Ultra-low Energy Ion Implantation into Graphene

Dissertation

for the award of the degree

"Doctor rerum naturalium"

of the Georg-August-Universität Göttingen
within the doctoral program Physics
of the Georg-August-University School of Science (GAUSS)

submitted by

Felix Junge

from Herzberg am Harz

Göttingen, 2023

Thesis Committee:

Prof. Dr. Hans C. Hofsäss
II. Physikalisches Institut, Georg-August-Universität Göttingen

Prof. Dr. Martin Wenderoth
IV. Physikalisches Institut, Georg-August-Universität Göttingen

Prof. Dr. Michael Seibt
IV. Physikalisches Institut, Georg-August-Universität Göttingen

Examination Board:

Reviewer: Prof. Dr. Hans C. Hofsäss
II. Physikalisches Institut, Georg-August-Universität Göttingen

Second Reviewer: Prof. Dr. Martin Wenderoth
IV. Physikalisches Institut, Georg-August-Universität Göttingen

Further members of the Examination Board:

Prof. Dr. Michael Seibt
IV. Physikalisches Institut Georg-August-Universität Göttingen

Prof. Cynthia A. Volkert, PhD
Institut für Materialphysik, Georg-August-Universität Göttingen

Prof. Dr. Thomas Weitz
I. Physikalisches Insitut, Georg-August-Universität Göttingen

Prof. Dr. Lino da Costa
Pereira Quantum Solid-State Physics, KU Leuven

Date of the oral examination: 27.10.2023

List of publications

Many of the results explained in this thesis and arising from the project have already been published in peer reviewed journals. The corresponding papers are as follows:

- H. Hofsäss, **F. Junge**, P. Kirscht, K. van Stiphout, Low energy ion-solid interactions: a quantitative experimental verification of binary collision approximation simulations, Mater. Res. Express 10 (2023) 075003 https://dx.doi.org/10.1088/2053-1591/ace41c
- **F. Junge**, M. Auge, H. Hofsäss, Lateral Controlled Doping and Defect Engineering of Graphene by Ultra-Low-Energy Ion Implantation, Nanomaterials (13) (2023) 658. https://doi.org/10.3390/nano13040658.
- R. Villarreal, P.-C. Lin, Z. Zarkua, H. Bana, H.-C. Tsai, M. Auge, **F. Junge**, H. Hofsäss, E. Tosi, S. De Feyter, S. De Gendt, S. Brems, E. H. Åhlgren, L. M. Pereira, Bond defects in graphene created by ultralow energy ion implantation, Carbon 203 (2023) 590–600. doi:https://doi.org/10.1016/j.carbon.2022.12.005.
- P.-C. Lin, R. Villarreal, H. Bana, Z. Zarkua, V. Hendriks, H.-C. Tsai, M. Auge, **F. Junge**, H. Hofsäss, E. Tosi, P. Lacovig, S. Lizzit, W. Zhao, G. Di Santo, L. Petaccia, S. De Feyter, S. De Gendt, S. Brems, L. M. C. Pereira, Thermal annealing of graphene implanted with mn at ultralow energies: From disordered and contaminated to nearly pristine graphene, The Journal of Physical Chemistry C 126 (25) (2022) 10494–10505. doi:10.1021/acs.jpcc.2c00855.
- M. Auge, **F. Junge**, H. Hofsäss, Laterally controlled ultra-low energy ion implantation using electrostatic masking, Nuclear Instruments and Methods in Physics Research Section B: Beam Interactions with Materials and Atoms 512 (2022) 96–101. doi:https://doi.org/10.1016/j.nimb.2021.12.001.

- **F. Junge**, M. Auge, H. Hofsäss, Sputter hot filament hollow cathode ion source and its application to ultra-low energy ion implantation in 2d materials, Nuclear Instruments and Methods in Physics Research Section B: Beam Interactions with Materials and Atoms 510 (2022) 63–68. `doi:https://doi.org/10.1016/j.nimb.2021.10.017`.
- R. Villarreal, P.-C. Lin, F. Faraji, N. Hassani, H. Bana, Z. Zarkua, M. N. Nair, H.-C. Tsai, M. Auge, **F. Junge**, H. C. Hofsaess, S. De Gendt, S. De Feyter, S. Brems, E. H. Åhlgren, E. C. Neyts, L. Covaci, F. M. Peeters, M. Neek-Amal, L. M. C. Pereira, Breakdown of universal scaling for nanometer-sized bubbles in graphene, Nano Letters 21 (19) (2021) 8103–8110. `doi:10.1021/acs.nanolett.1c02470`.

Contents

8 Implantation Simulations 75

9 ULE-Implantations into Graphene 93

1 Introduction

Graphene and other 2D materials, such as transition-metal dichalcogenides (TMDs), have attracted substantial research interest across diverse domains due to their extraordinary mechanical, thermal, and electrical attributes. These materials have sparked significant advancements in fields ranging from electronics to biomedicine. Noteworthy applications encompass biosensors for biomolecules and pollutants [1–4], spintronic devices [5], and water purification systems [6] and many possible future application for energy storage and conversion [7].

To manipulate the electrical, magnetic, structural, or optical characteristics of 2D materials, external atoms can be introduced into their crystalline structure [8–10]. A variety of methods can achieve this, including adjusting the growth process or diffusing atoms into the material [11, 12]. One widely adopted technique in the semiconductor sector is ion implantation. This procedure allows precise incorporation of foreign atoms into materials without altering growth processes or relying on chemical reactions or diffusion. Consequently, it guarantees highly specific atomic integration. Nevertheless, conventional ion implantation methods (>1 keV) are inadequate for doping 2D materials, since this necessitates achieving a maximum penetration depth of only a few nanometers. These shallow penetration depths can only be accomplished using extremely low ion energies, ensuring that the implantation energy remains within the range of several 10 eV [13]. At higher energies, the ions pass through the 2D material, resulting in some defect formation without being incorporated into and landing in the substrate. The idea of using a material layer, a so-called capping layer [14], through which the higher-energy ions would pass and thereby come to a stop in the 2D material, would also not work, as many recoils from the capping layer would also be incorporated into the 2D material (cf. ch. 8.1.4 and 8.2.3).

As generating an ion beam with such low energy and maintaining reasonable implantation currents (>10 nA on the sample) poses considerable challenges, Ultra-low Energy (ULE) ion implantation can be achieved by decelerating keV ions in proximity to the target. One of the most prominent strategies of deceleration is applying an electric potential to the sample. Unlike deceleration methods using a protective layer [14], this approach prevents recoiled atoms from entering the sample, thereby ensuring exclusive implantation of the desired atomic species and

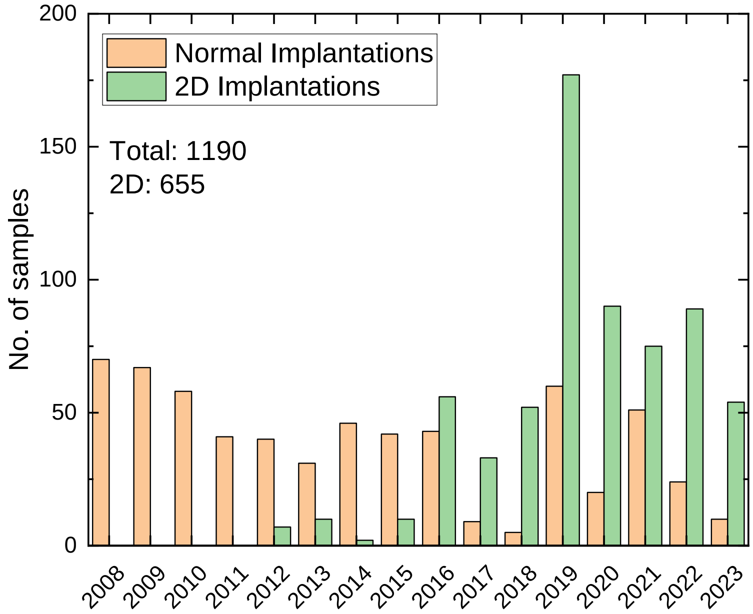

Figure 1.1: *Number of samples implanted with ADONIS over the years. Since 2008, a total of 1190 samples have been implanted, 655 of which were 2D materials (graphene, TMDs or hBN).*

preventing contamination. The efficacy of laterally uniform Ultra-low Energy ion implantation in tuning the properties and structural integrity of graphene and TMDs has already been successfully demonstrated [15–21].

To show the progression of implantation in 2D materials, the number of samples implanted with ADONIS in Göttingen is shown in Figure 1.1. Of the 1190 implantations performed since 2008, 655 were in 2D materials. Since ADONIS is currently the only device that can successfully direct implant into 2D materials due to the extremely low energy of the ions, this number also corresponds to the total number of samples fabricated worldwide up to this point.

Within the framework of this thesis, ion implantation, especially into graphene, has been further investigated, building upon the topic of several prior dissertations [22, 23].

The thesis is structured as follows: after this introduction, the material system graphene and its properties are briefly introduced (ch. 2). Subsequently, the theory of ion-solid interactions is discussed (ch. 3), which provides the theoretical description of ion implantation processes. A short chapter addresses the question of displacement energy of carbon in graphene, as this is an important parameter for selecting the ion energy for implantation when it comes to damaging graphene or introducing foreign atoms substitutionally (ch. 4). In Chapter 5, the methods and programs used for the analysis and characterization of the samples are briefly presented.

The main part of the work is divided into three aspects: one technical, one computational and one experimental. First, the technical innovations on the accelerator used for better implantation and providing new ion beam elements are discussed (ch. 6). This section particularly focuses on the newly developed ion source, which was created within the scope of this work. Additionally, a brief reference is made to the further development and testing of the new ULE deceleration unit used for laterally non-uniform implantation profiles, originally developed by Manuel Auge [22]. This chapter refers to publications on the ion source [24] and the deceleration unit [25].

Another part reports on the simulations and experimental verification of the new IMINTDYN program [26]. This code, developed by Hans Hofsäss, represents an advancement of the SDTrimSP code [27], and provides more accurate simulations of the ULE ion implantations (ch. 7). In this context, the vacancy was added as a target atom, allowing the simulation to more accurately calculate defects and crystal structures of 2D materials. Within this framework, test implantations and simulations (ch. 8) were conducted. In these chapters, reference is made to the publication on IMINTDYN [26].

The third aspect is the experimental modification of graphene using ULE ion implantation (ch. 9). Here, the implantations carried out during the course of the work and their results are presented. The publications [20, 21, 28, 29] are briefly summarized in this chapter, with a particular focus on the work conducted in Göttingen as part of these studies. Furthermore, unpublished experiments to create a p-n junction in graphene using ULE ion implantation is described.

The final part include the Conclusion and Outlook, suggesting possible future research directions based on the insights gained in this work.

2 Graphene

Graphene, although previously postulated to be thermodynamically unstable [30] was the first 2D material to be synthesized [31]. In the following chapter, the basic properties such as the crystal structure, the electronic properties of the bandstructure, known ways to fabricate and methods to dope graphene layers are presented.

2.1 Crystal structure

Graphene consists of a single atomic layer of carbon atoms, which are arranged in an sp^2 hybridization in a hexagonal honeycomb structure. The atoms have a bond angle of 120°. In Figure 2.1a, the graphene lattice is shown schematically with the corresponding lattice vectors and atom spacings.
The unit cell consists of 2 atoms with the lattice vectors

$$\vec{a}_1 = \frac{a}{2}\begin{pmatrix} 3 \\ \sqrt{3} \end{pmatrix}, \tag{2.1}$$

$$\vec{a}_2 = \frac{a}{2}\begin{pmatrix} 3 \\ -\sqrt{3} \end{pmatrix} \tag{2.2}$$

with nearest neighbor distance $a = 1.42\,\text{Å}$ and the corresponding reciprocal lattice vectors of the bravais lattice

$$\vec{b}_1 = \frac{2\pi}{3a}\begin{pmatrix} 3 \\ \sqrt{3} \end{pmatrix}, \tag{2.3}$$

$$\vec{b}_2 = \frac{2\pi}{3a}\begin{pmatrix} 3 \\ -\sqrt{3} \end{pmatrix}. \tag{2.4}$$

The lattice constant corresponds to $a_0 = 2.46\,\text{Å}$ [32]. The two atoms form two triangular sublattices as shown in Fig. 2.1a. If one looks at two layer graphene, multilayer graphene or graphite, it can be seen that the distance between the carbon layers is 3.34 Å [32].

Since the atoms are not uniformly distributed in the volume here, but instead form a thin atomic layer on top, and subsequently, the space to the next layer is empty, one can envision a graphene layer as a 1.11 Å thick carbon layer followed by 2.23 Å of empty space. This structure was assumed in the ion implantation simulations and will be explained in more detail in Chapter 8.1.1.

2.2 Electronic structure

The band structure can be calculated with the help of the tight-binding model and gives the following energy dispersion [30, 33]:

$$E(k_x, k_y) = \pm t \sqrt{(1 + 4\cos\left(\frac{\sqrt{3}k_x a_0}{2}\right) + \cos\left(\frac{k_y a_0}{2}\right) + 4\cos^2\left(\frac{k_y a_0}{2}\right)} \tag{2.5}$$

with the wave vectors k_x, y in x- and y-direction, a_0 the lattice constant and t the nearest-neighbor hopping energy needed for the electron motion. From the formula it is evident that the valence band (minus sign) has the same shape as the conduction band (plus sign). In addition, it is clear that both bands do not overlap, but touch in the so-called Dirac point and no band gap is available. In the case of free-standing graphene, the position of the Dirac-point energetically corresponds to the Fermi-energy of E_F =4.48 eV [34]. In Fig. 2.1b the band structure of graphene is plotted. The conical shape of the bands, which touch at the Dirac point, is clearly visible.

Because of the linear dispersion relation, the behavior of electrons in graphene is similar to that of massless particles, leading to improved mobility. Another consequence of this linear dispersion relation becomes apparent when examining electron states below E_F and hole states above E_F. Neither electrons nor holes can be precisely characterized using distinct Schrödinger equations; rather, they present themselves as quasi-particles, depicted by the Dirac equation [22, 35, 36].

2.3 Synthesis

There are various methods available for the production of graphene. Among these is exfoliation, where a single layer of graphene is removed using scotch tape and was also used to produce graphene for the first time [31]. Chemical vapor deposition (CVD) which is used to deposit a single layer of carbon on a substrate [37–39], and the epitaxial growth of a graphene

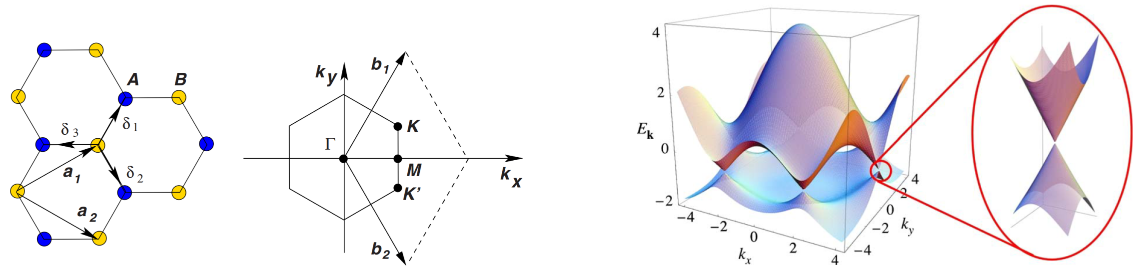

(a) **(b)**

Figure 2.1: *(a) Honeycomb lattice and its Brillouin zone. Left: lattice structure of graphene, made out of two interpenetrating triangular lattices (a_1 and a_2 are the lattice unit vectors, and $\delta_i, i = 1, 2, 3$ are the nearest-neighbor vectors). Right: corresponding Brillouin zone. The Dirac cones are located at the K and K' points. Reprinted figure with permission from [33] Copyright 2009 by the American Physical Society.(b) Electronic dispersion in the honeycomb lattice. Reprinted figure with permission from [33] Copyright 2009 by the American Physical Society.*

layer on SiC [40]. The methods are briefly explained below. The graphene layers used in this work were produced using CVD and then partially transferred onto other substrates, such as SiO_2, using PMMA. Various transfer methods are described in more detail in [41]. The disadvantage associated with methods entailing graphene transfer lies in the surface contamination attributed to the application of PMMA or other essential transfer chemicals. Conversely, direct approaches involving in-situ growth of graphene on the intended substrate prove to be more favorable.

2.3.1 Exfoliation

For mechanical exfoliation, one starts with a highly oriented pyrolytic graphite (HOPG) crystal. The goal is to remove only a single layer of graphene from the HOPG crystal. In this process, the weak van der Waals forces between the individual layers need to be overcome. The strength of these forces is about $300\,{}^{nN}/_{\mu m}$ [42] and can be overcome using a simple adhesive tape [40]. Through multiple iterations, the initially tape-covered graphite layers can be further thinned until only one layer remains. Subsequently, the tape is dissolved using acetone and the remaining flakes are collected and transferred onto a wafer. To remove residuals from the tape and to clean the graphene, further steps can be taken subsequently. Often, annealing in a reducing atmosphere or under vacuum at higher temperatures is applied [40, 43, 44].

2.3.2 Chemical vapor deposition

The Chemical Vapor Deposition (CVD) method is utilized to create thin films or coatings on various substrates. This technique involves introducing a solid material onto a substrate by promoting chemical reactions within the vapor phase. For graphene, the process relies on the decomposition of hydrocarbons such as methane (CH_4) at high temperatures [39]. To facilitate the decomposition, metal substrates like Ni, Cu, or Pt can be used as catalysts [38, 45, 46], on which the graphene forms as a protective layer. After the coating, the graphene can either be transferred to another substrate, which involves subsequent cleaning steps, or used directly on the metal substrate.

2.3.3 Epitaxial growth

Another promising method for producing large-scale graphene involves epitaxial growth on a silicon carbide (SiC) substrate. This growth process is based on the sublimation of Si from the topmost layer of the SiC substrate. The required temperature range for this growth falls between approximately 1100°C and 1800°C [47]. Within this span, substantial sublimation of silicon from the SiC substrate component occurs, resulting in the formation of a carbon-rich surface layer. The growth is facilitated by the high surface diffusion of atoms at these elevated temperatures [22].

2.4 Doping of graphene

In order to further tune the properties of graphene, in particular the electrical properties such as the creation of a band gap or the creation of n- or p-doped regions, foreign atoms can be incorporated into the graphene lattice or interaction effects with the substrate can be used. This is particularly important because a band gap must first be opened in the graphene before it can be used as a semiconductor. Although this can be accomplished by simply damaging the lattice, many applications require a specific level of the band gap. This work is largely concerned with the possibility of doping graphene using ion implantation, as this is one of the most widely used techniques for other semiconductors. It has already been shown that ULE ion implantation is possible [16, 17, 48]. By means of scanning tunneling microscopy measurements, the incorporation of foreign atoms into the graphene lattice could be detected [17] and the change of the Dirac cone could be confirmed by ARPES [49]. However, since ultra-low energies are required for the implantation of 2D materials and this technique is not widely used, other possibilities for doping graphene have already been developed, which will be briefly presented in the following.

2.4.1 Substrate and adsorption effects

To alter the electrical properties of graphene, it is not strictly necessary to incorporate foreign atoms into the lattice. It is sufficient that the interaction between graphene and the substrate on which it is positioned leads to a shift in the Fermi level, thus achieving n- or p-doping. Similarly, parts of a graphene layer can be coated with different metal atoms. For instance, applying gold can result in p-doping, as electrons transition from the graphene to the gold [50]. Achieving n-doping can involve the application of alkali atoms like potassium (K). Another option is the combination of freestanding graphene and supported graphene. In this case, the regions of the graphene that lie on the substrate induce doping, while the freestanding portion can be either p-doped or n-doped through an external electric field, thus enabling the realization of devices [50, 51]. Additionally, molecules can also be deposited onto graphene, aside from metal atoms. These molecules can also induce doping of the graphene through surface charge transfer, without damaging the graphene lattice [52].

2.4.2 Substitution of carbon atoms

Another approach to doping graphene involves the substitution of individual carbon atoms in the lattice with foreign atoms. In this regard, elements such as B and N are particularly viable options, given their possession of one electron less or more in the outer shell. Consequently, their incorporation into the lattice leads to p-type or n-type doping. However, it is important to bear in mind that the introduction of foreign atoms creates scattering centers for electrons, thereby significantly diminishing electron mobility and consequently, conductivity.

There are two avenues for introducing foreign atoms. Firstly, during the fabrication of the graphene layer, or alternatively, subsequently through additional treatments of the graphene, such as ULE ion implantation [17, 18], which was developed in Göttingen and will be used in this work, or post-annealing and the diffusion of atoms from the substrate, along with subsequent reactions under plasma treatments [53, 54]. Throughout the growth process, additional precursor molecules can also be employed within the CVD process, leading to the integration of foreign atoms [55–57]. Additionally, foreign atoms can be embedded into the substrate, diffusing from the substrate into the growing graphene layer during the CVD process and becoming incorporated therein [58].

3 Ion beam - solid interaction

When an ion beam is directed into matter, various interactions can occur, and these interactions strongly depend on the energy of the ions. Generally, most ions penetrate the material, with a few exceptions that scatter and are reflected by the surface atoms and create collision cascades with different target atoms along their path [59, 60]. This is due to the scattering of ions by the positively charged atomic nuclei. As a result of the collision cascade, damage occurs to the material's crystalline structure, as target atoms are knocked out of their lattice positions. These generated recoils can, in turn, scatter off of atoms within the material and create new recoils. This cascade leads to the ejection of some atoms from the material, allowing the target to be ablated or sputtered. This effect can be utilized for surface cleaning and for analytical methods such as secondary ion mass spectrometry [61]. The efficiency of the sputtering process depends on the mass of the ions, target atoms, ion energy, and the angle at which ions hit the surface [62–64].

Other effects that can occur are employed in various analysis methods, such as Nuclear Reaction Analysis (NRA, see 5.2.3) [65, 66] or Rutherford Backscattering (RBS, see 5.2.2) [67]. Another interaction occurs between the ions and the electrons of the target atoms. This can lead to excitations and ionizations, which are exploited, for instance, in Particle-Induced X-ray Emission (PIXE, see 5.2.1) [68]. At high energies and with heavy ions, a phenomenon known as a thermal spike can occur, where a substantial amount of energy is rapidly deposited into the electronic system, causing the region around the ion track to heat up significantly [69]. This can result in local phase transformations.

The crucial process in this work is the general form of ion energy loss as ions traverse through matter, as it significantly influences the penetration depth and depth distribution of ions. Thus, it represents an essential parameter for ion implantation.

The energy loss of ions is an important quantity in the interaction between ions and matter. It indicates how much energy the particles lose when passing through matter. A distinction is made between nuclear energy loss, due to interaction and scattering with target nuclei, and electronic energy loss, due to interaction with electrons [59]. Here, the nuclear energy loss can be understood as binary collisions with atomic nuclei within the material, and electronic

energy loss as the scattering and collisions with electrons from the atomic shells in the material. The electronic energy loss contributes a continuous energy loss, whereas in nuclear collisions, a certain amount of energy is transferred to the target atom per collision. The continuous deceleration of the ions allows depth information to be obtained, which, with the help of RBS or NRA allows measurement of the depth spectrum of the elements in the sample. The stopping power $S(E_0) = {}^{dE}/_{dx}|_{E_0}$ is the energy loss per path length of the ion. Additionally, the average penetration depth of ions can be determined through the analysis of energy loss. This allows for the calculation of penetration depths in ion implantation processes [59].
In Fig. 3.1a, the energy loss of carbon atoms in carbon, calculated by SRIM [70], is plotted. For calculating the electronic loss, SRIM uses fits to experimental data of H und He stopping and power laws to extrapolate the electronic stopping for all other elements. It is clearly evident that as the energy increases, the total loss decreases and the electronic energy loss predominates. At lower energies, the nuclear energy loss is dominant. Since the electronic energy loss dominates at high ion velocities, a distinction must be made between low and high energies. To differentiate whether a particle has high or low energy in this context, its velocity is compared to the velocity of electrons in the atomic shell, the Bohr, $^1/_{137}\ c$, or Fermi, $^1/_{200}\ c$, velocity [71] with c the speed of light, respectively.
At very high energies, ions can lose their energy due to radiation losses. Examples of this are, on the one hand, Bremsstrahlung and, on the other hand, Cerenkov radiation when a particle passes through matter at superluminal velocity. Since these phenomena occur in energy ranges that are irrelevant to this dissertation, they will not be discussed further.
The handling of the binary collision approximation (BCA), which is important for simulation programs, is explained in more detail in Chapter 7.1, where the underlying assumptions are also discussed.

3.1 Nuclear energy loss

The nuclear stopping power results from elastic collisions with atomic nuclei of the sample. In the following, the physical principles of the impact processes of atoms are explained and important parameters, such as the scattering angle and the impact parameter are described.
When a beam of charged particles hits matter, these particles are scattered by the atomic nuclei present. The resulting scattering angle Θ is the angle between the asymptotes of the hyperbola, which describes the trajectory of the scattered particle. This phenomenon arises because particles experience deflection caused by the Coulomb interaction, which follows an inverse square relationship with the distance between the charges. [72]. Another important

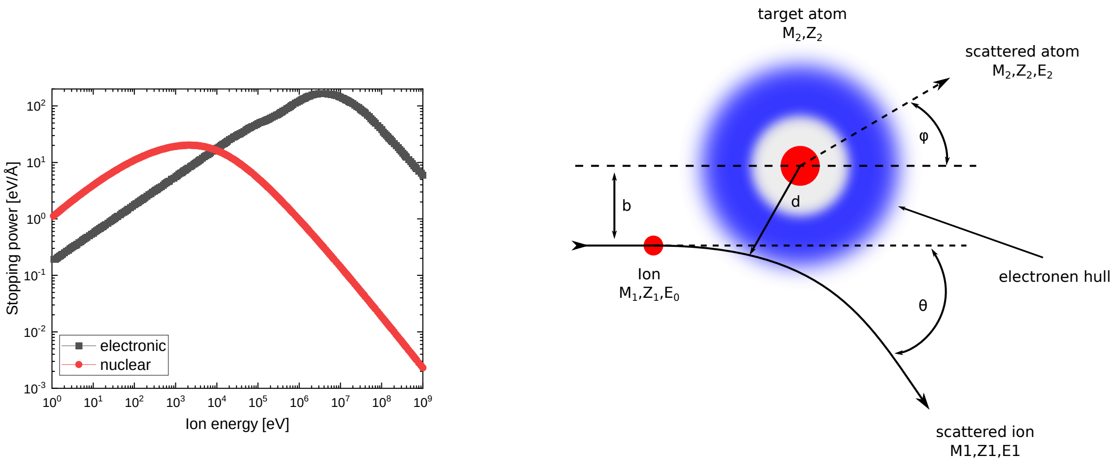

(a) **(b)**

Figure 3.1: *(a) Stopping power of C ions in a C target as a function of ion energy. The nuclear energy loss dominates at lower energies, while the electronic loss dominates at higher energies. Calculated using SRIM [70]. (b) Schematic representation of the collision between an ion and a target atom (after [72]).*

parameter is the collision parameter b, which describes the distance of the nucleus from the trajectory of the particle, if it would not have been scattered. The impact parameter can be derived with the help of energy and momentum conservation and is given by [72]

$$b = \frac{Z_1 Z_2 e^2 \cot(\Theta/2)}{4\pi\epsilon_0 M_1 v_0^2}. \tag{3.1}$$

Here Z_1 is the nuclear charge number of the incoming particle, Z_2 is the nuclear charge number of the nucleus at rest, M_1, v_1 are the mass and velocity of the incoming particle, θ is the scattering angle, e is the elementary charge, and ϵ_0 is the electric field constant.
The scattering angle Θ can be calculated using a screened Coulomb potential $V(r)$ as the interatomic potential. User A shielded potential is especially important when using ultra-low energies, since the ions do not get so close to the nucleus that they are not necessarily scattered within the K-shell of the target atom. As a potential between atomic nuclei, there are several approaches, such as the Bohr potential [70] or the in this thesis used Kr-C potential [73], which differ slightly in their parameters. Θ can be calculated by [74]

$$\Theta = \pi - 2\int_{r_{min}}^{\infty} \frac{b\,dr}{r^2\sqrt{1 - \frac{V(r)}{E_c} - \frac{b^2}{r^2}}}, \tag{3.2}$$

with r being the distance between the ion and the target atom and $E_c = E_0 M_2/(M_1+M_2)$, where E_0 is the initial energy. The energy transferred during the collision, denoted as T, can be calculated in the case of elastic collision using energy and momentum conservation as [70]

$$T = \frac{4E_0 M_1 M_2}{(M_1 + M_2)^2} \sin^2\left(\frac{\Theta}{2}\right). \tag{3.3}$$

The distance of closest approach d can be calculated using [72]

$$d = \frac{Z_1 Z_2 e^2}{4\pi\epsilon_0 E_0}, \tag{3.4}$$

where E_0 represents the energy of the projectile. The electrons of the target atom can be neglected since the incoming particle must get within the K-shell radius to be backscattered [72]. In Figure 3.1b the collision of two particles is shown graphically.

For the nuclear energy loss, it follows using T and n as the atomic density of the material

$$-\left.\frac{dE}{dx}\right|_{nuc} = \frac{8\pi n M_1 M_2 E}{(M_1 + M_2)^2} \int_0^{b_{max}} \sin^2\left(\frac{\Theta}{2}\right) b db. \tag{3.5}$$

The ions used for implantation in this study have energies in the range of a few tens of eV. Consequently, the nuclear energy loss is the dominant stopping process for the particles, and only a small portion of the energy is transferred to the electronic system.

3.2 Electronic energy loss

The electronic energy loss results from elastic and inelastic collisions of the ion with the electrons of the sample atoms. These collisions result in ionization and excitations of the target electrons. It is the dominant process at high energies and low ion masses [70]. Furthermore, it is responsible for the continuous slowing down of the ions [70]. The stopping power differs at high and low energies of the ion.

High Energy The electronic energy loss can be calculated at high energies using the Bethe-Bloch formula [75]. For relativistic considerations this is

$$-\left.\frac{dE}{dx}\right|_{El} = \frac{N Z_2 Z_1^2 e^4}{4\pi\epsilon_0^2 m_{el} \beta^2 c^2} \cdot \left[\ln\left(\frac{2m_{el}\beta^2 c^2 \gamma^2}{I}\right) - \beta^2\right]. \tag{3.6}$$

Here, N describes the electron density of the material and I the average excitation potential of the material. This can be approximated by $I = (10\,\mathrm{eV}) \cdot Z_2$ [70].

Low Energy At low energies the Bethe formula is no longer valid and the effective charge of the ion must be considered. This results from the change of the charge state of the ion due to collisions with shell electrons. In this context, electrons can be absorbed by the ion and subsequently emitted once more. The average charge of an ion in matter with respect to its velocity can be expressed by [70]

$$Z_1^{eff} \sim Z_1 \cdot \left(1 - \exp\left(-\frac{v}{v_{Bohr}} Z_1^{-2/3}\right)\right) \tag{3.7}$$

with the Bohr velocity v_{Bohr}. In this low-energy regime, the energy loss is proportional to $\sqrt{E}$ [76].

4 Displacement energy of C in Graphene

An important point for the choice of the implantation energy is the so-called displacement energy. This describes the energy which has to be transferred to an atom in order to be released from its lattice site, so that a vacancy remains. In ion implantation this energy is transferred by the collision with target atoms. In the following chapter we will focus on the displacement energy of carbon in graphene. In particular, the current state of publications with density function theory molecular dynamic (DFT-MD) simulations and experiments with TEM studies will be discussed. One reason for the more detailed treatment is the published value of 22 eV [77], which stands out in its magnitude when compared to the sublimation energy of carbon of 7.431 eV [78].

4.1 C-C bonds

A simple consideration of displacement energy can be made using the C-C bond. To remove a carbon atom from the lattice, 3 C-C bonds have to be broken. The binding energy of the sp^2 C-C bond is $348\,{}^{kJ}/_{mol} = 3.607\,{}^{eV}/_{bond}$ [79]. With 3 bonds, this would correspond to a displacement energy of 10.821 eV. By the impact of a charged ion, the electron deficit already provides a perturbation in the system, which can further decrease the displacement energy. Thus, more damage is generated in graphene when higher charge states of ions are used [80].

4.2 DFT-MD simulations

The displacement energy value has been calculated in different studies using MD and DFT simulations [13, 77, 81–85]. The energies determined here range from about 23 eV [86] down to 12 eV [84] for slightly different graphene configurations, with 22 eV[77, 85] being the most quoted value for pristine graphene. Both electron irradiations [77] and ion irradiations [85] were investigated. For the Ion irradiation simulation, molecular dynamic simulations (MD) were combined with an analytical potential (AP). The Ziegler-Biersack-Litmark (ZBL) [70] was used as the repulsive potential. The charge of the ion was ignored. To verify these results, additional DFT-MD simulations were performed, yielding the same results (22.2±0.2 eV vs. 22.05 eV). Own MD simulations, performed with LAMMPS [87] using the tersoff/zbl potential, showed that the ions must have an energy of at least 23 eV to exchange a carbon. Since the direct collision of two carbon atoms was simulated, this also corresponds to the displacement energy. In this potential, however, no charges of the particles are considered, but only bond lengths between the atoms. This leads to the fact that the arriving ion immediately forms a bond in sp^3 or sp^2 configuration, depending on the distance, and therefore the energy of the incoming ions is eventually distributed to more than one target atom, which makes this potential unsuitable for the considered case.

4.3 TEM Measurements

For the measurement of displacement energy TEM investigations can be considered. Here graphene samples are bombarded with electrons and the damage versus the electron energy is observed. The electrons transfer their energy to carbon atoms and can dislocate them from the lattice. In order to calculate the maximum amount of energy that can be transferred to an atom, the scattering process must be considered. Since electrons are negative charges and atomic nuclei are positive charges, this can be treated as a typical Kepler problem. One factor that complicates scattering kinematics is the Bremsstrahlung, which cannot be neglected because of the light electron mass, so it is a strongly inelastic scattering. In addition, relativistic calculations must be made for these electron energies. In the following two situations are considered separately. First, the trapping of the electron and second, the backscattering of the electron. In addition only electrons are considered, which approach the nucleus on less than a Bohr radius, because otherwise the shielding of the shell electrons suppresses the scattering clearly, since no interaction takes place by the nucleus potential. Since the scattering process is in any case clearly inelastic, only the conservation of momentum can be considered for the calculation of the transferred kinetic energy. The necessary formulas are for the relativistic velocity

$$\begin{aligned} K &= (\gamma - 1) m_0 c^2 \\ \rightarrow v &= \frac{\sqrt{K}\sqrt{2m_0c^2 + K}}{K + m_0c^2} \end{aligned}$$

For the relativistic electron momentum p_{el}

$$p = \sqrt{\frac{K^2}{c^2} + 2Km_0}$$

critical Radius r_{crit}:

$$\begin{aligned} m\gamma\frac{v^2}{r} &= \frac{1}{4\pi\epsilon_0}\frac{Ze^2}{r^2} \\ \rightarrow r &= \frac{1}{4\pi\epsilon_0}\frac{Ze^2}{v^2 m\gamma} \end{aligned}$$

and for the kinetic energy from momentum, in this case classical since the carbon atom is 21895 times heavier than an electron which leads to v«c,

$$K = \frac{1}{2}\frac{p^2}{m}.$$

Case 1: If the electron approaches the nucleus too close, it will be trapped in the nuclear potential. This minimum radius can be calculated classically by the force equilibrium between centrifugal force = electric force. Below this critical radius the electron would slowly spiral into the nucleus and lose its energy in the form of Bremsstrahlung. Thus, in this process, the entire electron momentum is transferred to the nucleus. If one take the minimum electron energy of 85 keV as reported in [88] and the mass of carbon, we get a transfer of kinetic energy of 8.42 eV. The rest of the energy is emitted in the form of radiation. The momentum of the emitted photons in this case can be neglected, since the photons are emitted in every direction and therefore cancel out extra momentum contributions.
Case 2: The maximum transmitted momentum would take place at a recoil of 180° of the electron, because there the momentum of the incident as well as of the outgoing electron is transmitted to the nucleus, thus it would be 2 times the electron momentum, which would correspond to an maximum energy transfer to the carbon of 16.836 eV. Since electrons can only perform a 180° scattering by completely circling the nucleus, energy is also emitted in the form of Bremsstrahlung. This is given by the deflection of the electrons around the nucleus and by the acceleration by approaching respectively the deceleration by moving away from the nucleus. To get an upper estimate of the transfered maximum momentum, the Bremsstrahlung is neglected once more, and the impact can be assumed to be completely elastic. For the maximum energy transfer during a collision of a relativistic and a non-relativistic particle it

applies [89, 90]:

$$E_{max} = \frac{E_0(E_0 + 2m_e c^2)}{E_0 + \left(1 + \frac{m_e}{M_C}\right)^2 \frac{M_C c^2}{2}}$$

For 85 keV electrons, a maximum of 16.834 eV is transferred to the carbon. Consequently, this estimate can be equated with the assumption of pure momentum transfer. It should be noted again that by neglecting the bremsstrahlung, this is only an upper estimation. Thus, already from these TEM experiments and simple estimates for the maximum energy transfer it can be concluded that the displacement energy of 22 eV is too high. It is surprising, is that in [88], where the TEM measurements were undertaken, the energy value of 22 eV from the DFT-MD simulations was used. Other studies also report $T_d \approx 21$ eV [91] Previous studies on graphite suggest a displacement energy of carbon of 15-20 eV [90] under electron irradiation, with some studies reaching down to 12 eV [92].

4.4 Sputtering of graphite

Further evidence supporting the idea that the displacement energy is significantly below 22 eV and closer to the sublimation energy is derived from sputter experiments [93, 94]. In these experiments, researchers measured the sputter yield under ion irradiation and compared the results with simulations. In both cases, they used either C ions with energies ranging from 100 eV to 6 keV [93] or Ar ions with an energy of 30 keV [94]. The simulations were conducted using TRIM [60], and they assumed the sublimation energy of carbon (7.4 eV) as the surface binding energy, which represents the energy required for a carbon atom to be sputtered from the surface. The experimental results consistently showed that the actual sputter yield was up to twice as high, regardless of the incident ion angle in respect to the simulations. Both studies concluded that the proposed value of 7.4 eV for the surface binding energy was too high [93, 94].

To explain this phenomenon, it is important to note that when removing carbon atoms through sputtering, they must first be displaced from the carbon lattice. In this context, the term surface binding energy can be understood as the displacement energy, which is lower than the sublimation energy and significantly lower than the suggested 22 eV. One possible explanation for this difference is that during the sputtering process, not only individual atoms are ejected but also dimers in the form of C_2 molecules, which possess their own binding energy and therefore require less energy to be sputtered.

While this study specifically examined graphite rather than graphene, the insights gained from these experiments can be applied to the process of ultra-low energy ion implantation in graphene. Particularly the study [93], which conducted experiments at low ion energies of 100 eV, demonstrates that the displacement energy during ion irradiation in this energy range is more closely to the sublimation energy or even below it.

4.5 Implantations

Another indication for the displacement energy of carbon during implantation is given by Raman measurements of graphene implanted samples (cf. 9.3). In [21], a disorder in the lattice can be measured for noble gas implantations energies down to 15 eV. For the studied ions (He, Ne, Ar) and using the 22 eV as displacement energy, a vacancy should only form at higher energies (29 eV, 23 eV, 31 eV) considering the perfect head-on collision with maximum energy transfer. In this study, it was found that the carbon was removed from the graphene and formed an additional bond with the substituent. The C atom was still in a bond with other C atoms from the graphene but was no longer incorporated in the graphene lattice and formed a so-called bond defect [21]. For ion implantation and used simulations it is shown that the carbon can already be removed from the lattice at an energy transfer lower than the 22 eV and can be replaced by another atom, even if it is not completely removed from the sample.

Therefore, in case of implantations it can be said that a significantly lower displacement energy can be assumed. It's worth mentioning that in ion implantation, where substitutions take place, no vacancies are generated, making this process inherently more energetically favorable. A further point is the irradiation with positive ions, so that the electronic system is locally strongly disturbed and thus the breaking of the bonds is supported. A possible experiment to evaluate the necessary implantation energy would be the implantation of boron or nitrogen in graphene at different energies and subsequent investigation by STM. Boron and nitrogen would be suitable for this purpose, since they guarantee a maximum energy transfer due to their mass similar to carbon (see Eq. 5.5). A possible source of deviation in the displacement energies from the simulations could be the use of wrong potentials, which can reproduce the correct parameters and properties in thermal equilibrium, but cannot reproduce them for a process like ion irradiation, which can transfer extreme energy to single atoms in a very short time and is far away from thermodynamic equilibrium. Another reason could be the neglect of the charge of the ion, which can already damage the bonding structure of the graphene and thus brings some additional potential energy into the system. For the simulations (ch. 7) performed in this work, the sublimation energy of carbon of 7.431 eV was chosen as the displacement energy, which also corresponds to the vacancy formation energy [95].

5 Methods

In the following chapter, the methods used for sample implantation and characterization are explained. These include techniques for elemental analysis and thickness determination such as particle induced X-ray analysis (PIXE), Rutherford-backscattering spectrometry (RBS), nuclear reaction analysis (NRA) and Auger electron spectroscopy as well as examination methods for characterizing the graphene layer such as Raman spectroscopy, low energy electron diffraction (LEED), X-ray photoelectron spectroscopy (XPS), angle-resolved photoemission spectroscopy (ARPES), scanning tunneling microscopy (STM) and Scanning kelvin probe microscopy (SKPM).

5.1 Ultra-low Energy (ULE) Ion Implantation

Ion implantation is a technique widely used in industry to modify the properties of solids. This technique has wide applications, from the coloring of gemstones [96] to the modification of semiconductors [97] and stands out as a crucial technique for introducing dopants into semiconductors. The unique atomic-thin nature of 2D materials necessitates a reduction in typical implantation energies from over well 100 eV to a range of just a few tens of eV, in order to precisely control ion penetration depth. Molecular dynamic simulations carried out on graphene have indicated that achieving a high likelihood of substituting a single carbon atom requires implantation energies below 100 eV [13]. While industrial applications commonly involve shallow implantations ranging from 100 eV to 2 keV [98], such energy levels are unsuitable for implanting ions into 2D materials.

To provide an ion beam with such low energies, three different typical approaches can be taken. First, ions with low energy can already be produced by choosing the accelerating voltage from the source as low as possible. The big disadvantage is that at low voltage only a few ions can be extracted from the source, since the current is proportional to $U^{3/2}$ after the Child-Langmuir law [99]. In addition, it is much more difficult to direct the ions through the accelerator to the target, because the lenses have a much stronger effect, the fewer energy or slower the ions are. Slow ions also bring space charge effects into the foreground, which cause the beam to defocus itself. The advantage of this method would be that, depending on the energy distribution of the ions from the source, a defined energy of the ions on the target could be achieved.

The second approach is to decelerate the ions by using a capping layer [14]. Here, high energy ions (a few keV) are passed through a solid, which is either directly on the sample or directly in front of it. The advantage of this method is the use of high-energy ions, whereby the focusing, the mass separation and especially the beam current can be optimized much more easily. However, a very big disadvantage is the inaccurate energy distribution of the ions when they hit the actual target. Due to the deceleration by a solid body, a strong energy spread is achieved, which is significantly higher than the energy distribution from the source. Furthermore, a collision cascade is generated inside the capping layer, with the generation of many recoils. These recoils are also incorporated into the 2D material, which is why precise doping is not possible, since both the fluence cannot be accurately determined and foreign atoms from the capping layer are implanted. The amount of recoils can easily exceed the fluence of the ions, depending on the composition of the capping layer and the energy of the ions. Therefore, as demonstrated in Chapter 8.2.3, this method is unsuitable for slowing down and implantation in 2D materials.

The third approach is the electrostatic deceleration of the ions in front of the target. There are several approaches for this: The one used in this work, the target can be connected to high voltage, so that an opposing field is formed, in which the ions are slowed down. It is important to use the same power supply for acceleration and deceleration to compensate for fluctuations in the potentials. Furthermore, in this approach, the deceleration takes place only a few mm in front of the sample, which prevents strong defocusing due to space charges and keep all advantages having a high energetic ion beam in the first place. An alternative option is to decelerate the ions by means of lenses [100, 101]. The advantage of this method is that the target does not have to be connected to a high voltage and all the electronics are easier to connect. The disadvantage is that the ion beam is difficult to focus due to the deceleration by lenses and the beam current decreases strongly, so that an efficient deceleration has not yet been achieved at the time of this work. Another possibility is similar to the one used in this work, with the difference that not the source and the sample are put on high voltage but the beam tube. Thus the sample would still be at earth potential and the ions would be automatically decelerated when leaving the beam tube. The biggest disadvantage is that all beam tube parts including the lenses and their power supplies have to be connected to high voltage and isolated, which is a significant effort for the electronics.

The accelerator ADONIS used here, with which the deceleration is carried out by means of a deceleration voltage on the target, is described in detail in chapter 6.

Independent of the method used for deceleration, care must be taken that the sample is electrically conductive and has good contacts. Otherwise, when the ions are irradiated, the sample would become charged and generate an additional counter-field, which on the one hand would further decelerate the ions and thus vary the energy, and on the other hand would completely deflect the ions so that no implantation can take place. Due to the low ion energies, this effect is significantly more present than in implantations with high-energy ions.

5.2 Elemental analysis

A large part of this work deals with the development of a new ion source for the ADONIS accelerator. To test the new implantation elements, implantations were made in tetrahedral amorphous Carbon (ta-C) and silicon and then tested for their elemental composition. For this purpose, the accelerator-based methods PIXE, RBS and NRA were used as well as Auger electron spectroscopy. PIXE offers the advantage that the elements can be determined unambiguously. A disadvantage is the non-existing possibility to detect light elements (Z<11) and that averaging is done over a large sample volume (1 mm beam diameter at a penetration depth of $\approx 50 - 100\,\mu$m). In contrast, RBS can provide both accurate fluence measurements of the implanted ions and a depth resolution of a few nanometers. A disadvantage is the decreasing mass and therefore element resolution, especially for heavy elements. Very light elements (Z<5) are also difficult to identify due to their low backscatter energy and very low effective cross section for scattering. Auger offers the possibility to examine the sample surface for elements. In addition, light elements (Z<11) can be identified. Another advantage is the low penetration depth, so that only the first few nm of the sample are examined. However, the applied Auger spectrometer was only used to make qualitative statements and not to determine quantitative values for the amount introduced.

5.2.1 Particle induced X-ray Emission

Particle Induced X-Ray Emission (PIXE) is a method to investigate the elemental composition of a sample. In this almost non-destructive method, the sample atoms are ionized under proton bombardment [68]. The energy released when the gaps in the atomic shell are filled is emitted in the form of X-rays and is characteristic of the element. The intensity of the radiation can be used to determine the ratio of the elements in the sample.

Bohr's atomic model is used to describe the origin of the characteristic X-ray radiation. In this model, the electrons move on circular paths of different radii, the so-called shells, around

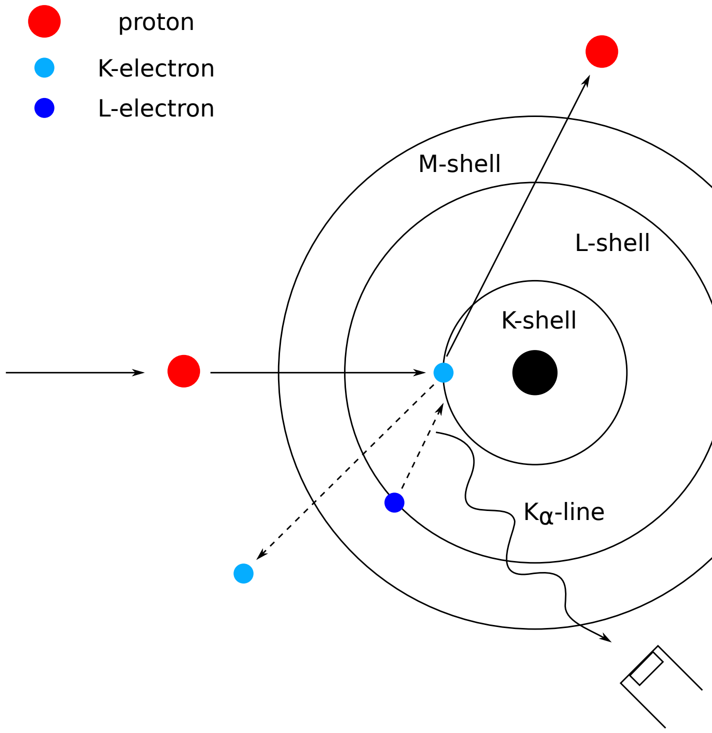

Figure 5.1: *Schematic of the PIXE process. A proton knocks an electron out of a low shell. The free space is filled by a higher-energy electron emitting X-rays.*

the atomic nucleus. If a particle hits an electron, it is knocked out of its shell and the atom is ionized. If this happens within a shell close to the atomic nucleus, a low-energy state is unoccupied and is filled by an electron from a higher shell. The difference in the electron's energy is thereby emitted in the form of X-rays, which have a specific value for the element because the atomic potentials of the individual elements differ.

For each element there are different characteristic lines, depending on which shell has been ionized and from which shell the electron filling up the state originates. For example, the K_α line is formed when the K shell is ionized and the filling electron comes from the L shell of an atom. In figure 5.1 the PIXE process with the Bohr atomic model is shown. To calculate the energy and wavelength of the characteristic radiation, Moseley's law [102] can be used:

$$\frac{1}{\lambda_{ik}} = (Z - S)^2 \cdot R_y \left(\frac{1}{n_k^2} - \frac{1}{n_i^2} \right). \tag{5.1}$$

Here n_i is the main quantum number of the electron before the transition and n_k is the main quantum number of the electron after the transition. Furthermore, R_y describes the Rydberg constant, Z the nuclear charge number and S the shielding of the nuclear charge due to the shell. The fluorescence yield holds significant importance in elemental analysis, signifying the likelihood of decay for an ionized, excited atom while emitting X-rays. This probability is considered over an entire electron shell, as opposed to individual spectral lines. Notably, the fluorescence yield (f) scales proportionally with the atomic proton number (Z). For instance, the K shell displays typical f values ranging from 0.0027 for carbon to 0.9 for gold. Evidently, lighter elements exhibit lower X-ray fluorescence yields, due to the increasing amount of auger electrons, contributing to their challenging detection and rendering PIXE inadequate for detecting such elements [103]. During the irradiation with protons, besides the characteristic X-rays also Bremsstrahlung can occur. When electric charges undergo acceleration, they emit electromagnetic radiation. The emitted radiation's energy increases with the strength of the acceleration, potentially falling within the X-ray spectrum and creating a background radiation that distorts measurement outcomes [104]. In PIXE experiments, the Bremsstrahlung phenomenon arises from two sources: the deceleration of protons within the material and the generation of electrons through proton-induced ionization of atoms in the sample. Proton Bremsstrahlung occurs when a proton scatters off an atomic nucleus due to Coulomb interactions, resulting in its deceleration. However, the contribution of this process to overall Bremsstrahlung is relatively minor due to the substantial mass of protons. It becomes noteworthy only at exceedingly high proton energies [104]. Secondary electron Bremsstrahlung occurs when an electron, previously displaced from its atomic shell by a proton, scatters and alters its velocity. The high mass and energy of the protons causing atomic ionization lead to the emitted electrons attaining high velocities. Furthermore, owing to the electrons' low mass, they relinquish a significant portion of their energy in individual collisions. This dynamic gives rise to secondary electron Bremsstrahlung, which contributes significantly to the background radiation. The upper limit of energy, denoted as T_m, that X-ray radiation can achieve through this process is expressed as [104]

$$T_m = \frac{4m_e E_p}{m_p}, \tag{5.2}$$

where E_p signifies proton energy and m_p represents proton mass.

PIXE measurements were performed at the external beam line of the 3 MV tandem accelerator of the II Physical Institute in Göttingen. A special feature of this measurement site is the extraction of protons in air through a 170 nm thick diamond membrane [105]. For better investigation of lighter elements down to Na (Z=11), the area between the sample and the detector can be flooded with He to minimize the shielding of the low-energy X-ray radiation. For the measurements, protons with an energy of 2.5 MeV were shot on the target, energy loss through the membrane and the air in front of the sample taken into account. The protons impinge diametrically on the sample with a detector sitting in 45° direction to the sample. The distance between the membrane and the sample is 5 mm while the distance between the sample and the detector is 4 mm. Typical currents of 2-10 nA proton current and a beamspot of 1 mm diameter were used. The penetration depth at this energy corresponds to about 70 μm (calculated using SRIM [70] for protons on Si).

5.2.2 Rutherford-backscattering spectrometry

Rutherford Backscattering Spectrometry (RBS) is an important method for the elemental analysis, as it allows conclusions to be drawn about the elemental composition and depth profiling. Thus, individual layers of a multilayer system can be detected and measured. Another advantage is that even light elements, for which other ion beam analysis methods like PIXE are blind, can be detected. RBS is based on the principle of elastic scattering of charged ions by nuclei. Thus, an incoming ion is scattered in the nuclear potential of an atom present in the sample due to the coulomb interaction and is subsequently detected. During this collision, part of the energy of the incoming particle is transferred to the sample atom. This energy transfer depends on the mass difference of both collision particles. By measuring the energy of the scattered particle, the mass and thus the element of the atom present in the sample can be obtained. The particles are measured here in backscatter geometry with an scattering angle near to $\theta = 180$, to ensure a good mass resolution.

In every collision, a fraction of momentum gets conveyed to the colliding partner. Consequently, a particle experiences a reduction in its kinetic energy owing to the collision. The proportion between the initial and post-collision energies of the projectile is referred to as the kinematic factor, denoted as k. The exchange of momentum hinges on the masses of the particles involved and the scattering angle during the interaction. As a result, the kinematic factor k tends to increase as the mass of the stationary particle becomes larger. When calculating the kinematic factor, it is assumed that nuclear reactions or resonances do not come into play. To derive the kinematic factor, the conservation of energy and momentum during the collision is taken into account. A moving particle with mass M_1 and velocity v_0 collides with a stationary particle of mass M_2. In the case of an elastic collision, both energy and momentum are preserved, and no energy is dissipated as thermal energy. Therefore applies

$$E_0 = E_1 + E_2 = \frac{1}{2}M_1 \cdot v_0 = \frac{1}{2}M_1 \cdot v_1 + \frac{1}{2}M_2 \cdot v_2 \tag{5.3}$$

and

$$M_1\vec{v_0} = M_1\vec{v_1} + M_2\vec{v_2}, \tag{5.4}$$

with v_1 and v_2 of the velocities after the impact. By dividing the velocities to a parallel and perpendicular component to $\vec{v_0}$ and some conversions the kinematic factor can be derived. This is leading to [72]

$$k = \frac{E_1}{E_0} = \left(\frac{(M_2^2 - M_1^2 \sin^2\theta)^{1/2} + M_1 \cos\theta}{M_1 + M_2} \right)^2. \tag{5.5}$$

It's evident that the kinematic factor is influenced by the mass ratio and the scattering angle, while being independent of the incident particle's energy (E_0). Consequently, if we focus solely on a specific scattering angle, we can deduce the mass of the atoms in the sample from the energy of the scattered projectiles. Notably, for scattering angles of $\theta = 180°$ and $\theta = 90°$, special cases arise where the kinematic factor adopts simplified forms: At $\theta = 180°$:

$$k(\theta = 180°) = \left(\frac{M_2 - M_1}{M_2 + M_1} \right)^2 \tag{5.6}$$

At $\theta = 90°$:

$$k(\theta = 90°) = \left(\frac{M_2 - M_1}{M_2 + M_1} \right). \tag{5.7}$$

From this it can be derived that at an angle of $\theta = 180°$ the mass resolution becomes maximum and thus the reflected particles should be detected near this angle. It should be noted, that backscattering is only possible, if the mass of the projectile is smaller than the target mass.

The cross section is the effective collision area and a measure of the likelihood of interaction between a moving particle and a stationary particle. For a spherical target, the cross-section would be equal to the geometric cross-section and is given by $\sigma = \pi r^2$ [72]. In order to derive a formula for computing the Rutherford cross section, the issue is approached from a classical perspective. It is postulated that solely the Coulomb force is influential in this scenario, as stated in [72]. Additionally, the assumption is made that the scattering occurrence remains elastic and the charge is localized to a point. Furthermore, it's considered that the particle possesses infinite rest mass, thus encountering no recoil effect [72]. The resultant expression derived is as follows:

$$\frac{\mathrm{d}\sigma}{\mathrm{d}\Omega} = \left(\frac{Z_1 Z_2 e^2}{16\pi\epsilon_0 E}\right)^2 \frac{1}{\sin^4(\theta/2)}. \tag{5.8}$$

In this context, $\frac{d\sigma}{d\Omega}$ represents the differential cross-section, which essentially signifies the cross-section amount per unit solid angle. The corresponding interaction cross section in the laboratory system is given by [72]

$$\left(\frac{\mathrm{d}\sigma}{\mathrm{d}\Omega}\right)_{lab} = \left(\frac{Z_1 Z_2 e^2}{8\pi\epsilon_0 E}\right)^2 \frac{1}{\sin^4(\theta)} \frac{\left(M_2\cos(\theta) + \sqrt{M_2^2 - M_1^2\sin^2(\theta)}\right)^2}{M_2 \cdot \sqrt{M_2^2 - M_1^2\sin^2(\theta)}}. \tag{5.9}$$

The complete Rutherford cross-section is determined by integrating the differential effective cross-section across the entirety of the solid angle. As a result of eq. 5.8, there is an increased probability of scattering when dealing with heavy elements (specifically higher atomic numbers Z_2) and lower energies. RBS exploits the nuclear energy loss, which is described in ch 3.1.

The RBS measurements were performed at the Cockraft-Walton type accelerator 'IONAS' at the II. physics institute in Göttingen [106]. Alpha particles with an energy of 860 keV were used. The beam current on the sample fluctuated between 1 and 15 nA at a beam diameter of either 0.5 or 1 mm. Three detectors were used, each of which had a solid angle of 3.2 msr. Two of the detectors were set up at a backscatter angle of $165°$ and one at a backscatter angle of $150°$.

High resolution RBS A special form of RBS is high resolution RBS. Here, the energy and thus the depth resolution can be significantly increased. For this purpose the backscattered He-ions are energy filtered by a cylindrical electrostatic analyzer (ESA). In this process, the a periodic triangular voltage is applied at both capacitor plates, so that only one energy passes through the cylindrical condensor and reaches the detector. Since one voltage corresponds exactly to one energy, the voltage signal is used as the input signal, while the signals from the detector act as the gate signal. The setup used in Göttingen consists of an ESA detector with a 300 mm central radius, a plate spacing of 6 mm and a 90° sector angle. A backscatter angle of 127° is considered and the achieved energy resolution is $\Delta E/E \approx 0.5\%$ which corresponds to an equipment constant [107]. In this case, ΔE is not constant and depends on the energy because there is a different binning between the Multichannel Analyzer and the ESA detector. Special attention has to be paid to the vacuum in the ESA, because the energy loss due to a too high pressure and the energy straggling of the He ions on the way to the detector determines the energy resolution. The vacuum of 2×10^{-7} mbar achieved is sufficient for the system used to ensure negligible energy loss over the 55 cm flight distance between the sample and detector. The HR-RBS was used to test the IMINTDYN program, in particular to measure the depth of penetration of the W implantations and to compare it with simulations to find out whether the introduction of vacancies into the simulation is useful [26]. A description of the HR-RBS setup used here and its specifications can also be found in [26].

5.2.3 Nuclear reaction analysis

Nuclear reaction analysis (NRA) is a method that uses nuclear reactions to detect and quantify elements in a sample. If the protons have enough energy to overcome the Coulomb barrier of the target atom, they can be absorbed by the nucleus, leading it to an excited state, which subsequently decays. The reactions can be described by a reaction equation of the form

$$a + X \rightarrow X^* \rightarrow Y + b + n\gamma, \tag{5.10}$$

with a the projectile nucleus with mass M_1, X the target nucleus with mass M_2, X^* the excited intermediate state and Y,b the products of the reaction [72]. Furthermore, gamma rays $n\gamma$ can be produced. One possible reaction is ^{4}He production by protons impinging on ^{7}Li. In this process, the protons are absorbed by the ^{7}Li nucleus. The resulting excited ^{8}Be nucleus subsequently decays into 2 α particles, each of which has an energy of about 7-8 MeV [108]. The reaction equation for this process is [65]

$$^7\mathrm{Li} + {}^1\mathrm{H} \rightarrow {}^4\mathrm{He} + {}^4\mathrm{He} + 17346{,}24\,\mathrm{keV} \tag{5.11}$$

or

$$^7\mathrm{Li}(\mathrm{p}, \alpha)^4\mathrm{He} \quad \text{with} \quad Q = 17346{,}24\,\mathrm{keV}. \tag{5.12}$$

The Q-value indicates the energy which is released during the reaction. Often, several reactions occur simultaneously; thus, in addition to ^{4}He production, ^{7}Be production is also possible, in which a neutron is emitted in addition to the beryllium nucleus. However, the reactions have different cross sections, so that ^{7}Be production is about 3 times more likely at a proton energy of 2.66 MeV [65]. NRA is particularly useful for the detection of light elements, since reactions in this method occur at proton energies as low as 1-5 MeV [72]. Also, NRA is isotope

specific, which is why diffusion properties in materials can be better studied. A special case of NRA is resonant NRA. Here, resonances in the effective cross section at specific energies of the projectile are exploited to induce the reaction. Using this method, depth profiles of concentrations can be obtained because the energy of the projectile beam can be changed so that, due to the loss of energy in the sample, the resonant energy occurs at a previously calculated depth. Here, the method is used to detect the light element Li, for which the other methods are blind due to their low mass and resulting low effective cross section for RBS and low fluorescence yield in PIXE. In this process, protons are directed at the sample, triggering nuclear reactions. First, the proton is absorbed into the nucleus, which decays almost instantaneously. This can release alpha particles, neutrons and gamma radiation, which are subsequently detected. Due to the high energy, the α particles can be detected almost background-free. Because of the energy loss within the sample, a depth concentration analysis is also possible, which has a resolution of 250 nm [105] in the used setup.
NRA measurements for lithium detection were conducted at the external beamline of the 3 MV Tandem Accelerator at the II. Physical Institute in Göttingen. In this study, protons with an energy of 2.5 MeV were used. The experimental setup used and its detailed specifications are published by the author in [105].

5.2.4 Auger electron spectroscopy

Another technique for elemental analysis is Auger electron spectroscopy (AES). Like PIXE, this method is based on the binding energies of the electrons in the atomic shell. First, an electron is knocked out of a lower shell of the atom and the resulting gap is filled by another electron of higher energy. The difference in energy is not emitted in the form of X-rays, but is transferred to another shell electron, which can leave the nucleus when the binding energy is overcome. Given that both the binding energy of electrons and the energy disparity between states within the shell are distinct to each element, the element can be determined by evaluating the energy of the emitted electron, commonly known as an Auger electron after its discoverer Pierre Victor Auger [109]. The strength of the Auger effect is Z dependent and dominant at small Z. Exceptions are H and He, since at least 2 electrons must be present in the L shell, one which fills the hole and a second which absorbs the energy of the transition. For excitation and first ionization of the atom, electrons, photons (mostly X-rays), or ions can be used, as long as the necessary energy can be transferred. Mostly electrons in the energy range of 2-5 keV are used for AES. This makes AES a very shallow characterization method, since the penetration depth of electrons at these energies is limited to a few nanometers.

The Auger measurements done in this work served to get a first impression of the implanted atomic species when testing new elements in the source. For this purpose the Auger spectrometer was used, which is directly connected to the ADONIS accelerator, so that a transfer completely in UHV (5×10^{-9} mbar) was possible. Here an electron beam was generated by means of an electron gun, which then impinges perpendicularly on the surface of the sample with an energy of 3 keV. The current of the electron was around 1 mA and the irradiated area around 1 mm^2. The emitted Auger electrons are quantified by their kinetic energy using a cylindrical mirror analyzer (CMA). The Auger electrons reaching the detector are measured by an electron multiplier, in particular a channeltron. The measurement data is recorded using AugerScan software developed by RBD Instruments [110]. The scanning process included five scans of the sample in an energy range from 30 eV to 1200 eV. Subsequently, all acquired spectra were averaged to obtain a comprehensive representation. A qualitative evaluation is done by comparing the spectra with the spectra from the handbook of AES [111]. A quantitative evaluation was not made, because it was only about the classification of the correct element and a fluence analysis afterwards with RBS delivered more exact results.

5.3 Graphene characterization

To characterize the graphene after implantation, different techniques are used, which are briefly explained in this section. From these measurements, only the SKPM measurements were performed in Göttingen by the author of this thesis. The Raman, STM and LEED measurements were performed at the KU Leuven. For the XPS measurements the SuperESCA beamline at the Elettra synchrotron in Trieste was used. The ARPES measurements were also performed at the synchrotron in Trieste using the BaDElPh beamline.

5.3.1 Raman spectroscopy

Raman spectroscopy is a non-destructive method for the investigation of samples. It is based on the inelastic scattering of light and matter, in particular the scattering of photons by phonons [112]. Due to the surface sensitive analysis of solids, this method is a standard method for the investigation of 2D materials. The sample is irradiated with a monochromatic laser and the scattered light is detected. For graphene usually a wavelength between 400 nm and 700 nm is chosen to better detect the sp^2 bonds of the carbon [113] and to reduce damage to sample when using to high energetic photons. Various spectral lines can be observed in the detected spectrum. The frequency which is used for excitation and which is scattered by elastic Rayleigh scattering, a line with lower energy (Stokes shift) and one with higher energy (Anti-Stokes shift).These arise due to inelastic scattering from optical phonons or the interaction with the vibrational processes of the target molecules. For the generation of the Stoke line, a phonon is generated in the crystal lattice, which extracts energy from the light during scattering. The reversed process, i.e. the annihilation of a phonon, provides an increased energy of the light after scattering and an Anti-Stokes line is generated. The ratio of these two lines can be manipulated by temperature. At low temperature, only a few phonon states are occupied, so that the generation of a phonon and thus the formation of a Stokes shift is preferred. At higher temperatures, many phonons are present in the lattice, so the absorption of energy and the annihilation of a phonon is more likely.

In a Raman spectrum of defect-free single layer graphene, two peaks can be identified. These are the so-called G-peak, which originates from the E_{2G} mode at the Γ-point. At the Γ-point, the dual degeneracy E_{2g} mode describes both longitudinal optical (LO) and transverse optical (TO) phonons within the plane. This comprises of oscillations that reciprocate between the sublattices in graphene [114]. The G-peak is strongly influenced by strain effects and can give an impression of the curvature of the surface in the graphene. The G-peak has a wavenumber of $\nu = 1582\,\mathrm{cm}^{-1}$. The second peak is the 2D-peak, which in contrast to the G-peak is caused by a second-order two-phonon process. The shape of the 2D-peak can be used to determine whether the graphene is a single or multi-layer graphene, since the 2D-peak changes its shape and intensity with multiple layers, especially in relation to the G-peak. The 2D-peak occurs at wave numbers of $\nu \approx 2700\,\mathrm{cm}^{-1}$ [114].

By introducing defects into the graphene, the Raman spectrum changes in such a way that new peaks appear. On the one hand, this can lead to a splitting of the G-peak, with the D'-peak emerging at a wavenumber of $1620\,\mathrm{cm}^{-1}$, which is due to the localized vibrational modes at the defect. On the other hand, the D-Peak forms at a wavenumber of about $1300\,\mathrm{cm}^{-1}$. The ratio of intensity between the D-peak and the G-peak serves as a characteristic parameter for defect formation in graphene, as indicated by various studies [115–118]. Thus, Raman measurement provides a good picture of the damage to the graphene after ion implantation.

5.3.2 Low energy electron diffraction

Low energy electron diffraction (LEED) is another method for near-surface structural analysis of solids. Here, electrons with low energy ($< 500\,\mathrm{eV}$) [119] are shot vertically onto the sample surfaces. These scatter at the lattice atoms and are reflected back. Through an energy filter, only the elastically scattered electrons are selected and then accelerated onto a luminescent screen on which a diffraction pattern is formed. The crystal structure can then be determined from this pattern. In addition, the penetration depth can be increased by changing the electron energy, which means that, in the case of graphene, parts of the substrate can also be measured. This allows conclusions to be drawn about the quality or damage, of the graphene [23].

5.3.3 X-ray photoelectron spectroscopy

X-ray photoelectron spectroscopy (XPS) is a sophisticated surface-sensitive method for element determination. The photoelectric effect is exploited. A sample is irradiated with X-rays and the resulting photoelectric electrons are analyzed. From the kinetic energy of the electrons E_e and the work function ϕ of the material under investigation, the element-specific binding energy E_B can be deduced [72]:

$$E_B = E_\gamma + (E_e + \phi) \tag{5.13}$$

where E_γ represents the energy of the photons. Besides the identification of the chemical composition, XPS can also provide information about the chemical bonds in a system [72]. In the case of graphene, a difference between the sp^2 and sp^3 hybridization in the peak position of the C 1s level can be detected and used to some extent to investigate damage to the graphene, but due to the small difference and other artifacts, Raman is much more informative about the damage to the graphene [23].

5.3.4 Angle-resolved photoemission spectroscopy

Angle-resolved photoemission spectroscopy (ARPES) is based, like XPS, on the photoelectric effect. In contrast to XPS, however, not only the energy but also the angle at which the electrons leave the sample is measured. Furthermore, not the core electrons but the valence electrons are examined, which are emitted with significantly lower energies, corresponding to their lower binding energy. In this way, a determination of the energy-momentum relationship of the electron in the solid is possible. In the process of photoemission, the energy and momentum parallel $P_{||}$ to the surface are conserved, while the momentum perpendicular to the surface is not conserved [120]. By conservation of momentum parallel to the surface and the assumption that the photon momentum is negligible at the energies used, we obtain for the wave vector $K_{||}$ with the kinetic energy E_{kin} of the electrons and their mass m_e [120]

$$P_{||} = K_{||}\hbar = \sqrt{2m_e E_{kin}} \sin\theta. \tag{5.14}$$

From this, together with the determined binding energy E_B (similar to XPS), the band structure can be calculated.

5.3.5 Scanning tunneling microscopy

Scanning tunneling microscopy (STM) is based on the tunneling effect of electrons between a conducting tip and individual target atoms. For the measurement, an electrically conductive, at best atomically thin tip is moved over a sample, whereby the tip approaches the surface of the sample to within a few nanometers. The tunnel current is increased or decreased by minimal topological changes of the surface and thus slightly different distances between the sample and the tip d. In addition, the tunnel current is influenced by the work function Φ of the surface [121]. The tunnel current is calculated via [121]

$$I_{tun} \propto \exp\left(-2d\sqrt{2m_e\Phi/\hbar^2}\right) \approx \exp\left(-1.025\sqrt{\phi}d\right) \tag{5.15}$$

By means of STM, atomic resolutions can be achieved and thus foreign atoms or vacancies can be detected. Thus, the number of introduced foreign atoms can be estimated by simple counting directly via STM and important implantations parameters such as retained fluence can be determined [17].

5.3.6 Scanning kelvin probe microscopy

Scanning kelvin probe microscopy (SKPM) is an atomic force microscopy (AFM) based technique for determining the surface potential of a sample [122]. To measure this, a conductive probe is brought into the immediate vicinity of the sample surface by means of an AFM. Here, the Fermi levels of the cantilever material and the sample material equalize as electrons flow from the higher energy level to the lower one. The subsequent electron difference produces a contact voltage which is proportional to the work function Φ of the surface under investigation, which can be determined by [122]

$$V = \frac{\Delta\Phi}{e} = \frac{\Phi_{sample} - \Phi_{tip}}{e} \tag{5.16}$$

and e the elemental charge. in this work, SKPM measurements were used in this work to determine the sharpness of the transition region in lateral selective implantation of graphene (see 9.4).The implantation of foreign atoms changes the work function of the graphene, which allows the SKPM to measure the difference between implanted and unimplanted areas. No quantitative evaluations of the location of the fermi potential were made. The measurements were performed in Göttingen on an AFM of the Institute of Material Physics.

5.4 Programs

The simulation programs used are briefly explained below. First, there is IMINTDYN, which was used for the implantation simulations and the simulations for the HR-RBS evaluations. The special features of IMINTDYN are explained in more detail in chapter 7, since they are important for the understanding of the results and this section is only intended to provide a brief overview. Secondly, SIMNRA and GUPIX were used for the analysis of the RBS, NRA and PIXE spectra and furthermore, SIMION was used for the ion beam simulations, especially for the newly developed source.

5.4.1 IMINTDYN

For the simulation of implantation in 2D materials the program IMINTDYN [26, 123] was used. IMINTDYN is a further development of the program SDTrimSP from the Max-Planck-Institute for plasma physics [27]. This Monte Carlo program uses the binary collision approximation to simulate the collisions between the ions and the solid. Different potential methods for the energy loss calculation can be chosen.

A major advantage is the use of a new approach for the calculation of the sputtered particles, which was previously determined by means of a surface binding potential. Here, an ion must have a certain energy to leave the solid. Since there is no proper physical justification for the surface binding potential besides the better fitting to sputter data [124], an energy threshold , the so called bulk binding energy, was introduced, which is based on the sublimation energy of the material [123]. The bulk binding energy can be used here in complement to the surface binding energy [123]. Furthermore, the introduction of vacancies as new atomic species and a better distribution of the layers allow a much better simulation of thin layers.

Another advantage in the calculation of the penetration depth, especially compared to SRIM, is the use of simultanous weak collisions [26]. These ensure that not only the direct impact partner, but also the nearest to next-to-nearest neighbor are taken into account. A more detailed description of IMINTDYN and its new features are can be found later in this work in chapter 9.7

5.4.2 SIMNRA

SIMNRA [125] is a program to simulate RBS and NRA spectra and to fit experimentally measured data. It is possible to choose between different incident particles, like protons or helium nuclei. Furthermore, target materials of different thickness, composition and layers can be simulated. Additionally, the geometry of the measurement setup, such as angle of incidence and backscatter angle, as well as the energy of the incident particles and whether there is a shielding foil in front of the detector, can be adjusted. For the determination of the stopping power, SRIM is used and the energy of the scattered ions is calculated in SIMNRA. For the effective cross sections of the occurring reaction, either internally calculated Rutherford effective cross sections or self-inserted non-Rutherford effective cross sections can be used. Which cross sections are used in each case can be selected by the user. As a rule of thumb, for helium nuclei the normal Rutherford cross section can be used, while proton backscattering should be analyzed with experimentally determined cross sections. Nuclear reactions can also be studied as long as the necessary data of the effective cross sections are available. These can be determined using SigmaCalc2 [126], which takes into account both theoretical and experimentally determined cross sections. For measured spectra, a fit can be used to determine the energy calibration, the composition and thickness of the individual layers of a sample, and their surface roughness. The composition of the sample is given in at.%.

5.4.3 GUPIX

The evaluation of the PIXE spectra is done with the program GUPIX [127]. Herewith, the measured spectra can be adjusted and a quantitative elemental analysis can be performed. The elemental composition is determined from the intensities of the X-ray lines, which is why an energy calibration is indispensable. Furthermore, the program takes into account the absorption of the X-rays by the atmosphere in front of the detector. A calibration must also be carried out for this, whereby a foil made of platinum or a heavy element is suitable, where both L- and K-lines can be measured. By arranging the appropriate spacing and composition, it's possible to align the relationship between the K and L lines in a way that enables accurate concentration determination.

Another advantage of GUPIX is that also non-measurable elements like oxygen or carbon can be specified, which are used in the calculation of the concentrations. Here, the program calculates the composition of the sample from the valence of the invisible elements. Thus, it is assumed that every element in the sample is present as an oxide when oxygen is selected.

It should be noted that for single crystalline materials the absorption may be different from the calculated one and thus the concentration could be different. In contrast to SIMNRA, the concentrations given are in wt.%, which must be taken into account when comparing the two methods. In this work, GUPIX is used to identify the implanted elements, whereby a quantitative analysis is not performed due to the relatively low concentration in relation to the analyzed volume.

5.4.4 SIMION

SIMION [128] is a program used for calculating optical systems of ions or electrons. This involves computing both the electric fields within a system and the trajectories of charged particles. To achieve this, the simulation solves the Laplace equation at each location to determine the electrical potentials and electric fields at every position. Subsequently, charged particles can be defined, which are influenced by the electric fields and thus determine the trajectories of the particles within the system under consideration. The definition of the particles includes the mass, start position, energy and charge state. A big advantage of SIMION is that CAD drawings can be read in as electrodes, so it is possible to make an accurate simulation of the desired setup. However, when considering the electric fields, only fields in vacuum are assumed.

SIMION was used in this work to simulate the newly developed source and to determine the trajectories and energy of the ions inside the source (see 6.4.1.1).

6 Ion accelerator ADONIS

In the following chapter the ion implanter ADONIS (Anlage zur DepOsition von Niederenegetischer Ionen auf Substrate) (ch. 6.1) and the ion source used for this research are described (ch. 6.3). Special attention is given to the new modifications to the source developed during this research to provide hitherto unavailable elements for the implantation (ch. 6.4.1), as well as the special deceleration unit, which allows a lateral inhomogeneous implantation (ch. 6.5). Additionally, implantations for testing these new features are presented. For this purpose, RBS, PIXE and Auger measurements were performed. Finally, the new Arduino-based process control is explained, which was built and programmed to upgrade the old system.

6.1 Beam Line

In Fig. 6.1 a schematic illustration of ADONIS is given. Roughly, the accelerator can be divided into three parts, the source region, which is at 30 kV and in which the ion beam is generated, the actual beam line, in which the beam can be focused and mass separated with the aid of lenses, deflectors and a 90°-magnet, and the deceleration unit, in which the beam is decelerated and the sample is implanted. To generate the ion beam, a hollow cathode hot filament source [129] or its further development a sputter hollow cathode ion source [24] is used. For the extraction and concentration of ions from the plasma of the source, a grounded electrode is placed opposite the outlet of the source. The acceleration of the ions with 30 kV is done so that as many ions as possible can be extracted from the source. A lower voltage would result in a greatly reduced beam current and some elements that do not have a high intensity in the first place could not be made available as an ion beam. Already from 20 kV a significant reduction of the beam current can be measured. Thus, it is not possible to generate an ion beam with a few 10 eV from the source, but it must be generated with increased energy and decelerated in front of the target. After the extraction out of the source, the beam passes through a cylindrical lens and is mass separated by a 90°-magnet with a mass resolution of $M/\Delta M = 150$. The mass selection is followed by capacitors for beam positioning, another Einzel lens and a quadrupole lens for beam focusing. To remove neutral particles from the beam, the beam is electrostatically deflected by 5° before entering the ultra-high vacuum. In the ultra-high vacuum a beam sweep ensures that the beam irradiates a homogeneous surface. In this process, the beam is first deflected by several plate capacitors to which an alternating voltage is applied, and then parallelized again. The beam is expanded and homogenized to such an extent that an aperture then limits the beam to an area of 2.5 cm^2. Thus, edge effects due to the beam sweep are irrelevant. In front of the decelerating unit is an electron lens, which deflects possible electrons with -4 kV. These electrons can be generated as secondary electrons by the unattended irradiation of beam tube parts. Since the target is at +30kV, these would also be accelerated to it and thus corrupt the current measurement. The beam then enters the deceleration unit, where it is decelerated to the desired maximum energy and the samples are implanted. Typical values for the focusing are 15-22 kV for the first einzel lens, 0-13 kV for the second, 1.6-1.9 kV for the quadrupole lens and 0-200 V for the xy-deflector. To insert a sample into the implantation chamber, a load lock system is available, where a vacuum of $1 \times 10^{-7} - 1 \times 10^{-8}$ mbar is reached, before the sample is transfered into the ultra-high vacuum ($5 \times 10^{-9} - 8 \times 10^{-10}$ mbar). The sample manipulation is done by magnetic linear and rotation manipulators.

Besides ion implantation, also growth of thin films are possible. Ions with energy around 200 eV are deposited on a substrate. This technique can be used to produce ta-C or BN layers. Due to the mass separation, these layers can be isotopically pure, e.g. pure ^{11}B layers. A detailed description of the accelerator can also be found in [22, 130].

6.2 Deceleration unit

In order to implant the ions with energies down to 10 eV, they have to be decelerated. For this purpose, a deceleration unit is included in the implantation chamber. The main idea is to put the sample on the same potential as the anode in the source, since there the ions with the most energy are created. In addition, a small negative voltage with respect to the high voltage is applied to the sample, which should correspond to the maximum energy of the ions. In Fig. 6.7 the implantation current, i.e. the current on the sample, is plotted against the additional applied voltage. It can be clearly seen that at 0 V, which corresponds to a potential on the sample equal to the anode potential, no current arrives and thus all particles are deflected. As soon as a voltage is applied, the current increases sharply until it reaches saturation. From this measurement it can be concluded that the maximum energy of implanted ions corresponds to the applied voltage. The deceleration unit also underwent an upgrade to improve the steering of the ions. Additionally, improvements were made to the insulators, the electrical connections

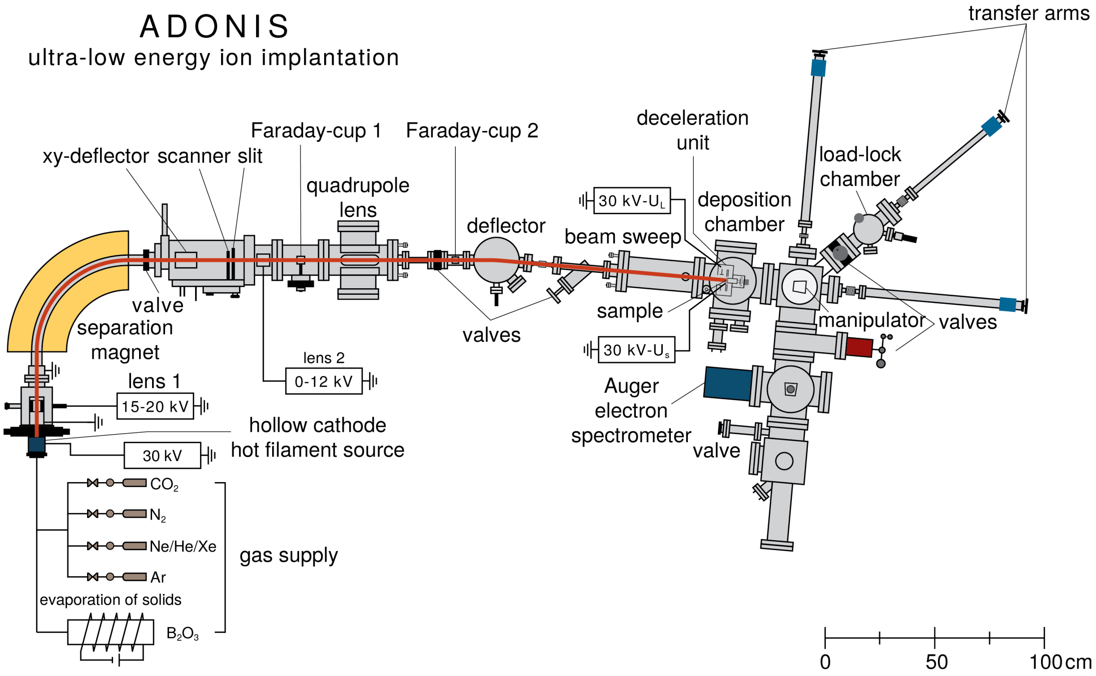

Figure 6.1: *Schematic representation of the ADONIS ion implantation system. The beam starts in the ion source, is mass-separated in the 90°-magnet and passes through different lenses. Deceleration occurs in the separation chamber. Auger spectroscopy is possible before and after implantation without leaving the vacuum. (Illustration done by Manuel Auge and used with his permission. Original in [22])*

and the vacuum feedthroughs, in particular to prevent and suppress leakage currents. These could occur, for instance, when there was an excessive voltage differential between the electron lens and the deceleration unit, coupled with a sharp bend in the supplying cable, leading to corona discharges, or when the insulators were contaminated. A description of the upgraded deceleration unit can be also found in [22] and [25].

6.3 Ion source

The following paragraphs, 6.3 and 6.4.1, can be also found in the publication [24][1]. The normal ion source is a conventional hollow cathode hot filament source [129] which corresponds to the Model SO-55 from High Voltage Engineering. The setup with typical potentials is shown in Figure 6.2a.

From left to right it consists of a graphite anode with gas feed, which is separated from the tantalum cathode by a boron nitride insulator. This in turn is separated from a graphite cap

---

[1] The corresponding text passages in this paper were prepared by the author of this thesis

by means of a BN insulator. The hollow cathode is formed by the tantalum ring, the graphite cap and the tungsten filament that sits in between. The use of graphite for the anode and cap as well as the separation of the conductive parts by stronger boron nitride insulators represents a modification to the the Model SO-55. The filament is heated with 25 A and emits electrons via thermionic emission, which are then accelerated to the anode and ignite an Ar plasma in the small volume in the area between the graphite anode and the tantalum cathode. The anode voltage drops to 25-35 V after ignition, which describes the maximum energy the ions have, if they are generated directly in front of the anode. Further away from the cathode they have a smaller energy. Therefore, the maximum energy of the ions out of the source (before acceleration) corresponds to the anode voltage (25-35 V) with a tail to lower energies. The circular extraction hole with 0.8 mm diameter generates a point-like beam source, which ensures that the beam can be very well focused.

The desired elements can be fed into the plasma both as a gas or by evaporating from solids with an oven (not shown) into the gas stream. The ions are subsequently extracted from the source by a 30 kV high voltage. Although a wide range of elements can already be produced with the described source design, its use is limited for materials with high melting points or low gas pressure. To circumvent this disadvantage, a sputtering cathode is introduced into the source underneath the anode, which contains a small disk of the material to be implanted [24]. In Fig. 6.3 all possible implantation elements are shown. The elements marked with a star are available due to the new ion source.

6.4 Improvements and tests

In the following, the improvements and new developments concerning the hardware of the ADONIS accelerator and the tests carried out on these improvements will be explained in more detail.

6.4.1 Development of the Sputter hollow cathode ion source

The aforementioned source design was modified by incorporating a stainless steel sputtering cathode, as shown in Fig. 6.2b. A sputtering target in the form of a disk can be integrated into this cathode. Moreover, the graphite anode was replaced by a tantalum anode because of the better durability and difficult to build shape.

The sputter cathode in the new design is placed behind (in viewpoint of the ion extraction) the plasma and a voltage up to -2 kV (-1 kV under normal conditions) can be applied with

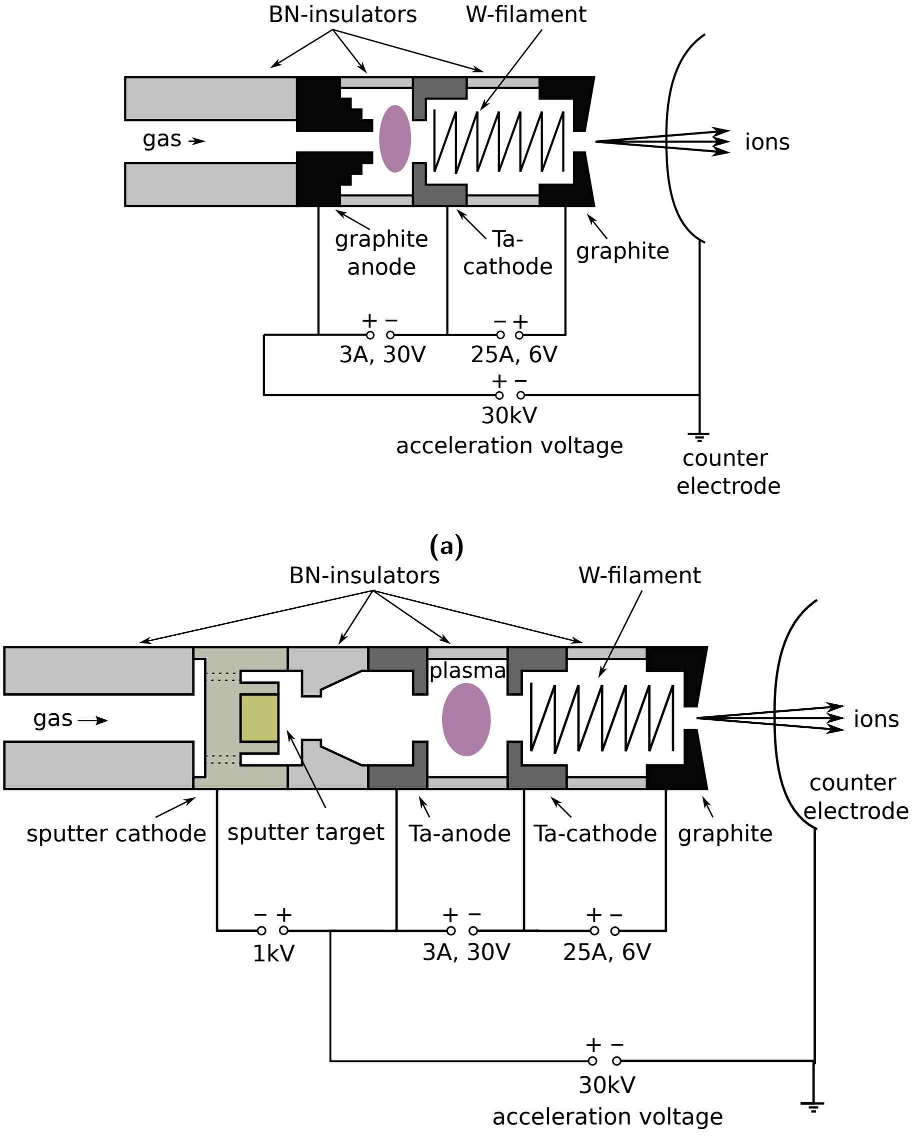

(a)

(b)

Figure 6.2: *(a) Schematic of the conventional hollow cathode hot filament source with the typical potentials. (b) Scheme of the modified ion source by including a sputter cathode. The sputter cathode in the new source is placed behind (in viewpoint of the ion extraction) the plasma and a voltage of around to -1 kV can be applied, in respect to the anode. Figure also published in [24]*

respect to the anode. In order to electrical insulate the tantalum anode and the sputter cathode a new insulator was designed. The height of the insulator was increased from 4 mm to 5 mm compared to the previously used source to optimize the distance between the tantalum cathode and anode. The gas supply through the sputter cathode is ensured by four 0.5 mm wide holes next to the sputter target (dotted line in Fig. 6.2b).

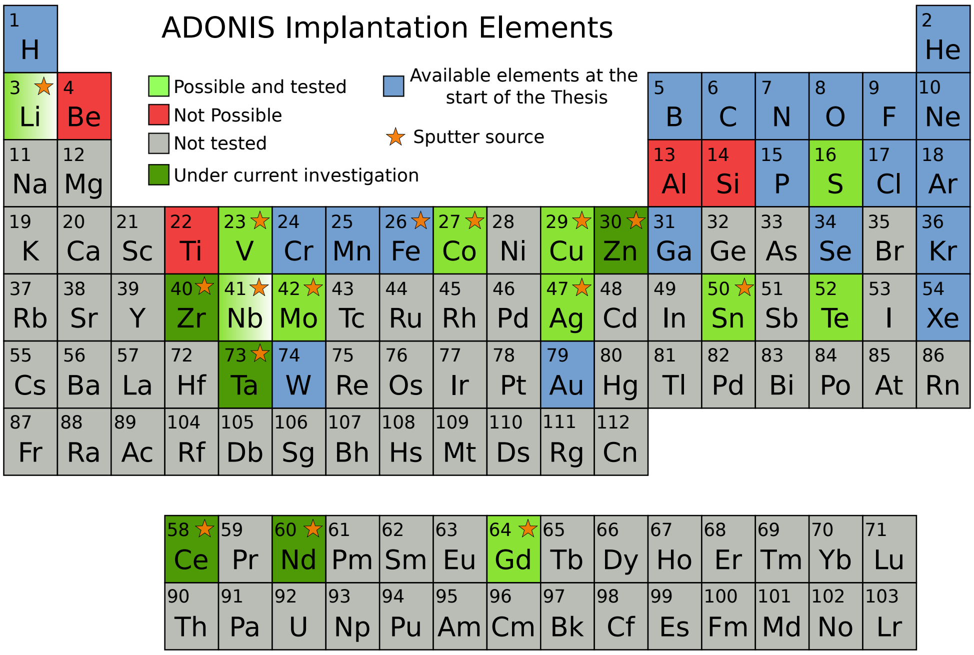

Figure 6.3: *Available elements for ADONIS. Not possible are Be, due to its strong toxicity and difficult handling,* Al *because no clean mass separation is possible between* $^{27}\mathrm{Al}$ *and* $^{11}\mathrm{BO}$ *and* Al *has only one stable isotope.* $^{28}\mathrm{Si}$ *due to mass overlap with* $\mathrm{N_2}$ *and* CO *and titanium due to formation of* TiN *in the source.* $^{93}\mathrm{Nb}$*, the only stable* Nb *isotope, has a mass overlap with* W^{2+} *and* Li *one with* N^{2+}*, which can be circumvented (see 6.4.2 and 6.4.2). Fe is also possible with the normal source, but supplies significantly higher currents with the sputter source.*

The idea of this design is similar to the concept of the Penning ion source (PIG), which operates at Anode voltages of 1 keV up to 7.5 keV [131]. This leads to a large energy spread and is only useful for post-acceleration to high energies. Here, the existing Ar plasma is used both for sputtering and to ionize the particles. Some of the Ar^+-ions are extracted out of the plasma and accelerate towards the cathode, in which a sputter target is placed. As a result of Ar ion impact, part of the target elements are sputtered out and transferred to the plasma. In the plasma, the target atoms get ionized and are subsequently extracted by the high voltage, to get accelerated towards the separation magnet. For igniting the plasma an Ar pressure in the range of 10^{-5} mbar was used. Since the voltage drop at the anode is the same as from the old source, the maximum energy is also 25-35 eV with a tail to lower energies. However, since the deceleration voltage uses the anode potential as a reference, a sharp energy distribution can be set for implantation. In addition, a point-shaped beam can be achieved by using the same extraction aperture (0.8 mm) as the old source [24].

6.4.1.1 Simulation

For a better understanding of the processes inside the new ion source, simulations using SIMION [128] were performed. Therefore, the CAD drawings of the source tower were converted into a potential array. In the simulation, the Laplace equation gets solved for every place to get the electrical potentials and the electrical field at every position inside the source. In figure 6.4 the simulation is presented. The red lines show the trajectories of the Ar^+ ions that get created in the plasma between the Ta-anode and Ta-cathode. Most of the ions get extracted due to the 30 kV to the right side out of the source, but some of them are accelerated towards the sputter target (left of the plasma). Since the dimensions corresponds to the real source, this confirms, that the 1 kV is sufficient to shape the electric field in a way that ions will reach the sputter target and therefore hit atoms out of it.

The simulation was used to determine the fraction of ions generated in the plasma that is accelerated to the sputter cathode. For this purpose, SIMION was used to define a cylinder in the area between the Ta-anode and Ta-cathode in which the ions are generated. The trajectory was then calculated and the ions reaching the sputter target were counted. Then the voltage applied to the sputter cathode was changed and the whole process was repeated. A total of 10000 ions were generated per simulation. The fraction of ions versus the applied voltage is shown in Figure 6.5a. To support the simulation with an experiment, the Mo current extracted from the source was measured as a function of the applied voltage and plotted in Figure 6.5b.

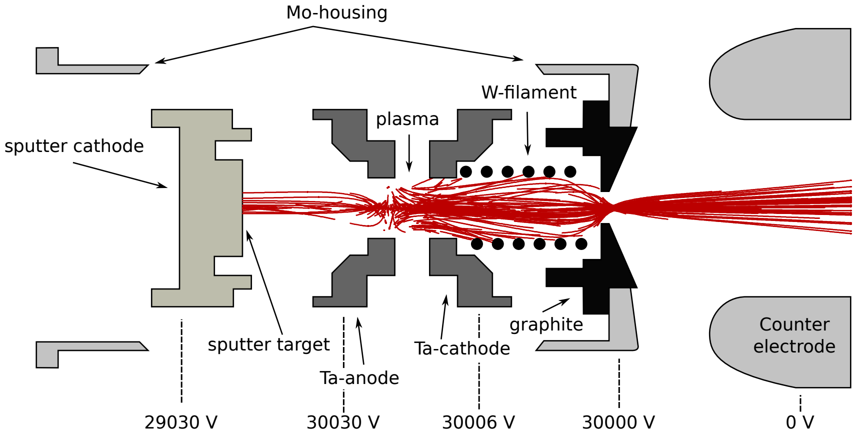

Figure 6.4: *SIMION simulation of the source during operation. The argon ions (red) generated in the plasma between the Ta-anode and the Ta-cathode are shown in red. Most of the ions are accelerated out of the source towards the counter electrode, while a smaller fraction of the ions is accelerated onto the sputter target where they sputter out particles. Figure also published in [24].*

It can be seen that both, simulation and experiment, require a certain offset voltage for particles to be sputtered from the target. This is because the electric field must first propagate to the plasma, which is somewhat shielded by the Ta-cathode, before it can extract ions. Subsequently, more and more ions are accelerated towards the target and thus more particles are extracted from it.

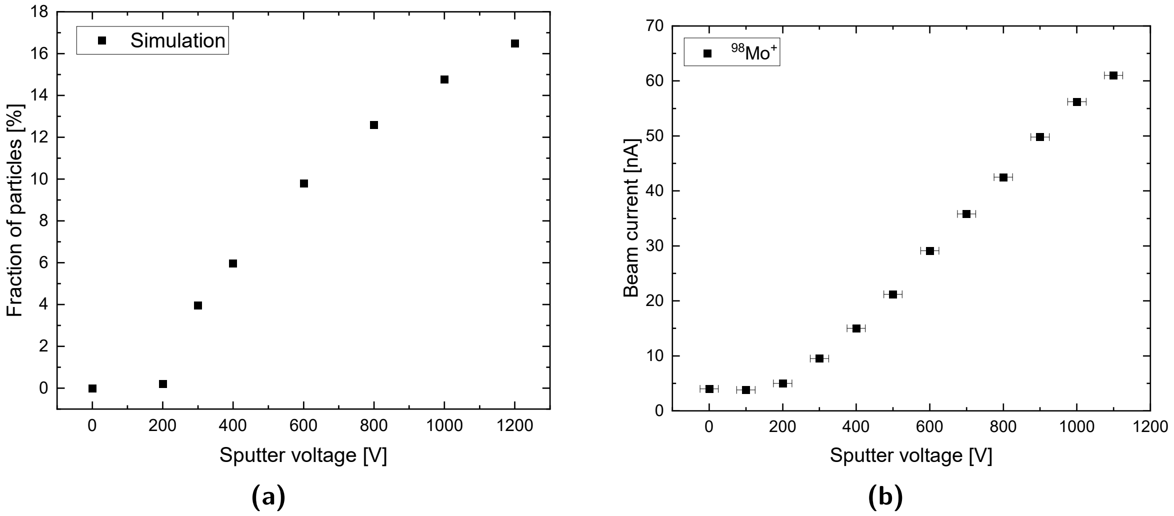

Figure 6.5: *(a) Simulated fraction of particles generated in the plasma that get extracted towards the sputter target. (b) Molybdenum current after the 90°-magnet versus the applied sputter voltage. It can be seen that a certain offset is required. Figure also published in [24]*

Energy distribution out of the Source and on the target An important point when implanting in 2D materials is the accuracy of the selected implantation energy, so a too high voltage on the one hand can cause the ions to fly through the layer and also that the layer is damaged more, on the other hand, too low is bad because the displacement energy of the target atoms may not be reached and substitutional incooperation is suppressed. Since the deceleration voltage is applied in respect to the anode voltage, this is the maximum energy the ions can have. However, since there is a potential gradient within the source between the anode and the filament, the positive ions may not be generated directly at the anode but somewhere in the plasma and thus may not have the maximum energy. SIMION simulations were also performed to estimate the energy distribution from the source. A typical voltage drop of 40 V between the filament and the anode was assumed, which occurs when the plasma is ignited. The range of ion generation was a cylinder distribution starting at 15 eV e^- energy, since this corresponds to the energy at which the electrons can overcome the ionization energy of argon. It should be noted that SIMION cannot take into account the plasma potential and therefore this is only an estimate. In addition, a different range would have to be selected for each ion, since the ionization energies are different. The energy profiles for the old and the sputter source with an sputter voltage of 1 kV of the ions for an implantation energy of 20 eV are shown in Fig. 6.6. It can be clearly seen that most ions are extracted at around 15 eV, so about 5 eV below the set energy for the normal source. For the new sputter source, this effect is even more enhanced, so that the maximum is at about 11 eV. In reality, due to the plasma potential, probably more particles will be at the maximum energy. The mass separation, which also corresponds to an energy selection, has hardly any influence on the energy distribution of the ions in the beam, since a difference of 5 eV-20 eV cannot be resolved and is always focused on the maximum beam current of an isotope.

In order to obtain a further estimate of the energy of the ions on the target, the measured target current can also be checked against the applied implantation voltage. Ideally, this should also be 0 A at 0 V. If there would be current at 0 V, there is most likely an error in the contacts, so that a lower voltage drop at the target and thus the ions are not slowed down as much as they should be. In addition, it can happen that electrons are removed from the target and thus a positive current is measured. This happens especially during hot implantation due to the heated specimen holder. In order to verify this, however, the current must also occur with the beam switched off and increase with higher targets voltage.

If the current already drops to 0 A at higher voltage values, this can have two main causes. On the one hand, it can happen that electrons hit the target and are not completely deflected if the negative voltage of the target is too weak, thus falsifying the current measurement. On

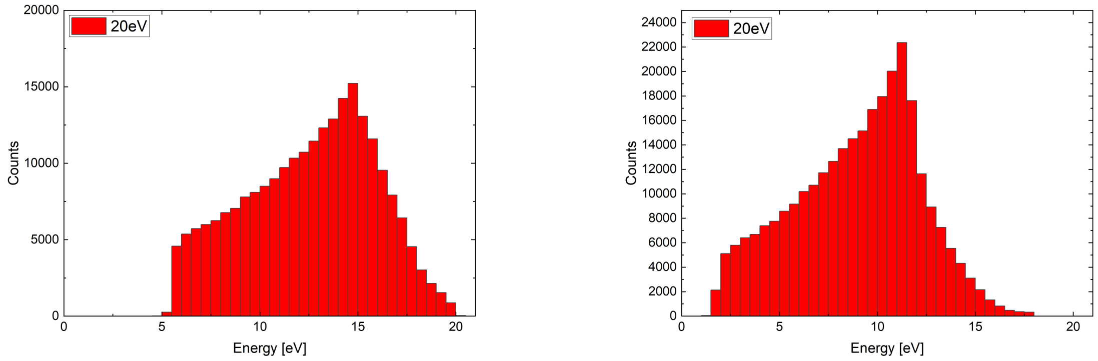

(a) **(b)**

Figure 6.6: *(a) Energy distribution of ions for a 20 eV implantation using the normal ion source according to SIMION. (b) Energy spread of ions for a 20 eV implantation using the sputter ion source with -1 kV at the sputter cathode according to SIMION.*

the other hand, it is possible that the ions from the source have too little energy and can no longer reach the target. This can happen if they are not generated directly at the anode but in the area between the anode and the filament. The first case occurs mainly when insulators between individual parts in the deceleration unit are no longer perfectly insulating due to contamination. Electrons present in the beam due to secondary electrons from collisions with residual gas molecules or collisions with beam line parts are removed from the beam on the electron lens, which is at -4 kV to -5 kV, before they reach the deceleration unit and are further accelerated by it at 30 kV. Secondary electrons which are emitted inside the deceleration unit are also removed by the negative charged defocusing lens in front of the target. This also ensures that secondary electrons from the target are suppressed. In the case of electrons, a negative current is then measured, which does not occur if the ions have too less energy as in the second case.

Figure 6.7 shows the argon current on the target versus the applied target voltage. It can be seen that the current drops significantly starting at 60 V bias and drops to 0 μA at 5 V and then remains 0 μA. This indicates that the ions have a lower energy by about 5 eV than indicated by the target voltage. For the measurement, the sputter source was used with -1 kV at the sputter target to match the simulations (Fig. 6.6b). The value of approximately 5 V does not precisely align with the results obtained from the simulations. However, it is worth noting that SIMION does not account for plasma potential. Nevertheless, a similar trend is evident, as the ions arrive at the target with slightly reduced energy. It should be noted that even at 5 V some current can still arrive at the target, but the measuring range of the analog current integrator does not have sufficient measuring accuracy. In addition, the value of 5 V is not constant but can drop to 1 V depending on the type of ion, the type of source, how well refocusing is done, and in general how good the electrical contacts inside the source and to the target are.

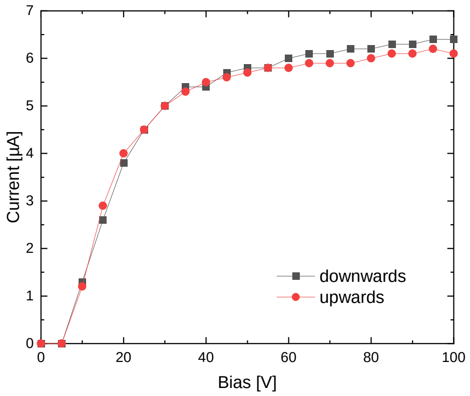

Figure 6.7: *Ar current on the target, at different implantation voltages. For the red points, the voltage was started at 0 V and increased, and then reduced again for the black points. Due to the measurement accuracy of the current integrator in the current range under consideration, no current below 5 V can be measured.*

6.4.2 Test Implantations

To test the new source, two materials, molybdenum and iron, were used as sputter targets. Due to the high melting point and low vapor pressure molybdenum was also chosen to proof, that the particles get sputtered out of the target and not only evaporate due to an extra heat source when some current flows to the sputter cathode. Iron was chosen because in the normal source nearly no iron is seen in the mass spectrum. In the following, the most interesting source materials are presented, where sometimes the usual parameters differed, unexpected things happened or more exotic elements were explored. These include Fe, Mo, Nb, Gd, V, Ti and Li.

In table 6.1, implantations of selected elements provided by the new sputter source with achieved currents are presented. This table is also published in [24] and was prepared by the author of this work. In summary, the achieved currents are sufficient for implantations in 2D materials, where fluences higher than 1×10^{15} at/cm^2 are rarely used. For example at 100 nA beam current an implantation of 1×10^{15} at/cm^2 takes around 67 min. Furthermore, an overlap between the measured fluence and the fluence determined during implantation can be seen

Table 6.1: *Implanted Isotopes provided by the new ion source, with the achieved implantation current, the used energy, the implanted fluence (current integration), measured fluence (RBS) and the used substrate material. The errors from the measured fluence corresponds to the fit errors given by SIMNRA. (Slightly adapted from [24]).*

Isotope	Current [nA]	Fluence (c. i.) [10^{14} $^{at}/_{cm^2}$]	Fluence (RBS) [10^{14} $^{at}/_{cm^2}$]	Implantation Energy [eV]	Substrate
^{51}V	80-100	4	4.5(2)	25	Si(p-doped)
^{56}Fe	900	40	39.8(4)	20	ta-C
^{59}Co	800	10	9.9(2)	20	ta-C/graphene
^{93}Nb	100-200	10	6.23(1)	25	Si(p-doped)
^{98}Mo	50-70	10	9.9(2)	100	Si(n-doped)
^{158}Gd	20-40	5.5	5.4(3)	25	ta-C

via the current integration even at energies down to 20 eV. The only exception is Nb, which is due to co-implantation with W^{2+} (see 6.4.2), which cannot be distinguished in the current measurement but can be determined by RBS.

Iron-Source For the iron test, the graphite cathode was used, to only get the iron out of the target and not the cathode itself. As a target a normal steel nail was inserted into the middle hole of the cathode and a voltage of -1 kV was applied to it after the plasma was ignited. Because the most prominent stable Fe isotopes, $^{56}\mathrm{Fe}$ (91.72 %) and $^{54}\mathrm{Fe}$ (5.8 %), is hard to separate from only stable $^{55}\mathrm{Mn}$ in the mass spectra, it was implanted into a ta-C layer using an implantation energy of 20 eV to examine the beam purity afterwards.
Auger spectroscopy, RBS (figure 6.8), and PIXE (figure 6.9) measurements were performed to examine if and how much iron was implanted into the sample. The AES measurement showed clear peaks in the energy range typical for iron [111]. However, since these are very close to the peaks for manganese, it was not possible to make any clear statements. The RBS measurement shows a clear peak at values that represents iron. Also the area under the graph matches to the implanted amount of $4 \times 10^{15}\, ^{at}/_{cm^2}$, but since this requires an exact energy calibration, a PIXE measurement was carried out to finally show which element was implanted. The PIXE measurement shows, beside the silicon Peak, only X-rays from iron, which proofs that only iron was implanted.
With this source for Fe ions, implantation currents of around 1 μA could be achieved. For even higher Fe currents the normal stainless steel sputter cathode can be used.

Molybdenum-Source For the molybdenum-source, the stainless steel sputter cathode was used. A disk made of pure molybdenum severed as a sputter target and was inserted in the recess in the center of the cathode. Once again high voltage of -1 kV was applied to the cathode, which dropped slowly to around 600 V during the implantation process. One reason

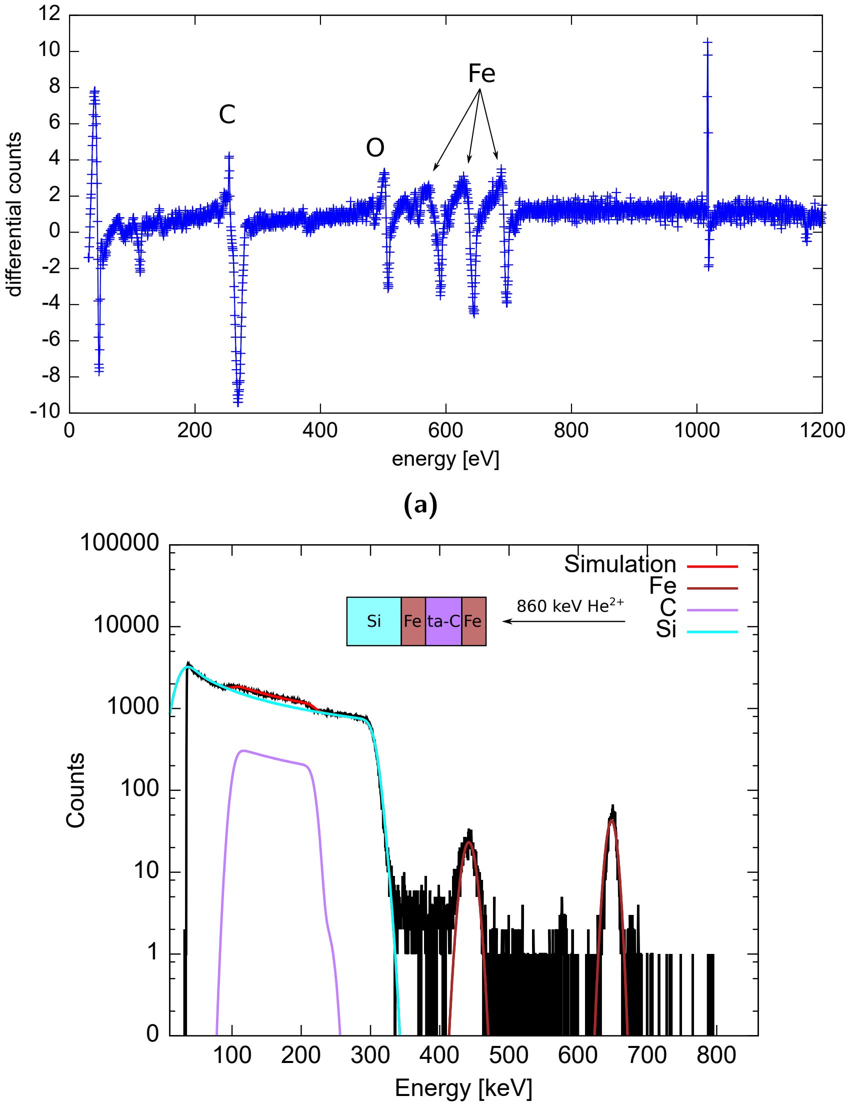

(a)

(b)

Figure 6.8: *(a) auger spectrum of iron implanted ta-C sample right after the implantation. (b) RBS spectrum of the same sample. The Fe Peak between the ta-C and the Si substrate, is due to a contamination which occurs during the coating process of the wafer. The position of this peak clearly indicates that this Fe lies under the ty-C layer and therefore has no influence on the implantation. Here, 860 keV* He^{2+} *ions and a backscattering angle of 165° were used.*

for the voltage drop could be, that the insulator was coated with molybdenum over time and thus became slightly conductive. This is indicated by the fact that the insulator had a silvery shiny containing layer after the implantation, which was identified as Mo via PIXE.

In order to measure the performance of the source, two mass spectra were measured, one with

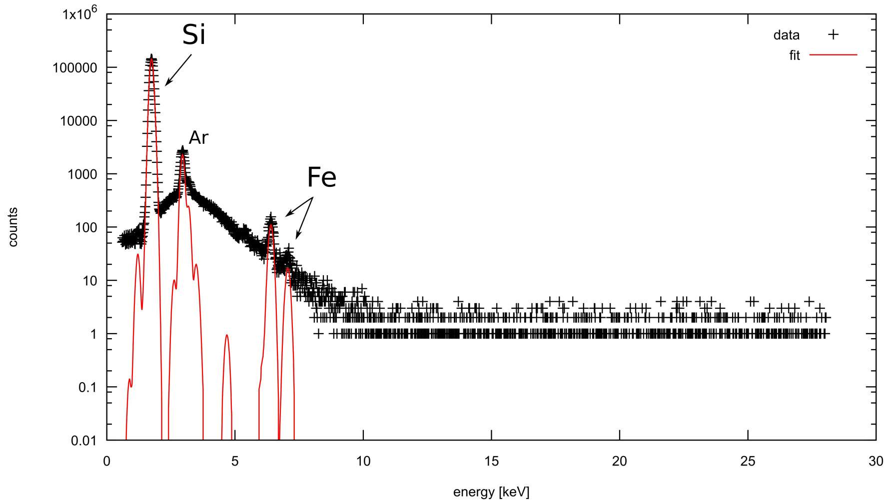

Figure 6.9: *PIXE spectrum of the implanted ta-C sample with the Fe K lines at 6.4 keV (K_α) and 7.06 keV (K_β). The Mn peaks would occur at 5.9 keV (K_α) and 6.49 keV (K_β) X-ray energy. 2500 keV protons were used for this measurement.*

and one without voltage on the sputter cathode. In figure 6.10 the section of the spectra where molybdenum should be present is shown.

From the mass analysis It is clear that molybdenum is only present, when the high voltage is applied. The peaks at lower magnetic field, which are in both spectra, corresponds to W^{2+} isotopes. The tungsten comes out of the filament. The increase of one of the tungsten peaks is caused by a superposition of the stable isotopes $^{184}W^{2+}$ and $^{92}Mo^{+}$. Although, the fingerprint of the molybdenum isotopes in the mass spectra proofs that the source provides molybdenum, an implantation into a Silicon wafer was performed and Auger, RBS (Fig. 6.11), and PIXE (Fig. 6.12) measurements were conducted.

All three measurements show the presence of molybdenum in the sample. For the PIXE analysis, a 24 μm aluminum absorber in front of the detector was used, in order to filter out low energy X-rays to get a better resolution for the molybdenum X-rays. Therefore, the high peak at low energy corresponds to aluminum X-rays generated due to X-ray fluorescence and the silicon peaks are filtered out. The arsenic peaks are present because n-doped silicon was used as a sample.

With this source implantation currents up to 70 nA could be achieved. However, after some time the current starts to drop, when the insulator gets coated with a conductive layer and therefore the high voltage at the sputter cathode drops.

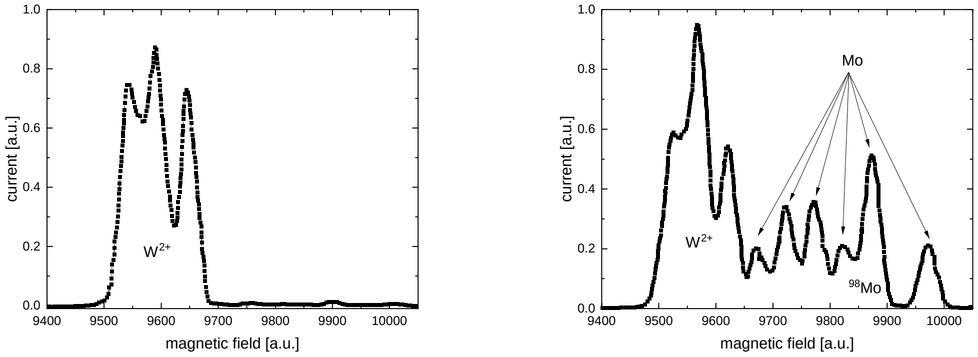

(a) **(b)**

Figure 6.10: *(a) The mass spectrum the of Mo-Source without an applied sputter voltage. The three peaks are double charged W ions from the filament. (b) The mass spectrum with an applied sputter voltage. The new peaks correspond to the Mo isotopes. The increase in the* $^{184}W^{2+}$ *come due to a superposition with* $^{92}Mo^{+}$*. (The mass spectra was digitalzied with WebPlotDigitizer [132].)*

Niobium-Source As another element with a high melting point (2477°C) niobium was chosen to extend the elements provided by the sputter source. Therefore, a 1 mm thick and 4 mm in diameter Nb disc was made and used as a sputter target. Furthermore a p-doped Silicon wafer was used as substrate for an test implantation of $1 \times 10^{15} at/cm^2$.

In Figure 6.13, the RBS spectrum of the test implantation is shown. Besides the Nb peak, a W peak is visible. This comes due to an overlap of the only stable ^{93}Nb isotope with the double charged ^{186}W isotope. The relation between Nb and W is 3/4 Nb to 1/4 W. The maximum mixed implantation current was 200 nA. The presence of Nb and W could be also confirmed by PIXE and Auger measurements.

If implantations are performed with niobium, either a different filament material must be selected or the energy must be chosen so that the tungsten penetrates significantly deeper into the sample. This is due to the double charge and thus the double implantation energy of the tungsten.

SRIM simulations show, on the one hand, that the penetration depth of 20 eV Nb in carbon is 4.3 nm. On the other hand, tungsten with 40 eV has a penetration depth of 6.7 nm. Therefore, the energy can be chosen that niobium is stuck in the first atomic layer, while tungsten is implanted into the substrate.

Further tests to verify the ratio between Nb and W are planed to calculate the exact charge that is needed for a given Nb fluence.

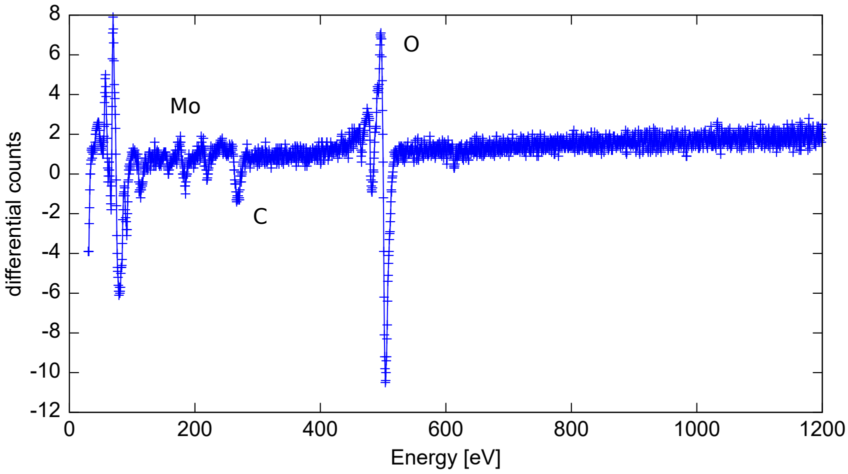

(a)

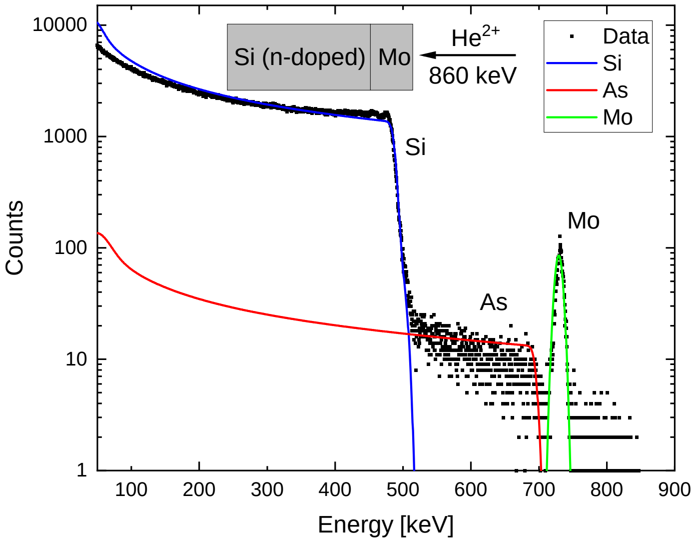

(b)

Figure 6.11: *(a) Auger spectrum of molybdenum implanted silicon wafer directly after the implantation. (b) RBS spectrum of the same sample. 860 keV He^{2+} ions and a backscattering angle of 165° were used.*

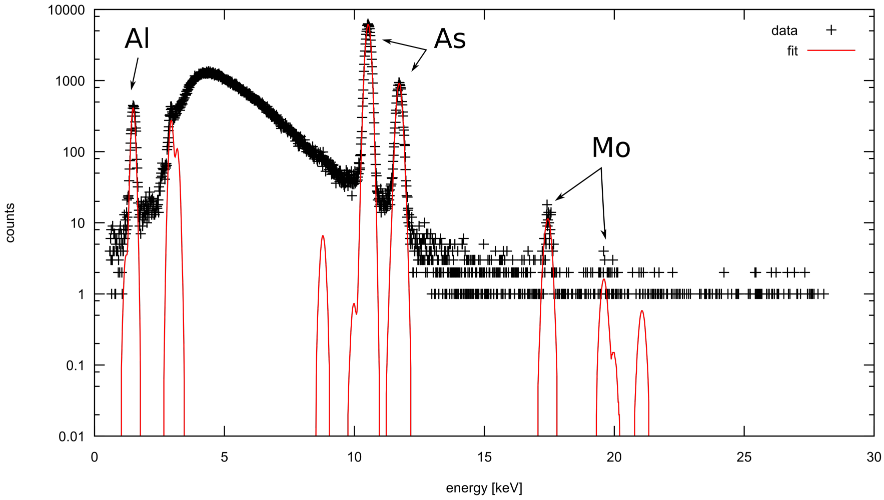

Figure 6.12: *PIXE spectrum of the implanted silicon wafer. For better resolution in the higher energy part, a 24 μm aluminum foil was used as an absorber in front of the detector. The arsenic peaks results ot of the n-doping of the silicon wafer.*

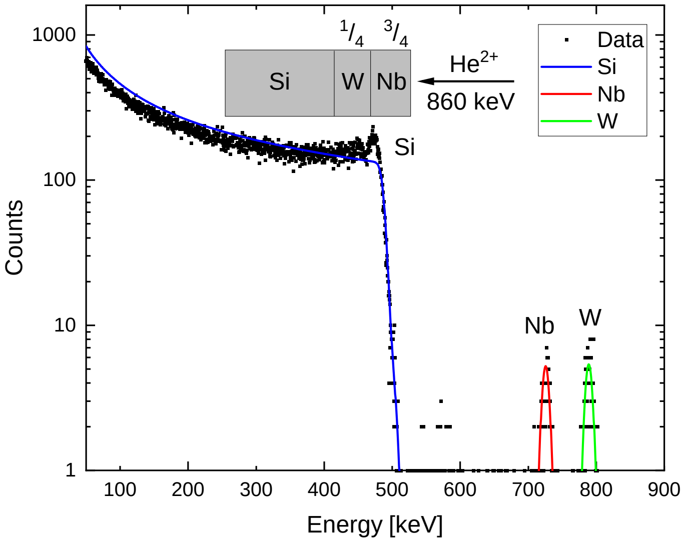

Figure 6.13: *RBS spectrum of implanted Nb in p-doped Si. The W peak originates in co-implantation with W^{2+} due to the same mass to charge ratio. The ratio between Nb and W is 0.75 to 0.25.*

Gadolinium-Source As a first test with rare earth elements, a rough piece of gadolinium was used as a sputter target. However, when voltage was applied to the sputtering cathode, a short circuit occurred almost immediately and no Gd current could be extracted. When the source was removed, it was found that the Gd and part of the stainless steel cathode were destroyed. It is assumed that an arc discharge was formed, which heated the Gd and the cathode to such an extent that both parts melted or evaporated. In addition, the BN insulator was welded directly to the Ta-anode at the sputter cathode, which can be attributed to the fact that the Gd and missing stainless steel was deposited there. In order to still have a Gd source available, a source was then constructed in which a thin Gd foil was placed directly on the graphite anode. Here also, no current could be extracted and the foil was completely used up after a short time. Only after using a very smooth Gd disk inside the sputter source a small Gd current of 20 nA could be extracted and used for implantation. This indicates, that the distances in the source might be a little to small and that high electric field at sharp edges may lead to discharges. However, a disadvantage when the dimensions are chosen larger, however, is that the sputter yield decreases and thus the generated currents lose intensity.

Vanadium-Source In order to realize a Vanadium source, a piece of vanadium oxide was placed in the sputtering cathode. Despite the imperfect shape and the oxide layer, an acceptable implantation current of 50-100 nA was achieved. In addition to the use of vanadium oxide, a disc of pure vanadium can also be used. In this case, however, the current achieved fell to 10-20 nA on the target. This can be explained by the lower stability of Vanadium oxide. While pure vanadium has a melting point of 1910 °C, the most stable oxide (V_2O_5) has a melting point of 690 °C and a decomposition temperature of 1750 °C. The existence of vanadium was again confirmed by PIXE and RBS.
One thing to consider with the Vanadium sputter source is the proper mass resolution setting when using a stainless steel sputter cathode. Since the most commonly used stainless steel, V2A, is chromium-nickel steel, a chromium current is also observed. This is caused by sputtering of the cathode itself as well as by normal thermal evaporation of chromium from the alloy. Chromium and vanadium are only one atomic mass apart (^{51}V vs. ^{52}Cr). The reading of the magnetic field from the mass separating magnet may also drift over time, so a mass spectrum should be plotted prior to any V implantation to avoid contamination with Cr. Another possibility would be to use a tantalum cathode.

Titanium-Source In order to get Titanium ions out of the source, a Ti-disc was made and used as a sputter target. Despite a normal function of the source and the accelerator no Ti current could be measured. This is probably due to the formation of TiN inside the source. Since nitrogen, out of the BN insulators, is present in the source and the reaction of Ti and N is highly efficient under the conditions inside the source, all of the sputtered Ti reacts. A strong indication for this is the gold-colored layer that formed on all source parts even on the sputter target. To confirm this RBS-measurements of these gold colored layers are planned. To avoid the formation of TiN and to get a running Ti source, the BN insulators must be replaced with nitrogen free ceramics.

Lithium-Source The sputter source can also be used to provide lithium. However, since lithium has a high vapor pressure with a melting temperature of about 181°C, an additional voltage at the sputter cathode is not necessary. The heat generated by the plasma is sufficient to vaporize enough Li and make it available as an ion beam. A challenge is the mass separation, because Li with a mass of 6 or 7 amu overlaps with N^{2+} or C^{2+}. Since the insulators are made of BN and there is always residual carbon in the source, N and C contamination are present. For a pure ^{7}Li-beam it is therefore important to operate the source in such a way that the anode voltage is less than 25 V. Thus, the electrons have less than 29.6013 eV, which corresponds to the second ionization energy of nitrogen, and thus cannot produce N^{2+}[133]. Test implantations and subsequent RBS investigations could not detect any N in the sample with this method, so it is assumed that the highest traces of N remain in the beam. Using NRA, lithium could be detected in the test sample, although no exact fluence determination was possible because the NRA setup was not calibrated using an external proton beam.

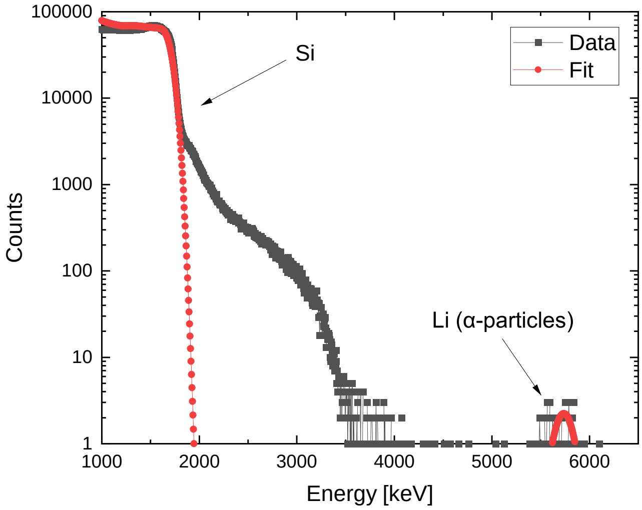

Figure 6.14: *NRA spectrum of a Si sample implanted with Li. The alpha particles from the nuclear reaction at 5700 keV can be clearly assigned to Li. The front peak is from backscattering events from the Si substrate.*

The corresponding NRA spectrum is shown in Fig 6.14. The corresponding α particles from the reaction appear at an energy above 5 MeV. Due to this high energy, the alpha spectrum is measured background-free and the counts can be uniquely assigned to Li.

6.4.2.1 New Filaments

One problem for implanting certain elements is the overlap of different isotopes with the same mass or mass to charge ratio (e.g. $^{40}\text{Ar}^{2+}$ and $^{20}\text{Ne}^{+}$). To avoid this other isotopes then the most present ones must be chosen for implantation. In the case of the given example $^{22}\text{Ne}^{+}$ can be used instead of $^{20}\text{Ne}^{+}$. For other elements like Nb only one stable isotope (^{93}Nb) exists, which makes is impossible to avoid overlap with $^{186}\text{W}^{2+}$. Since doubly-charged tungsten is always present due to the used filament, other possible filament materials were examined.
Due to the high melting point, filaments out of Ta and Mo were tested. Since those materials have different electrical properties, the length of the filaments were changed. For both a 0.5 mm thick wire were chosen, since this is also the diameter of the tungsten filament. Moreover, the same spring radius was used, to get a better placement inside the source. The number of windings, however, was adjusted is such a way, that the total electrical resistivity matches with the tungsten filament, in order to use similar settings to ignite a plasma.
With both materials a plasma could be ignited. In the case of the Mo filament the source was stable for around 1 hr before the filament broke. For the Ta the filament broke after 20 min. Since the new filaments were hand made, minor differences in the spring diameter and therefore different distances between the winding may have led to an uneven temperature distribution within the filament, which in turn may have resulted in the melting of the filaments at these locations.

6.5 Improved Deceleration unit and adapted sample holder

The new deceleration unit and corresponding test implantations are also presented in [22, 25] and was mainly designed by Manuel Auge. The main purpose of the new deceleration unit is to add another contact to the sample holder, which can be used to electrostatically deflect the ions from a part of the sample, thus forming an electrostatic mask.
The biggest change with respect to the normal sample holder concerns an additional contact on the deceleration unit, which can be used to connect an additional voltage to the sample holder. This voltage can be used to apply a potential path across the sample or to charge a

part of the sample significantly more positively to deflect incoming ions. The voltage can be applied by the new sample holder, which has all the features as the old ones, such as heating by filament and temperature measurement, either in contact with the sample or floating over the sample as a mask. A more detailed description with drawings of the sample holder and proof of concept implantations can be found in the PhD thesis of Manuel Auge [22]. In the current setup, a voltage of up to +600 V can be applied in respect to the implantation voltage. The use of a power supply is only suitable if the voltage is not in contact with the sample, because here, presumably the rectification of the voltage, leakage currents through the sample occur and the current measurement is distorted. In this case, batteries have proven to be a constant voltage source. Performed implantations in the context of this work are listed in chapters 9.4 and 9.5 as well as in [29].

6.6 New process control for the implantation

In order to replace the old process control for implantation and to be able to perform the implantations automatically, an Arduino-based system was built. The requirements for the control is that still a previously set fluence of the beam is automatically switched off when this fluence is reached. The control and counting of the pulses, which the current integrator sends back, is now done by an Arduino and not, as before, by a desktop PC. The advantage of this is that the Arduino only runs this one program and is therefore not disturbed by any background processes and therefore may not register pulses.

6.6.1 Hardware

The hardware consists of a Funduino Mega 2560, which is identical in construction to the Arduino Mega 2560. Furthermore, a keypad for entering the necessary parameters and an LCD monitor as a display.

The control of the power supply units is done via a fiber optic cable, because some of them are on 30 kV potential and therefore can not be controlled with an analog signal. For the switching of the beam deflector it is only necessary to switch a Transistor-Transistor-Logik (TTL) signal from 0 V to 5V. For the control of the current integrator, a certain bit sequence must be switched and a trigger signal must be set. The circuit diagram of the new control is shown in Figure 6.15. The connector describes the transition to the previously existing switch box in which the TTL signals are converted into light pulses. To count the pulses a capacitor with 1 nF is connected parallel to the input pin to intercept possible reflections and disturbances of the signal.

Funduino Mega 2560 The Funduino Mega is a mircocontroller board, which is identical in construction to the Arduino Mega 2560. It has 54 digital input/output pins which can be switched between 0 V and 5 V. It also has 16 analog inputs, several ground pins and power supplies of 3.3 V and 5 V. It can be controlled via USB and the Arduino IDE software can be used for programming. The programming language very close to C++. As a stand alone system it can be powered by a 9 V 1 A power supply.

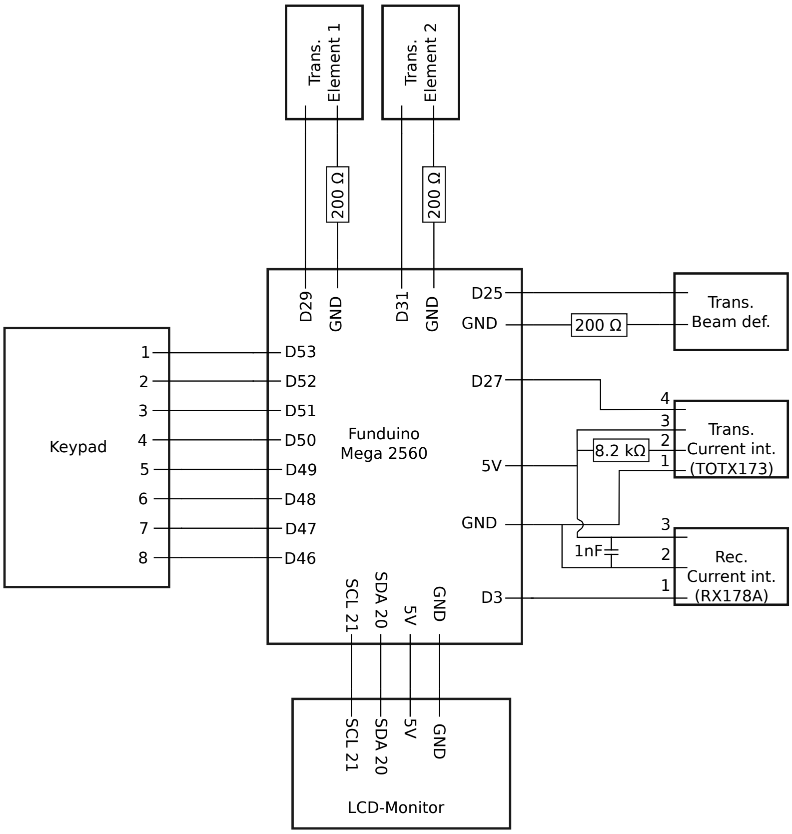

Figure 6.15: *Circuit diagram of the new process control. The signals gets converted to light pulses, which then are transmitted to the beam-deflect control unit, the current integrator or the magnet control unit.*

6.6.2 Program

In the following, the program will be described briefly. After starting the Funduino, the beam deflector is switched on to avoid a too early irradiation of the sample. Afterwards the fluence can be set in 10^{12} at/cm^2 steps and the current regime of the current integrator must be selected. The total charge needed and the number of pulses sent by the current integrator to reach the charge is calculated. After confirmation the Beam Deflector is switched off, the internal time is stored and the pulses are counted. After reaching the required charge, the beam deflector is switched on again automatically and the time difference of the implantation is determined and output. The values are entered via the connected keypad and the calculated values, the implantation progress and the total implantation time are displayed on the LCD monitor. For direct communication of the Arduino with the current integrator the outputs of the Funduino are connected directly to optocouplers, which send the light pulses to the current integrator. In addition, the counting signal is also sent directly to the Funduino and read out. With this setup, the old electronic is no more necessary, and the system is therefore less error-prone. There was the possibility that more interfering pulses were caught and additional counting pulses were generated. In addition, it could happen that a spark in the accelerator has reset the current integrator and thus the current range was lost.

Code The complete Arduino Code can be found in the appendix 10. A brief explanation follows here. First the *Wire* [134], the *LiquidCrystal_I2C* [135] and the *Keypad* library must be loaded, to connect to the LCD screen and the Keypad. Afterwards the Keypad is implemented by defining the rows and columns. After defining the needed variables, the void setup, which will be executed once the Arduino is turn on, is implemented. Here, the used Pins get defined and the LCD screen gets initiated. Furthermore, storage are reserved for the Input of variables likes the fluence and the current regime. At the end the beam deflector is turned on to avoid unintentional irradiation of the sample.

The main loop program is defined in void loop. First, all variables are set to 0 to reset the program from previous implantations. After this, the query of the desired fluence starts which is entered via the keypad in $10^{12}\,\mathrm{at/cm^2}$. For this the program is paused until an input is made. The numbers of the keypad are stored in your array and after confirmation of the fluence is converted into an Int value. The same procedure is repeated for the input of the current regime in nA. After confirmation the necessary pins are switched to 5 V and then the trigger is set to switch the current integrator to the correct regime. Afterwards the program pauses until a new confirmation via the keypad. If this is done, the current system time is read out and the beam deflector is switched to start the implantation. The program calculates the required counts of the integrator from the entered fluence and the current range. Then, the program runs through a loop in which the current counts are read out until the required number is reached. Furthermore, trigger signals are repeatedly sent to the integrator in the loop, since the current range can be switched over by sparks from the accelerator. By constantly resetting the current range at the integrator, such an error is corrected within a few milliseconds, thus ensuring correct current measurement. The counting function is done by an interrupt circuit, because the Arduino has only one thread, no two functions can run at the same time. The interrupt is triggered when a signal arrives at pin 3 and causes the void count function to be called, which increments the current counts by one. After reaching the desired counts, the beam deflector is switched to end the implantation and the system time is read out again to determine the total time of the implantation from the values of the times and then to show it on the display. After pressing a key again, the program switches back to standby and the next implantation can be set. To set the current regime, digital signal consisting of a 9 pulse signal, must be send to the current integrator. The length of the individual pulses subsequently determines the regime set. A distinction is made between a pulse length of 0.3 ms and 0.15 ms and a pause between the pulses of 0.35 ms and 0.5 ms. The total duration of the signal is always the same. After starting the implantation, the signal is sent to the current integrator every 6 ms to compensate for any reset due to sparks.

Film growth In addition to the implantation of a single ion type, there is also the possibility of film growth of different elements, such as BN films. For this purpose, the respective fluence of the individual elements is also specified. Since film growth involves significantly higher fluence (3×10^{15} at/cm^2 corresponds roughly to one atomic layer), the unit 10^{15} at/cm^2 is used here. In order to switch between the different masses during irradiation, up to four masses can be preset on the control unit of the magnet, whereas in the current version, only two masses can be set using the program. A light pulse can then be used to switch between these masses. In order to grow a homogeneous film, the mass is changed every 1×10^{15} at/cm^2, therefore only a fraction of an atomic layer is grown with the same element and a good intermixing is guaranteed. After reaching the set total fluence, the beam is automatically switched off again.

7 IMINTDYN

In the following chapter a description of the program for simulating ion implantations named IMINTDYN [26, 123] is provided. Most of the new features and how they are calculated within the program are published in [26]. Here only a short description is given, about the features, which are of special importance for the simulation of implantations in 2D materials. A more detailed description can be found in [26].

The program is based on SDTrimSP [27] and was written by Hans Hofsäss, with numerous ideas and suggestions for program features, like the use and handling of vacancies (sec. 7.3) or the fixed layer density feature (sec. 7.4) arising from collaborative discussions. It is a binary collision approximation (BCA) Monte-Carlo program, which is able to dynamically adjust the composition during the simulation. Thus, scattering of ions at already implanted atoms can be taken into account. In the following, the features of the program are explained in detail and their physical justification is given. Most of these features are also described in [26]. Since IMINTDYN only uses the BCA approach in its simulations, and only assumes an amorphous target structure, the general implantation behavior can be simulated and a good estimate of the penetration depth, energy loss and collision cascade can be calculated, but no accurate prediction of the type of damage to the sample can be obtained. For example, it is not possible to say if and which lattice site will be occupied by a foreign atom. This is due to the fact that no exact diffusion behavior and no chemical processes can be simulated. However, since the implantation simulation is only a momentary recording and the collision cascade ends after a few femtoseconds (speed of 20 eV C corresponds to 0.18 $^{\text{Å}}/_{fs}$), it can be assumed that chemical processes do not play a major role during the implantation and the collision cascade.

Different simulations of implantations in graphene, with and without substrate, $MoSe_2$ and MoS_2 were performed to get an understanding of implantations in 2D materials can be found in ch. 8.

7.1 Binary collision approximation

The binary collision approximation is a concept for the numerical calculation of ion-solid interactions in simulation programs. Here, only single collisions between the ion and a target atom are considered. Between the collisions, the ions continue to fly on straight-line trajectories. The mean free path λ is calculated by $\lambda = N^{-1/3}$ and therefore is determined by the target density. In this way a higher density leads to a shorter free path length between two collisions. At each collision an energy loss take place and the ion decelerates, until a critical energy is reached and the simulation of this ion stops. This energy is the so-called cutoff energy.
For the calculation of the collision, an important factor is the impact parameter (cf. ch. 3.1). It indicates the minimum distance between the two particles involved in the collision. Thus, it has a large influence on the collision kinematics and therefore on the energy transfer between the particles. For the collisions, cylinders with volume V are chosen with $V = N^{-1} = \lambda \pi b_{max}^2$ [26], where N describes the atom density of the target, λ the mean free path length and πb_{max}^2 the cross section area. The choice of $V = N^{-1}$ ensures that there is only one target atom in the cylinder.

The collision is always assumed to be elastic, which can be justified by the fact that the target atom is bound in the potential minimum at the moment of the collision and thus no repulsion force is present. If not enough energy is transferred to a target atom to overcome its binding energy during a collision, i.e. no recoil is generated, the momentum which would have to be transferred to the individual atom is transferred to the entire target in the context of momentum conservation.

A Monte Carlo simulation is used to simulate the collisions of the ions with the nuclei of the sample. To accomplish this, each atom of the sample is first divided into a unit cell in which the interactions are calculated. Four random numbers R_{1-4} are used for this calculation. One (R_1) to determine the mass of the atom in the unit cell, taking into account the composition of the sample. A second, which reflects the impact parameter, where $b = b_{max} \cdot \sqrt{R_2}$. The third, which will have influence of the free flight distance L of the ion, can be calculated via $L = {}^{R_3}/_{n \pi b_{max}}$, where n indicates the atomic density. And a last one, which determines the azimuth angle $\phi = R_4 \cdot 2\pi$ of the further flight path of the ion [70].
Examples of BCA monte carlo programs on ion-solid interaction are SRIM [70], Tridyn[136], SDTrimSP [27] and IMINTDYN [26, 123]. SRIM in particular is widely used because of its ease of use graphical user interface, however, it is not suitable for the calculation of ultra-low energy ion irradiations due to internal assumptions and estimations and therefore, do

not properly predict the implantations profiles. The physics used in BCA simulations for the ion-solid interaction is described in much detail in the book from Eckstein [60].
The target in the simulations is always assumed to be armoph independent of the actual target structure. This is justified by the fact that in the course of the simulation, due to the damage caused by the irradiation, a crystal structure also approaches an amorphous structure. In any case, the calculation without crystal structure offers the advantage of saving a significant amount of computing capacity.

7.2 Simultaneous Weak collisions

Especially with small impact parameters, it can happen that there are neighboring atoms in the target with which a larger impact parameter exists. These would be neglected in normal BCA simulations. At high ion energies, this can also be neglected, since the energy loss occurs mainly through electronic energy loss (see ch. 3) and not through the collisions and thus the nuclear energy loss. However, in simulations for less than 10 keV ion energy, the effect of the weak collisions is significant, since the nuclear energy loss becomes more important. If neglected, it can lead to an energy transfer per collision which is too small, and thus to a significant overestimation of the penetration depth. To take this into account, n cylinders are placed around the central cylinder, where n is the number of weak collisions considered, with one atom per cylinder. In Fig. 7.1 the representation of the cylinders with $n = 2$ is given.

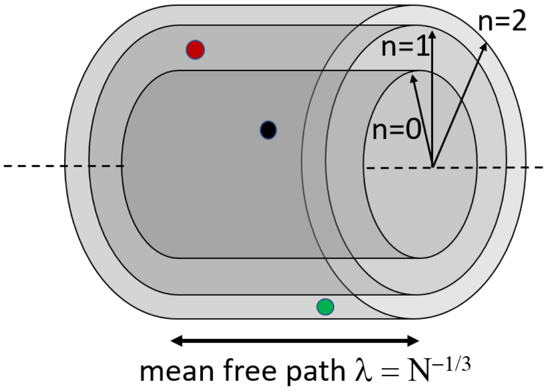

Figure 7.1: *Illustrated here is the concept of simultaneous weak collisions, where coaxial ring cylinder volumes hold exact one target atom each at random positions (depicted in black, red, and green). The impact parameter, indicating the distance between the incoming projectile and the target atom along the dashed axis, is randomly selected within the confines of the inner and outer cylinder radius limits. The Figure was made by Hans Hofsäss and published in [26] under the CC-BY 4.0 licence and slightly adapted.*

The maximum impact parameter P_{max} is then calculated by

$$b_{max}(n) = \frac{1}{\sqrt{\pi}} N^{-1/3} \sqrt{n}. \tag{7.1}$$

If the initial scattering is a vacancy atom, further vacancies are neglected for the weak collisions. For this, first the density of the target is adjusted accordingly, as if there were no vacancies in the target and then again a target atom is randomly selected for the 1st and 2nd cylinder. The atom density must be adjusted in this case, so that the impact parameter can be calculated correctly, otherwise it would be artificially increased. For $n > 0$ one get $n + 1$ collisions per BCA step. For IMINTDYN the default value of $n = 2$ is chosen, but can be adjusted if necessary. The choice of $n = 2$ was made here, as the influence of weak collisions at larger distances to the original collision center consistently diminishes. However, opting for a small value of n allows for the optimization of computational time. The exact calculation and a detailed description of the weak collisions in IMINTDYN can also be found in [26].

7.3 Vacancies

A new feature in IMINTDYN is the use of vacancies as target atoms. The vacancies appear as target atoms and have the mass $M = 0$ and the atomic number $Z = 0$ [26]. If a projectile hits a vacancy, the free flight path is doubled by taking into account weak collisions with more distant massive target atoms. During a dynamic simulation, vacancies can be generated and annihilated. Thus, a vacancy can be created when a collision take place and the target atom in question receives more than the displacement energy. In turn, a vacancy can be destroyed when a projectile stops in the immediate vicinity of a vacancy. This innovation offers an immense advantage over other BCA programs such as SRIM or SDTrimSP. There, vacancies are incremented as a simple counter without changing the target composition or density. However, the vacancies can cause the range of the ions to increase significantly at low energies (<10 keV). For the simulations of 2D materials the vacancy can also be used as a filler atom or spacer, to simulate a crystal like target (see. 8.1.1). Since there is not yet a theory for the vacancy formation probability under ion irradiation for simulations, different methods can be applied. The formula for the calculation of the vacancy formation probabilty p_{vac}, which has been applied here is

$$p_{vac} = q_{vac} \cdot (1 - c_{vac})^2, \tag{7.2}$$

where q_{vac} is the general formation probability, which can be specified in the input file, and c_{vac} is the local vacancy concentration. Thus, the probability of creating another vacancy decreases if there are already many vacancies in the layer. This formula gives good predictions in experiments [26] (see. 7.9). For q_{vac} in this work the value 1 was chosen, so that in principle each impact with enough energy is transferred produces a vacancy. A detailed description of the vacancy handling and calculation can be found in [26].

7.4 Fixed Layer Density

Another feature is the fixed layer density. In the case of implantations with gas atoms or ions with a strongly different atom density compared to the target, it can happen that the density of the individual layers is calculated incorrectly in the dynamic simulations. Since in dynamic simulations the target is constantly updated during the simulation, the density is also recalculated. If atoms with a significantly lower density are implanted, the density calculated as the average value of all the atoms present in the layer may be significantly too low and the program may decide to split a layer into two or to merge several layers together. This can lead to the layer structure being mixed up, especially in the case of 2D materials. To prevent this, the atom density of the individual layers is kept constant and the atom density of the implanted ions is adjusted accordingly. The reason for this is that even gas atoms in a graphene layer are not incorporated with their gas density but either replace a carbon atom or occupy an intermediate lattice site and thus lead to lattice distortions but do not radically change the atom density [26].

7.5 Displacement Energy

An important point for the calculation of the collision cascade and implantation profiles is the so-called displacement energy. This energy must be overcome to release an atom from its lattice place to act as a recoil. For IMINTDYN the displacement energy is set equal to the sublimation energy. A justification for the choice in the case of graphene is given in chapter 4.

7.6 Bulk Binding Model

Also new is the bulk binding energy model. In other BCA simulations, the surface binding energy model is used. This was designed to better simulate sputtering processes. First, a surface binding energy is assumed, which is added to the ion energy when entering the target. If an atom leaves the target in the course of the collision cascade, i.e. is sputtered, this energy is subtracted again and thus a different scattering behavior is achieved when the atom leaves the surface. In contrast, in the bulk binding energy model no surface potential is assumed and the ion gets no energy when entering the target. Instead, the sublimation energy is subtracted from the recoil when it is generated. This describes the sputtering process as well as the surface binding model but has a more physical justification [123].

7.7 Cutoff Energy

Another important point to calculate the penetration depth correctly, is the right choice of the cutoff energy. This specifies when an ion is at rest and thus the collision cascade is stopped. The cutoff energy used is expressed as $1/3$ of the sublimation energy or 1 eV for gases [26]. Too low cutoff energies of 0.1 eV as in TRIDYN [136] provide significantly overestimated penetration depths [26]. On the other hand, if the cut off energy is set too high, a significant portion of the collision cascade may not be captured and thus the penetration depth, recoil production and sputter yield may be miscalculated.

7.8 Electronic stopping

Although in the implantations considered in this work the ion energy is very low and electronic stopping is of little importance. The choice of the potential for electronic energy loss is an much more important parameter for the simulations of implantations into 2D materials. IMINTDYN offers, like SDTrimSP, the possibility to choose between different potentials, like Lindhard-Sharf or Ziegler-Biersack-Littmark. IMINTDYN can also use the SRIM stopping powers for all projectile target combinations [26]. The special feature of the SRIM data is that they are not only based on theoretical models, such as the Lindhard-Scharf or the ZBL model, but represent an interpolation of experimental data. This ensures a high accuracy, especially at medium to high energies, since numerous measurement data are available in this energy range. At low ion energies, unfortunately, there is little to no experimental data. However, this does not make the fit any less useful than the theoretical models, since it is not known exactly which model is most accurate at the low energies.

7.9 Testing IMINTDYN with W implantation

To verify the correctness of the new features of IMINTDYN and the reasonable usage of vacancies as a new target atom instead of adapting the atomic density, W implantations were performed and then examined using High Resolution RBS. The experimental data and analysis, together with an interpretation of the results can also be found in [26]. For this study, the required implantations in ta-C were performed by the author of this thesis. The measurements were done by Felix Junge and Hans Hofsäss and the simulations and the analysis of the experimental data were carried out by Hans Hofsäss.

7.9.1 Experiment

For experimental verification, a ta-C layer on a Si substrate was implanted with W. Tungsten was chosen because of its a high mass and because it reacts with the carbon to form tungsten carbide, thus forming a stable composition inside the target which prevents diffusion of the implanted W. Other elements such as Se or Ag tend to diffuse from the carbon layer to the surface and subsequently leave the sample. Tungsten atoms react with the carbon at the point where they come to rest and are therefore ideal for testing depth analyses. Two implantations were performed sequentially. First, W was implanted with 10 keV and a fluence of 1×10^{15} at/cm². Then, W with an energy of 20 eV and the same fluence was implanted to obtain a surface signal during HR-RBS measurement. In addition, a W layer prepared by sputter deposition was examined to also determine the surface area in the energy spectrum of the backscattered He atoms. For HR-RBS analysis, He$^+$ ions with an energy of 446 keV and a beam spot of 1 mm diameter were used. The electrostatic analyzer has an inner radius of 300 mm and 6 mm plate spacing and comprises a 90° sector angle [107]. The energy resolution of the analyzer system is $\Delta E/E = 0.5\%$. The scattering angle which was measured is 127°. The pressure in the analyzer was 2×10^{-7} mbar, so the energy loss on the way to the detector is negligible (cf. ch. 5.2.2). A description of the measurement setup is also given in [26]. The simulations with IMINTDYN were performed accordingly. In addition, the expected backscatter spectrum was simulated with IMINTDYN.

7.9.2 Results and discussion

Figure 7.2 displays the results of the HR-RBS measurement, which are plotted alongside simulations. The simulations in Fig. 7.2a correspond to various parameters available in programs such as SRIM or TRIDYN. Parameters that were investigated include a density change from ta-C to a-C (graphitic) and cutoff energy EC. In this case, the chosen cutoff energy of $EC = 0.1$ eV corresponds to the default value of TRIDYN. Additionally, a simulation was conducted that corresponds to SRIM.

At first it is noticeable, that although the same fluence was used for both W implantations, that the measured fluence in the deeper W layer (corresponding to the 10 keV), determined via the integral of the measured signal, is about 25 % lower. This is due to the increased production of secondary electrons leaving the sample, which distorts the current measurement used to determine the fluence during implantation. With the 20 eV implantation on the one hand significantly less secondary electrons are produced and on the other hand they have a significantly lower energy, which is why they are directed back onto the sample by the negative focusing lens for the target and cannot escape. The simulations show that the use of dynamically produced vacancies significantly increases the range of the ions compared to a reduction of the density of the ta-C layer. At a dynamic steady state concentration of 14 % vacancies, the HR-RBS results can be simulated very well (Fig. 7.2b), while a reduction of the density of ta-C to graphite does not agree with the measurements, even the overall density of the ta-C and vacancies is higher then the density of graphite. Therefore, it can be concluded, that the new feature of vacancies as target atoms, which can be generated and annihilated is an important advantage, when it comes to the simulation of depth profiles. Another important point is the use of simultaneous weak collisions. If these are not taken into account, the ion ranges also increase significantly and cannot reproduce the results of the measurements. The exact measurement results and their detailed interpretation can be also found in [26].

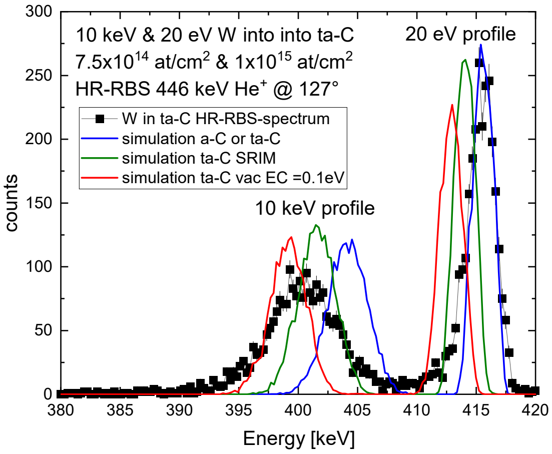

(a) **(b)**

Figure 7.2: *(a) Comparison of the experimental W implantation HR-RBS spectrum to simulations under various conditions.(b) Experimental W implantation HR-RBS spectrum and IMINTDYN simulation of W implantation into ta-C with the use of vacancy generation. These graphs are also published in [26] and were slightly adapted.*

8 Implantation Simulations

The IMINTDYN code enables useful simulations of implantations into 2D materials to be made. We discuss both graphene and TMDs to investigate the best implantation energy and substrate effects. For all implantation simulations into 2D materials, the Kr-C potential [73], which has been proven to be the most accurate at low energies and 2D materials and SRIM stopping power data were used.

8.1 Graphene

8.1.1 Graphene structure

The graphene layer with layer spacing of 3.35 Å is simulated as a 1.1 Å thick carbon layer, followed by two layers of vacancies each 1.1 Å thick. The deeper layers, and thus the substrate, consist of SiO_2. The sublimation energy of 7.428 eV is used as the displacement energy of the carbon. This also corresponds to the vacancy formation energy of graphene [95]. To take the lattice structure into account, even if IMINTDYN assumes the layers as amorphous, the graphene layer was adjusted slightly to simulate the hexagonal arrangement of the atoms. Because of the lattice structure there is the possibility that an ion flies through the middle of the carbon ring without colliding with an atom. Therefore, the first layer in the simulation consists of 2/3 C-atoms and 1/3 vacancies since two C-atoms and one empty center are to be assigned to one carbon ring. The density of the layer, with a layer spacing of 3.35 Å, was then increased to $0.4965\,\mathrm{at}/\text{Å}^3$, so that the atomic density of carbon atoms again corresponds to graphene. In the interpretation of the results, however, it must be taken into account that the first layer consists of only 66.7 % carbon followed by two layers consisting solely of vacancies. It is worth emphasizing that when a high fluence is implanted, foreign atoms can annihilate vacancies within the graphene layer, even if those vacancies were not initially formed through recoil production. Thus, more vacancies are annihilated than created. This leads to an increase of the actual atomic density in the simulation which could be significantly higher than the real atomic density. However, the fluences used for the implantation simulations into graphene in this work are low enough that this effect is not relevant and can be neglected. In addition, not only collisions with the atoms that can hit directly but also collisions with nearest neighbor and next nearest neighbor atoms (weak collisions) were taken into account. The structure of the simulated graphene is also described, just like the He implantations, in [29].

For the multilayer graphene, the same structure as for the single-layer graphene was assumed. Thus, a graphene layer consists of a carbon layer with 33.3% vacancies, followed by two complete vacancy layers. The atomic densities were adjusted to achieve a total carbon density of $3.85\,{}^{at}/_{cm^2}$. Figure 8.1 shows a schematic diagram of the graphene structure with the filler vacancies. In addition, the side view is shown for a better illustration of the two vacancy layers. A depth profile used as start condition for the simulations can be found in Fig. 9.7a in chapter 9.5.

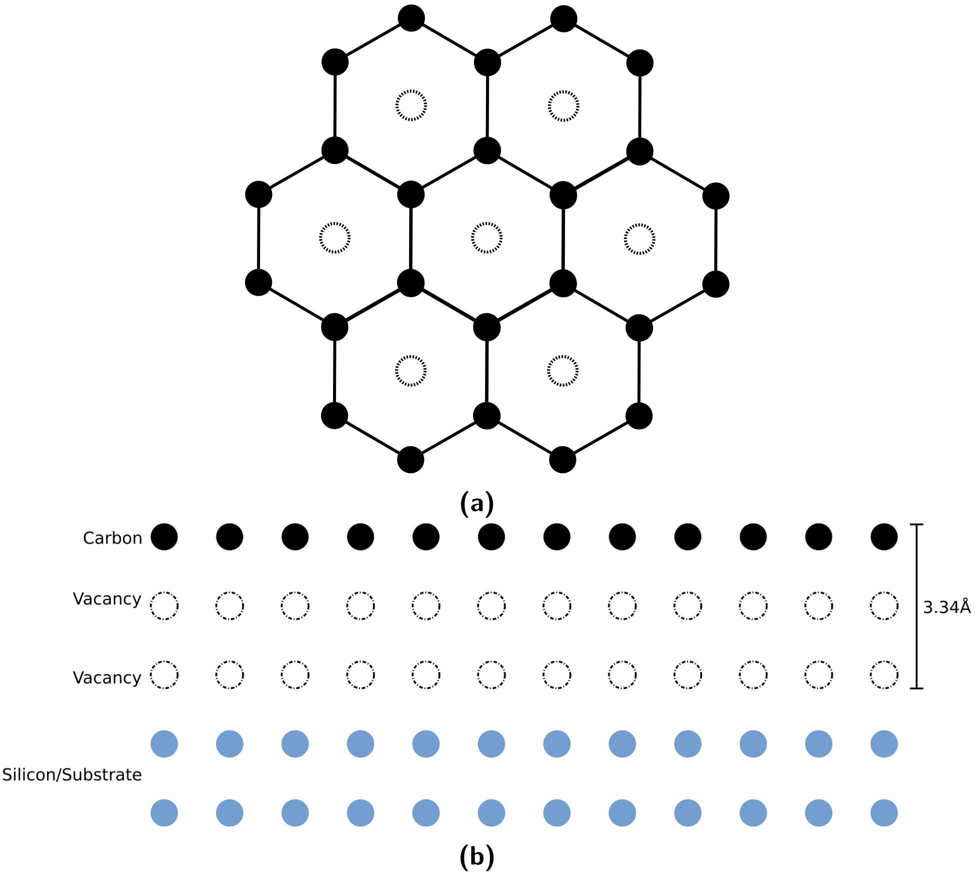

(a)

(b)

Figure 8.1: *(a) Schematic top view of the graphene layer as used for the simulation, the open circles symbolize filler vacancies. (b) Side view of the graphene layer as used for the simulation, with one carbon layer and two vacancy layers.*

8.1.2 Simulation of optimal implantation energy

An important parameter for ion implantation is the energy of the ions. This is especially the case for 2D materials, since deviations of only a few 10 eV can cause the ions to fly through the layer and cause a lot of damage or actually come to rest in the uppermost atomic layers. In order to find out which is the best energy, IMINTDYN simulations of B, N, Fe and Gd in graphene on different substrates were performed. B and N were chosen since these elements are can be used for p and n doping. Fe and Gd were chosen to study examples at different atomic masses. The substrates studied were Cu, SiO_2 and free-standing graphene. In addition, bi-layer graphene on SiO_2 and freestanding was considered. To find out the energy at which the highest concentration of impurity atoms is present in the graphene layer, the simulations were performed in 1 eV steps from 5-100 eV. Lower energies were not considered further, since the ADONIS implanter cannot reliably provide such low energies.

In Figure 8.2 the atomic concentrations of the implanted atoms in the top graphene layer on different substrates are plotted against the implantation energy.

It is noticeable that two maxima occur for B and N, with the first maximum at the energy at which the first C can be dissolved from the lattice (sublimation energy of C) and occurs as a recoil. The second maximum at higher energy occurs due to multiple scattering, both in the graphene layer and by backscattering from the substrate. The comparison between B, N and Fe shows that the maximum concentration in the graphene layer increases with higher atomic mass. However, this trend does not continue, because firstly there is no maximum in Gd at energy higher than 5 eV and secondly the concentration in the graphene is lower overall. To find out what happens to the Gd compared to the Fe, the simulated implantation profiles of Gd and Fe at an implantation energy of 10 eV and an implanted fluence of 5×10^{14} at/cm² are shown in Fig.8.3.

The first thing that stands out is that no C was removed from the lattice during the Gd implantation with 10 eV and no C recoils were driven deeper into the material. This is due to the fact that because of the large difference in mass, the maximum energy transferred from Gd to C is not sufficient to overcome the sublimation energy. If the Gd then has enough energy to remove carbon, the energy after the collision is still so great that the Gd is transmitted further into the substrate or, in the case of free-standing graphene, into vacuum. It can also be seen that in the case of iron, many atoms fly through the graphene structure and end up in the first substrate layers. This is due to the hollow structure simulated by the filler vacancies. In addition, Gd is so heavy that only forward scattering can take place, even on the substrate,

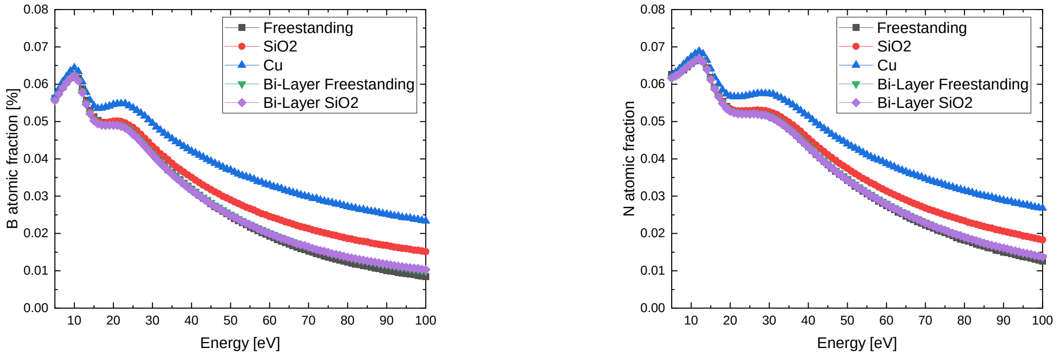

(a) *B concentration in the first graphene layer.* **(b)** *N concentration in the first graphene layer.*

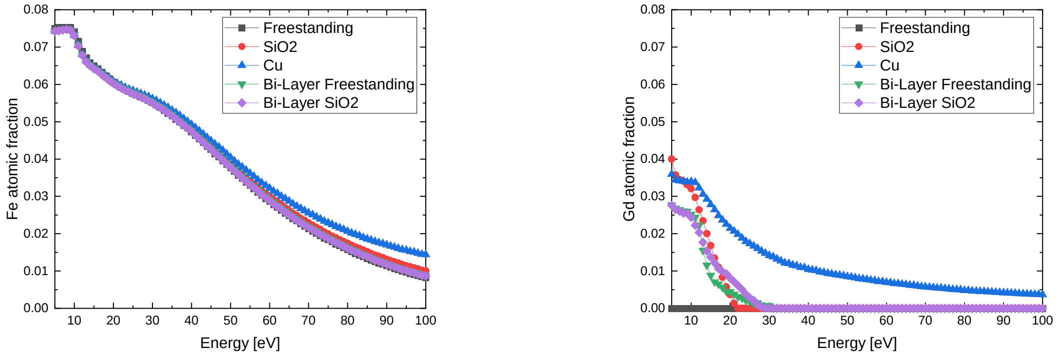

(c) *Fe concentration in the first graphene layer.* **(d)** *Gd concentration in the first graphene layer.*

Figure 8.2: *Concentrations of impurity atoms (a) B, (b) N, (c) Fe, and (d) Gd in the top graphene layer on different substrates after implantation with different energies and fluences of* 5×10^{14} $^{at}/_{cm^2}$.

so at least two collisions must take place for the Gd to be scattered back into the graphene. Afterwards, the energy is so low that the highest vacancies are destroyed but no proper incorporation into the graphene takes place. The fact that atoms also come to rest in the vacancy layers is due to the weak collisions. One would expect that when an atom hits a vacancy, it would just keep flying straight and not lose energy. However, due to the simulation of the weak collisions, scattering with distant atoms takes place, which causes a small energy loss.

To find the energy at which most of the atoms end up in the C layer, a bi-Gaussian was fitted to the peaks. The values for the implantation energy, at which most of the impurity atoms come to rest in the graphene layer, are listed in Tab. 8.1.

It can be seen that the energy is independent of the substrate on which the graphene is

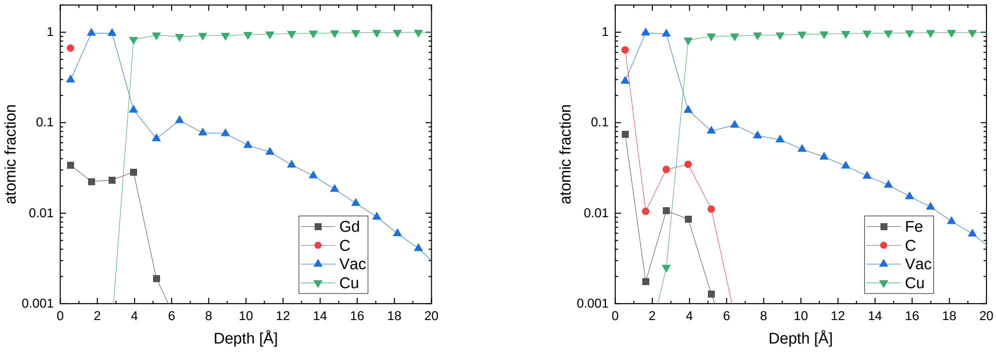

(a) **(b)**

Figure 8.3: *(a) Simulated implantation profile of graphen on Cu after a 10e eV* $5 \times 10^{14}\,{}^{at}/_{cm^2}$ *Gd implantation. (b) Simulated implantation profile of graphen on Cu after a 10e eV* $5 \times 10^{14}\,{}^{at}/_{cm^2}$ *Fe implantation.*

Table 8.1: *Values for the implantation energy at which most of the implantation atoms are incorporated in the graphene layer on different substrates. The values are in eV.*

	B	N	Fe
Freestanding	10.3(2)	12.9(3)	8.3(3)
SiO_2	10.2(2)	12.7(3)	8.3(3)
Cu	10.0(2)	12.4(1)	8.3(3)
Bi-layer freestanding	10.2(2)	12.6(3)	8.3(3)
Bi-layer on SiO_2	10.2(2)	12.7(3)	8.2(3)

located. However, the substrate has an influence on the number of atoms that end up in the layer, which is particularly significant at higher implantation energies. The reason for this is the backscattering from the substrate. At lower energies, this is hardly significant, since many ions lack the energy to reach the substrate or receive enough energy to get back into the graphene layer after backscattering at the substrate. At higher energies, however, the backscattered ions have enough energy to come to rest in the graphene. It is also clear that the heavier the atoms in the substrate, the more ions are repelled. This is mainly due to the Rutherford cross section, which is also increased for heavier (higher atomic number Z) collision partners (see eq. 5.8). This explains the slower decay of the introduced implantation atoms in a Cu substrate, compared to the SiO_2 substrate.

An interesting finding is that the most sufficient energy for implantations is about 8-13 eV. This energy is significantly lower than the 15-40 eV used for implantations (see ch. 9). This is because, the maximum possible implantation energy is always fixed during implantation and but ions with lower energy will be also present in the beam (see section 6.4.1.1). In addition, the simulation does not distinguish between substitutionally implanted atoms and atoms simply located in the layer, since IMINTDYN assumes the sample to be amorphous and thus the type of defect created cannot be determined. Therefore, it is possible that filler vacancies are simply filled with implanted atoms without removing a carbon atom. These are then barely bound and could subsequently diffuse out of the sample in a mobile manner. The same applies to adatoms, which are assigned to the top layer in the simulation but are not bound in the graphene. Thus, although the penetration depth of the ions can be determined very well from the simulations, it is not possible to say whether these ions really remain at this location after implantation.

8.1.3 Substrate recoils

Another effect that can be studied is the damage to graphene caused by the introduction of recoils from the substrate. For this purpose, the same simulations were used and the proportion of substrate atoms in the graphene layer was analyzed. In Fig. 8.4, the concentrations of the substrate atoms in the uppermost graphene layer are plotted.

It can be seen that the concentration of substrate atoms in the graphene layer increases with increasing implantation energy. This is because, on the one hand, more ions can penetrate into the substrate and start the collisions cascade there and, on the other hand, more energy can be transferred to the substrate atoms, which can then form recoils and finally be sputtered into the graphene. The concentration decreases with increasing ion mass. Presumably, this is due to momentum, which is forward in the simulation and larger for heavy ions. Thus, scattering angles in the forward direction are preferred for heavier ions. It can be seen that in all investigated cases the Cu concentration from 40 eV implantation energy onwards is higher than the summed concentration of Si and O from the SiO_2. This is mainly due to the higher mass of the Cu and therefore increased scattering cross section. From the substrate behind the bi-layer graphene, a slight increase can be observed only at high energies and at B implantation. This is hardly surprising, since the concentrations in the uppermost graphene layer were investigated here, and thus the substrate atoms must first overcome a carbon layer again. It can also be deduced from this that implantation should be carried out with as little energy as possible, the concentration of substrate atoms in the graphene can already exceed 1 % at 50 eV and thus a non-negligible proportion of substrate atoms can be incorporated into the graphene. Above 100 eV the concentration of substrate atoms can even exceed the number of implanted atoms. Again, it must be emphasized that these atoms are not necessarily bound in the graphene but can also occupy filler vacancies without significantly damaging the

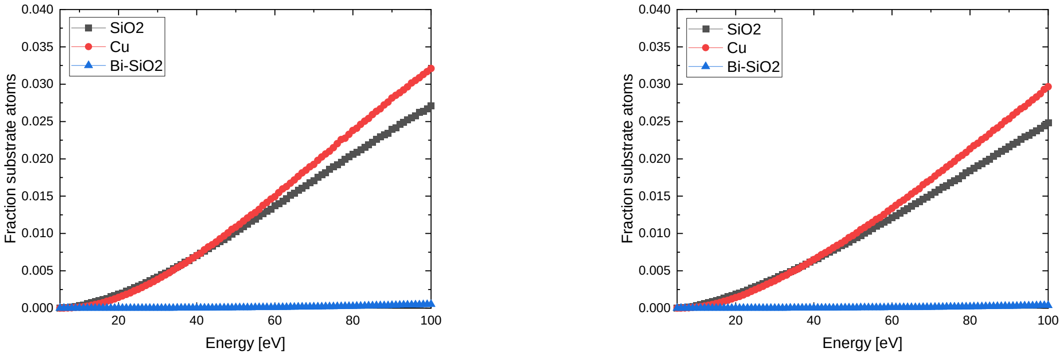

(a) *After B implantation.*

(b) *After N implantation.*

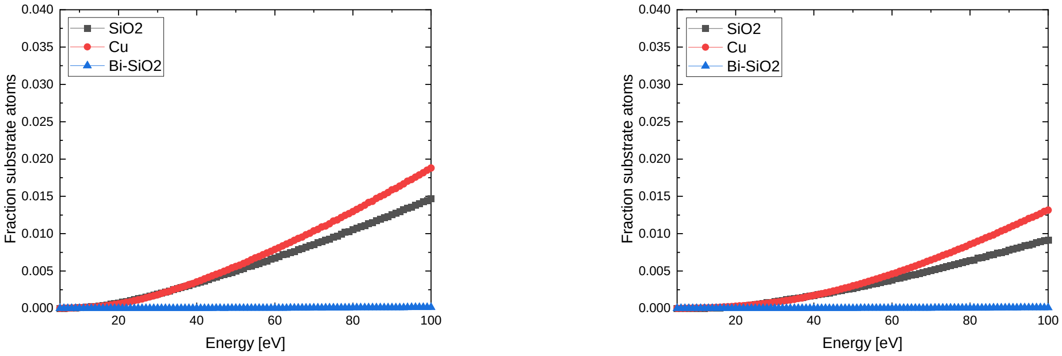

(c) *After Fe implantation.*

(d) *After Gd implantation.*

Figure 8.4: *Concentrations of substrate atoms in the top graphene layer on different substrates after (a) B, (b) N, (c) Fe, and (d) Gd implantation with different energies and a constant fluence of* 5×10^{14} *at/cm²*.

graphene. To keep the concentration of substrate atoms as low as possible, one could consider using bi-layer graphene and transferring the top layer after implantation. This way, one would have at most C atoms sputtered back into the graphene, which could heal defects (vacancies, holes, etc.) created in an annealing step. The top layer would then have to be lifted off and transferred again, which would be a much more complex procedure than using the implanted sample directly after implantation.

8.1.4 Water on Graphene

In order to investigate the effect of a water film on the graphene layer, simulations were carried out, in which the energies of 5-100 eV were simulated in each case. Since the water on the sample is in the form of ice in a vacuum, the density of ice was assumed. Different thicknesses from 1.1 Å to 22 Å were simulated with a B fluence of 1×10^{14} at/cm².

In Figure 8.5a, the boron concentrations in the graphene layer against the used implantation energy is presented for different ice layer thicknesses. It can be seen that again two maxima of boron in the first layer occur at different energies. Furthermore, these maxima shift to values of higher energy, which makes sense insofar as the boron ions are slowed down in the ice film. The energies of the two maxima were plotted against the ice thickness and fitted linearly to obtain a correlation between the two values (see. Fig 8.6). Here it can be seen that for each Å ice about 1 eV more must be applied for the first and around 2 eV for the second maximum. In addition, it can be seen with the higher ice thicknesses that the required energy decreases again with increasing fluence during the simulation, which is due to the sputtering of the ice film. Although this effect is rather small in the typical fluences used for doping 2D materials and can be largely neglected. Furthermore, the ice film has great influence on the concentration of boron in the graphene layer. Thus, the overall maximum concentration without water film is about 1.3% and drops significantly at 22 Å to 0.3%. It can be clearly seen that the first peak increasingly disappears, which indicates that single scattering events of boron in graphene hardly occur and the boron ends up in the graphene through multiple scattering. Another important point is the formation of recoils. When boron hits the water molecules, both hydrogen and oxygen recoils are formed, which are then also incorporated into the graphene. Figure 8.5b shows the concentrations of H and O from the ice together with the B in the graphene at different B implantation energies for a fluence of 1×10^{14} at/cm². Here it can be seen that a significant fraction of oxygen and hydrogen is introduced into the graphene and in some cases exceeds the boron concentration, making the oxygen impurity the main dopant element.

To get an even better impression of the distribution of the B and Ice layer atoms, Fig.8.7 shows the depth profile after a 40 eV 5×10^{14} at/cm² B implantation in a sample with 11 Å ice on the surface. Even if the 40 eV corresponds approximately to the energy, the maximum concentration in the graphene, one recognizes that most B atoms are directly in front of the graphene in the water film. Furthermore, there is again an increase of the B concentration in the substrate, which is related to the fact that due to the filler vacancies many B atoms fly through the graphene and are only effectively stopped in the substrate. The same is valid for the H and O recoils from the water film. In addition, it can be concluded that at 40 eV enough energy is also transferred to the C atoms so that C recoils are also implanted into the substrate. A small fraction of the C atoms is also sputtered back into the water film.

These results show, that the usage of a capping layer on top of the graphene leads to a significant amount of recoil atoms in the graphene and is therefore to avoid. If a physical

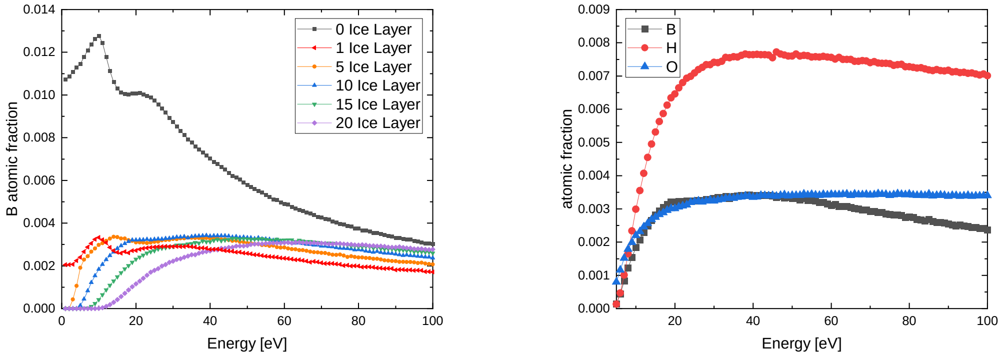

(a) **(b)**

Figure 8.5: *(a) Boron atomic fraction vs. the ion energy in the graphene layer, when it is covered with water green and implanted with* $1 \times 10^{14}\,\mathrm{at/cm^2}$. *(b) Atomic fraction of foreign atoms in the graphene layer after the implantation of* $1 \times 10^{14}\,\mathrm{at/cm^2}$ *B and a ice thickness of 1.1 nm.*

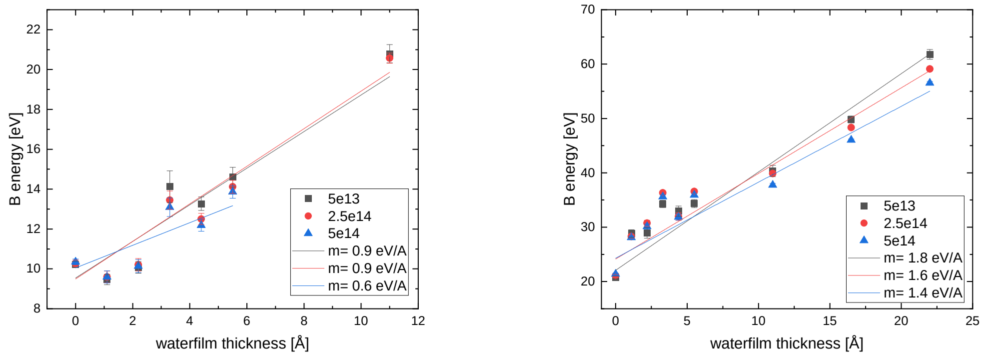

(a) **(b)**

Figure 8.6: *(a) Optimal B energy for the first maximum of B fraction for implantation in graphene when an ice layer is present. (b) Best B energy for second maximum in B concentration, if ice would be on the graphene.*

mask in the form of a layer on the graphene is used, it must be ensured that this layer is much thicker than the penetration depth of the ions, so that all recoils also remain trapped inside this layer. A capping layer to achieve a deceleration of the ions, as some groups strive for [14], leads to a significant contamination with foreign atoms, wherefore a deceleration of the ions should occur in front of the sample using electrostatic lenses or, like in our case, putting the sample on high potential. Furthermore, it can be assumed that there is no water film on the sample during implantation at room temperature, since no additional oxygen was detected in the graphene after implantation using Auger electron spectroscopy.

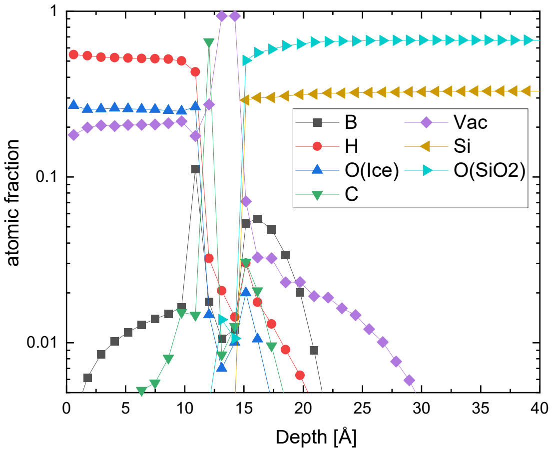

Figure 8.7: *Implantation profile of a 5×10^{14} at/cm² B implantation with 40 eV in a graphene sample, which is covered with 1.1 nm ice.*

8.2 TMDs

Another group of 2D materials modified by ULE ion implantation are transition metal dichalcogenides (TMDs). For this reason, the implantation of MoS_2 and $MoSe_2$ was also investigated using IMINTDYN. The question considered here is whether implantation modifies the ventral or posterior layer of the chalcogenes.

Although IMINTDYN cannot simulate crystal structure, a trick similar to that used for graphene was used to simulate the TMDs. Looking at the structure of MoS2, one find that it is also composed of hexagons, with only 3 of the atomic sites per layer occupied, resulting in a vacancy concentration of 66.7 % ($1/3$ through the unoccupied atomic sites $+1/3$ through the center of the ring per 1 whole atom per ring). In addition, a comparison of the two simulation methods (with and without vacancies) was performed to illustrate the influence of the crystal structure. For the initial configuration, 3 layers of chalcogen on 3 layers of Mo on another 3 layers of chalcogen were selected. The thickness of each layer is 0.72 Å and the atomic density was adjusted according to the selected vacancy concentration to get the right number of atoms per layer. In Fig. 8.8a and 8.8b the initial depth profiles for MoS_2 in SiO_2 with and without filler vacancies are plotted. For $MoSe_2$ the configuration would be identical except that Se was used instead of S.

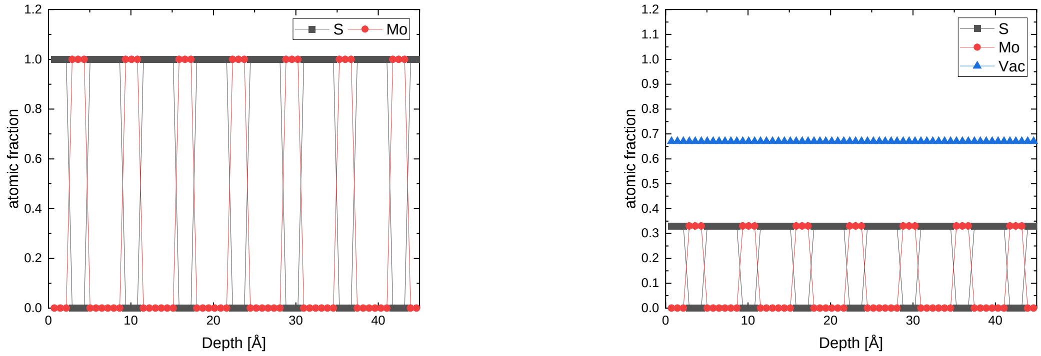

(a) **(b)**

Figure 8.8: *Start configuration of the bulk TMD target (a) without filler vacancies and (b) with filler vacancies.*

8.2.1 Cr in MoS_2

For the investigation of MoS_2, Cr was chosen as implantation atoms since these implantations were performed in the past to study transition metal substitution [22]. Here was investigated, at which energy most ions are implanted into the upper S layer firstly or into the lower S layer secondly. The sample system studied was free-standing MoS_2, 10 layers of MoS_2, which corresponds to the bulk at the energies considered, and MoS_2 on SiO_2. The values for the concentration were averaged over the 3 layers of one atom species, wich form one composed layer in each case. To investigate the influence of the vacancies on the simulation, the simulations were also performed without previously set filler vacancies, similar to SDTrimSP simulations. In order to have a better comparison between the use of filler vacancies and without their use, the vacancies were excluded for the evaluation of the atomic percentages. The same was made for the creation of the implantation profiles to ensure better comparability.

In Fig. 8.9 the atomic percentages in the first and second chalcogen layer (S layer) are plotted versus the implantation energy.

First of all, for the implantation in the top layer (8.9a and 8.9b), there is no difference between the used substrates or even freestanding films, mainly due to the fact that the structure consisting of 3 atomic layers already acts as a substrate itself on which the ions can be scattered back. The effect of decreasing Cr concentration with increasing energy can be seen, which is due to the generally higher penetration depth at higher implantation energies. A difference between the use of filler vacancies and without can hardly be detected. A small difference concerns the course of the concentration curves, which decrease somewhat faster,

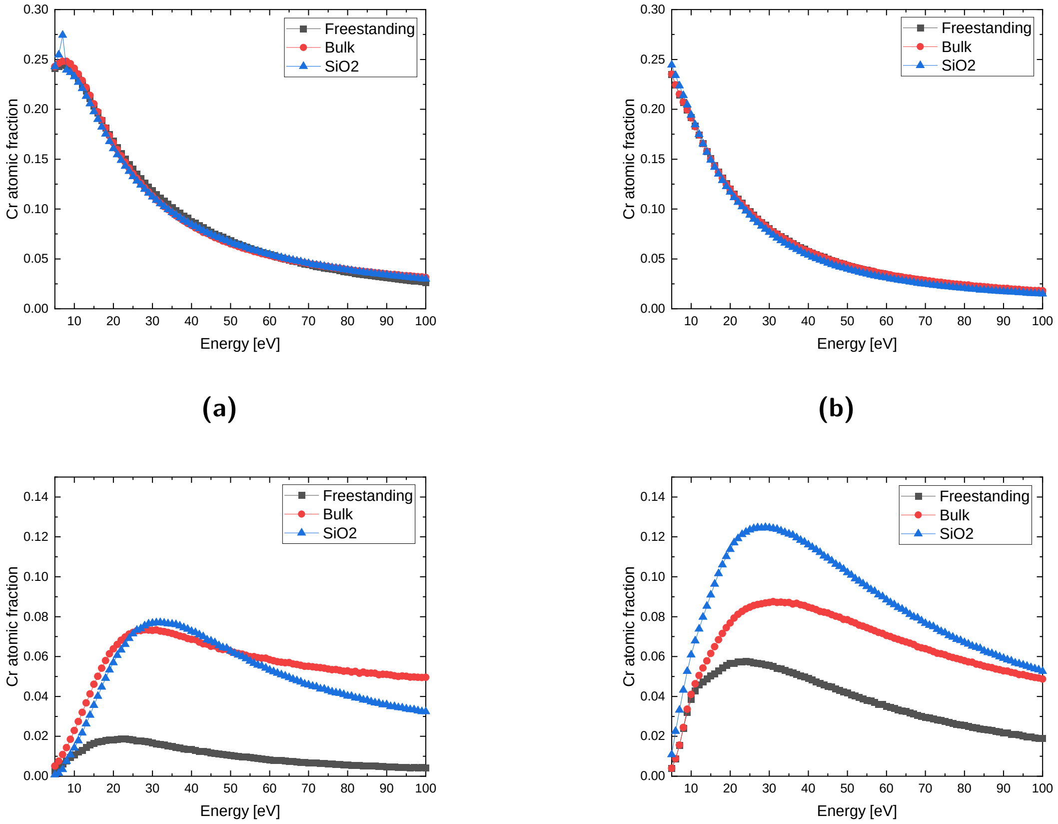

(a) **(b)**

(c) **(d)**

Figure 8.9: *Cr atomic fraction in the S layer versus implantation energy for MoS_2 on different substrate materials. (a) Top sulfur layer without filler vacancies and (b) top S layer with filler vacancies. (c) and (d) the 2nd sulfur layer without (c) and with (d) filler vacancies, respectively. The simulation was performed with a fluence of* 5×10^{14} *at/cm²*.

when filler vacancies are used. This is due to the fact that at higher energies, the ions can penetrate deeper into the material through the vacancies, since the ions are hardly deflected when they hit a vacancy, only due to weak collisions, and lose less to no energy. However, the concentrations are very similar and almost identical, especially at low energies.

When looking at the Cr concentration in the second S layer, a clear difference can be seen between the individual substances. This is mainly due to the fact that this is the last layer of the first MoS_2 layer. Thus, substrate effects are clearly more present. In the case of the free-standing MoS_2, the concentration is significantly reduced, since the ions cannot be scattered back from substrate atoms after passing through this layer. There is also a clear difference between the refinement of filler vacancies and without their refinement. The SiO_2 has a much stronger influence on the concentration in the second S layer than when a bulk material of MoS_2 is considered. This is due to the fact that in the simulated SiO_2 there are no vacancies in the crystal structure and thus each impact occurs at an atom. If MoS_2 is used as a substituent, this still implies a high concentration of filler vacancies where the ions cannot be reflected. Looking at 8.9c where the filler vacancies are not used, the concentration of the bulk material is similar to the concentration of SiO_2, because the ions can be reflected with each BCA step at an atom. Another difference concerns the energy at which the respective maximum Cr is reached in the layer. This is somewhat lower when using the vacancies, which is due to the fact that the ions have a slightly increased penetration depth overall and thus less energy is sufficient to penetrate the layer. Additionally, it can be seen that the general concentration is higher when filler vacancies are used, than when they are not. To explain this, one can have a look at the implantation profile over the entire target. In Fig. 8.10 the depth profiles after implantation of Cr in MoS_2 with and without filler vacancies are shown. The vacancies were excluded from the evaluation to allow a better comparison. A fluence of $5 \times 10^{14}\,\mathrm{at/cm^2}$ at an energy of 25 eV was simulated. The target was 10 layers of MoS_2, which corresponds to bulk behavior at these low implantation energies.

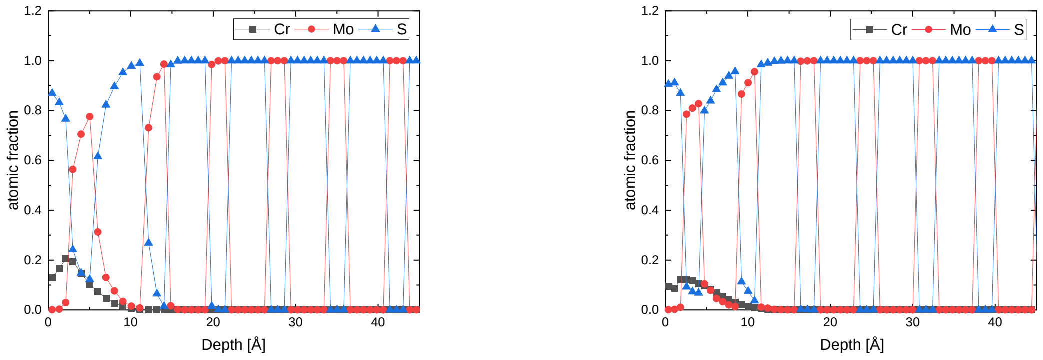

(a) **(b)**

Figure 8.10: *Implantation profiles of 25 eV Cr in MoS_2 at a fluence of $5 \times 10^{14}\,\mathrm{at/cm^2}$ without (a) and with (b) the consideration of filler vacancies.*

Here it can be seen that due to the vacancies in the system (8.10b), the penetration depth of the Cr ions is somewhat greater than in the system without vacancies. This is due to the fact that when a Cr ion hits a vacancy, its flight distance almost doubles. In contrast, in the system without vacancies, a much stronger Cr incooperation into the upper layers is observed and a stronger mixing and damage of the individual layers is visible, so that an alloy is formed between the Mo and the second S layer rather than separate layers of S and Mo. Without vacancies, the Mo layer acts as a strong barrier due to the exorbitant mass of the Mo atoms, which ensures that the Cr cannot penetrate further into the layer and thus collects especially at the interface between the first S and the O. The empty spaces show that the second MoS_2 layer is also implanted.

8.2.2 S in $MoSe_2$

For the investigation of $MoSe_2$, S was chosen as the implantation atom since these implantations are currently performed in coorperation with the group of Beata Kardynal from the Research center Jülich[1] and with the University of Duisburg-Essen with the group of Marika Schleberger[2]. It is also investigated at which energy most of the implantation atoms are implanted into the upper Se layer or into the lower Se layer on the one hand and possibly replace the Se on the other hand. The sample system used was again freestanding $MoSe_2$, 10 layers of $MoSe_2$, which corresponds to the bulk at the energies considered, and $MoSe_2$ on SiO_2. The values for the concentration were averaged over the 3 layers of one atom species in each case. To investigate the influence of the vacancies on the simulation, the simulations were also performed without previously set filler vacancies, similar to SDTrimSP simulations. In order to have a better comparison between the use of filler vacancies and without its use, the vacancies were excluded for the evaluation of the atomic percentages. In Fig. 8.11 the atomic percentages in the first and second chalcogen layer (Se layer) are shown versus the simulated implantation energy.

In the case of S implantation, the concentrations in the uppermost Se layer again hardly differ between the use of filler vacancies or their omission, although a slightly increased concentration is measured when calculating without filler vacancies. In addition, there is a slight difference between the freestanding and the bulk material in this case. The increase of the substrate effects in the 2nd Se layer can again be explained by the fact that this is the last layer of the $MoSe_2$ layer and therefore the substrate is present afterwards. The difference between the substrates again follows the same trend as for Cr implantation in MoS_2.

In Fig. 8.12 the depth profiles after implantation of S with and without filler vacancies are plotted. The vacancies were excluded from the evaluation to allow a better comparison. In each case, a fluence of $5 \times 10^{14}\,\mathrm{at/cm^2}$ was simulated at an energy of 25 eV. The target was 10 layers of $MoSe_2$, which corresponds to bulk behavior at these low implantation energies.

Similar results to Cr implantation in MoS_2 (8.2.1) are observed here. There is also significant mixing of individual atomic layers if filler vacancies are not considered, and a less damaging

---

[1] https://www.fz-juelich.de/de/pgi/pgi-9/forschung/arbeitsgruppen/liste-aller-arbeitsgruppen/quantenphotonik-ag-kardynal

[2] https://www.uni-due.de/physik/schleberger

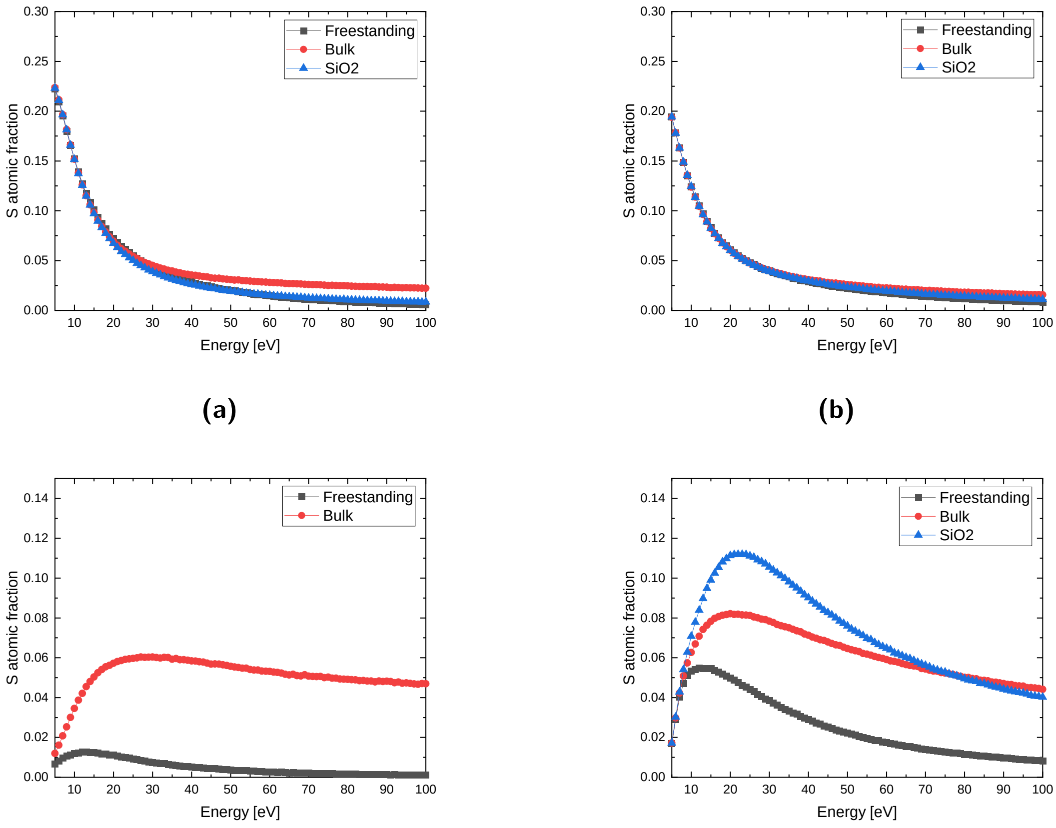

(a) (b)

(c) (d)

Figure 8.11: *S atomic fraction in the Se layer versus implantation energy for MoSe*$_2$ *on different substrate materials. (a) Top Se layer without filler vacancies and (b) top Se layer with filler vacancies. (c) 2nd Se layer without and with (d) filler vacancies, respectively. The simulation was performed with a fluence of* 5×10^{14} at/cm^2.

and uniform implantation profile if they are considered. The S also accumulates at the alloyed interface between Mo and Se with a strong damage in the first Mo layer. The damage to the entire system is also significantly increased without the vacancies and can be measured down to deeper layers which results from the generated recoils. Again, the results with filler vacancies are more likely and closer to reality, which is why the use of filler vacancies in the simulation of TMDs is always advantageous and should be carried out. In addition, it is advantageous to incorporate the individual atomic layers separately in the target in order to obtain a more precise implantation profile, which is not possible with a mixed target without observing the spatial arrangement of metal and chalcogen layers. In this way, it is easier to distinguish in which exact layer to implant and not only to calculate a general penetration depth. It should be mentioned again that the simulations only reflect the moment directly after implantation

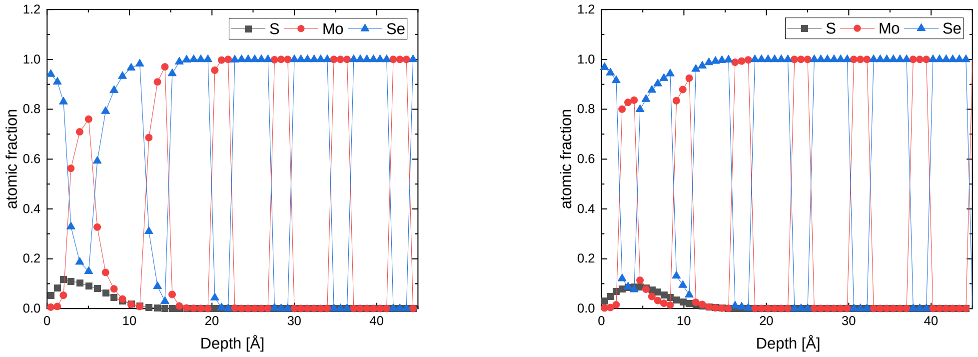

(a) **(b)**

Figure 8.12: *Implantation profiles of 25 eV S in $MoSe_2$ at a fluence of 5×10^{14} at/cm² without (a) and with (b) the consideration of filler vacancies.*

and cannot calculate chemical processes, annealing processes and the crystal structure and type of damage. Nevertheless, it provides a good indication of the energy that should be used for implantation and the extent of damage that can be expected in the material. However, it is not possible to distinguish whether the atoms introduced are substitutionally incorporated, interstitial or adatoms.

8.2.3 Capping layer on $MoSe_2$

Another proposed method for implantation in 2D materials is the use of a capping layer, through which high-energy ions are decelerated to stop at a defined depth [14]. To investigate this possibility, and in particular the number of recoils generated from the capping layer, the implantation performed in [14] was simulated using IMINTDYN. In the study, a 6 nm thick Si_3N_4 layer was deposited on $MoSe_2$ flakes and then irradiated with 7 keV Cl^+ ions at a fluence of 5×10^{14} at/cm² to obtain n-doping of $MoSe_2$ by the incoperation of Cl. The substrate on which the $MoSe_2$ flakes were placed was also Si_3N_4.

The system was simulated using IMINTDYN, modeling the $MoSe_2$ with filler vacancies as before (see 8.2 and 8.2.2). In Fig. 8.13 the simulated implantation profile after irradiation is shown. It can be seen that the majority of Cl ions are indeed present at the interface between Si_3N_4 and $MoSe_2$. However, the clearest results include the recoils from the capping layer. Thus, the concentration of Si and N in the top layers of the $MoSe_2$ flake is significantly higher than that of Cl. The fraction of Cl of all impurity atoms (Cl, Si and N) in $MoSe_2$ over the whole thickness, is only 13 % while Si accounts for 33% and N for 54%. Therefore, it is not

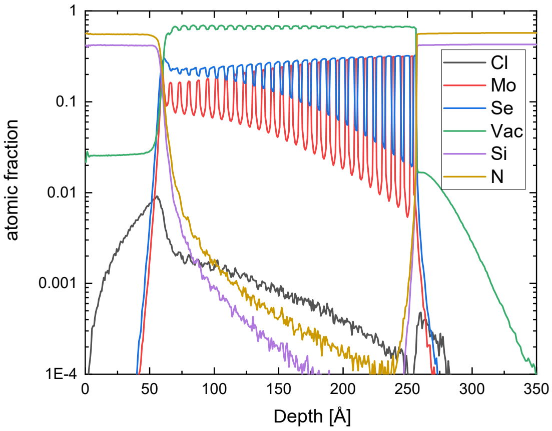

Figure 8.13: *With IMINTDYN simulated implantation profile of 7 keV Cl ions with a fluence of* 5×10^{14} *at/cm²* *in* $MoSe_2$ *through a 6 nm thick* Si_3N_4 *capping layer. A clear recoil production can be seen dominating the doping in* $MoSe_2$*.*

possible to say from which foreign atom the observed effects occur. However, it can be said that this method is highly unsuitable for performing clean implantation in 2D materials.

9 ULE-Implantations into Graphene

In this chapter, the implantations in graphene, which have been performed in the context of this thesis, will be discussed. These include some which have already been published [20, 21, 28, 29] and test studies to implant a lateral pn-junction in graphene. In [20, 21, 28] the implantation of the samples was performed in Göttingen within the framework of this work and the measurements and analysis were carried out by the group of Lino da Costa Pereira from KU Leuven. Since the analysis was done by other people, only the most important findings will be presented here.
In the following studies, the Raman measurements were performed with a confocal Raman microscope equipped wit a 532 nm Nd:YAG laser with a maximum power of 1 mW. The STM measurements were done using an Unisoku USM1000, an Omicron LT STM and an Unisoki USM1500. For the XPS measurements the SuperESCA beamline at the Elettra synchrotron in Trieste was used. The ARPES measurements were also performed at the synchrotron in Trieste using the BaDElPh beamline. The SKPM measurements were done in Göttingen by the author of this thesis.

9.1 Noble gas nanobubbles in graphene

The statements of this section are published in [28]. For this study, the required implantations in graphene were performed in Göttingen by Felix Junge and Manuel Auge. The evaluation and measurements were done in the group of Lino da Costa Pereira at KU Leuven. The manuscript was primarily written by Renan Villarreal and Pin-Cheng Lin. This study unveils the formation of graphene nanobubbles, which possess a remarkable radius smaller than 1 nm and are filled with He, Ne, and Ar and were produced by ultra-low energy ion implantation.

9.1.1 Experiment

CVD grown mono layer graphene on copper and platinum was implanted using ultra-low energy ion implantation. The implantation of the noble gases He, Ne and Ar was investigated.

The implantation energy was 25 eV and each irradiation was done with a fluence of 1×10^{15} at/cm². The implantations were performed at room temperature and a typical pressure of 5×10^{-8} mbar with a base pressure in the chamber of 5×10^{-9} mbar. For subsequent examination, STM and Raman measurements were performed together with MD and DFT simulations. Here STM were used to measure the dimensions of the noble gas bubbles and the MD simulations to calculate the pressure inside the bubbles. The measurements were conducted without any prior thermal cleaning. For more details see [28].

9.1.2 Results and discussion

Implantation as described above of graphene grown on Pt substrates produced nanobubbles whereas none were found for graphene on copper substrates. The observation suggests that only atoms trapped within defects become immobilized as intercalated species, while the rest are likely to escape through defects in the graphene, such as holes. The MD simulations confirm the presence of bubble instability in graphene on Cu. This may be due to the fact that the bond between graphene and copper is much weaker than that between graphene and platinum ($0.045\,\mathrm{eV}/\text{Å}^2$[137] vs. $0.251\,\mathrm{eV}/\text{Å}^2$[138]) and this bond cannot withstand the high pressure exerted by the bubbles. With STM the bubble sizes of less than 1 nm and more than 1 nm could be observed, which lead to a pressure, accordingly to MD simulations of up to 30 GPa. In summary, nanobubbles of different sizes were generated on graphene using noble gas ions, with stability observed on Pt but not on Cu substrates. The scaling behavior previously observed for larger bubbles broke down as the bubble size approached subnanometer scales. The characteristics and stability of the nanobubbles were attributed to the adhesion energies between graphene, the substrate, and the trapped noble gas element. The nanobubbles induced significant strain on the graphene, reaching levels of approximately 10%. MD calculations provided insights into the spatial distribution of trapped atoms, bubble morphology, and estimated van der Waals pressures exceeding 30 GPa in the smallest bubbles. In Fig. 9.1 STM images of the nanobubbles in graphene after the noble gas irradiation is displayed. The exact measurement results and their detailed interpretation can be found in [28].

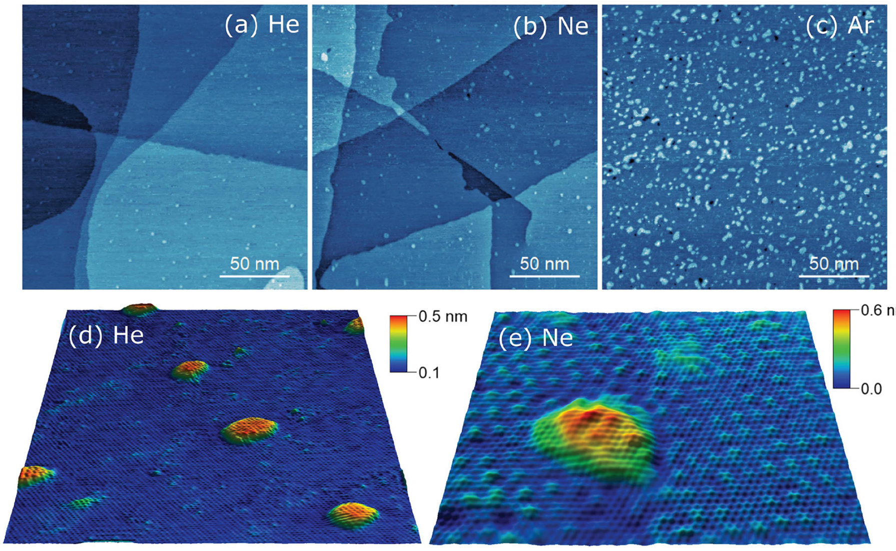

Figure 9.1: *STM images displaying (a) He, (b) Ne, and (c) Ar bubbles within the graphene on Pt. Additionally, (d,e) STM micrographs, capturing areas of* $20 \times 20\,nm^2$ *and* $10 \times 10\,nm^2$*, respectively, with atomic-level resolution, showcasing the continuous atomic lattice of graphene, especially above the bubbles. The Figure was made by Renan Villarreal and published in [28] under the CC-BY 4.0 licence.*

9.2 Thermal Annealing of Mn implanted graphene

The statements of this section are published in [20]. For this study, the required implantations in graphene were performed in Göttingen by Felix Junge and Manuel Auge. The evaluation and measurements were performed in the group of Lino da Costa Pereira at KU Leuven. The manuscript was primarily written by Pin-Cheng Lin and Renan Villarreal. In this study the effects of thermal annealing of Mn implanted CVD grown graphene is investigated. It was found that a minimum temperature of 525°C is necessary to recover from implantation-induced disorder.

9.2.1 Experiment

CVD grown mono layer graphene was implanted with 40 eV Mn. The fluence used was 1.5×10^{14} at/cm². Implantation took place at room temperature. The samples underwent analysis in their initial implanted state and were further examined following successive annealing processes conducted under ultrahigh vacuum conditions ($<5 \times 10^{-8}$ mbar), reaching temperatures up to 700°C. For comparison, unimplanted samples were also measured. Subsequently, STM, Raman, LEED, ARPES and XPS measurements were performed to investigate the graphene, where the XPS, LEED, ARPES and STM measurements were performed in UHV. For more details see [20]

9.2.2 Results and discussion

To investigate the surface cleaning by post annealing, XPS measurements were performed and show a reduction in O on the surface after annealing at 200°C and again after annealing at 425°C. The XPS measurements also reveal no significant change in the Mn content between the as implanted sample and the annealed one, regardless of temperature (up to 700°C). The LEED measurements show, that following a 20-minute annealing process at 425°C, the diffraction spots of graphene exhibited a notable improvement in sharpness, and the Moiré pattern resulting from the interaction between graphene and Cu(111) became visible, which also indicates a significant surface cleaning took place. To provide a more direct and quantitative characterization of implantation-induced disorder and its recovery, Raman spectroscopy was employed. As the annealing temperature increased, the disorder-related bands decreased in intensity, with significant recovery observed at 525°C and near-pristine graphene achieved at 700°C. These findings were consistent with previous reports and supported by STM imaging, which showed a well-ordered graphene lattice and Moiré superstructure in annealed samples. For Mn-implanted graphene, the ARPES data after annealing in UHV at 425°C and 700°C showed qualitative similarities to pristine graphene. However, the absence of significant cleaning in the XPS data between these annealing steps suggests that other modifications contribute to the improvement. The reduction in graphene disorder observed in the Raman study is expected to play a role in enhancing the spectral features. In terms of band structure parameters, the Dirac point position improved from approximately $BE = 0.52\,\text{eV}$ after annealing at 425°C to $BE = 0.43(1)\,\text{eV}$ after annealing at 700°C, with a gap opening of 0.23(2) eV. After annealing, the STM measurements show substitutional Mn defects, that proves, that the implantation with Mn took place. In summary, these findings indicate that the optimal annealing temperature for graphene is around 700°C. STM observations reveal a well-ordered graphene lattice on a nearly featureless surface, similar to pristine graphene, but with the addition of substitutional Mn atoms. ARPES measurements display a well-defined Dirac cone similar to pristine graphene, with only minor modifications likely caused by substitutional Mn and other implantation-induced effects. The surface cleaning achieved through thermal annealing at 425°C in UHV reduces photoelectron scattering from contaminants, allowing for clearer band structure probing. The improvement in ARPES spectral features between 425°C and 700°C annealing in UHV is attributed to further annealing of defects, leading to the restoration of a highly ordered lattice structure and well-defined band structure. In Fig. 9.2 STM images

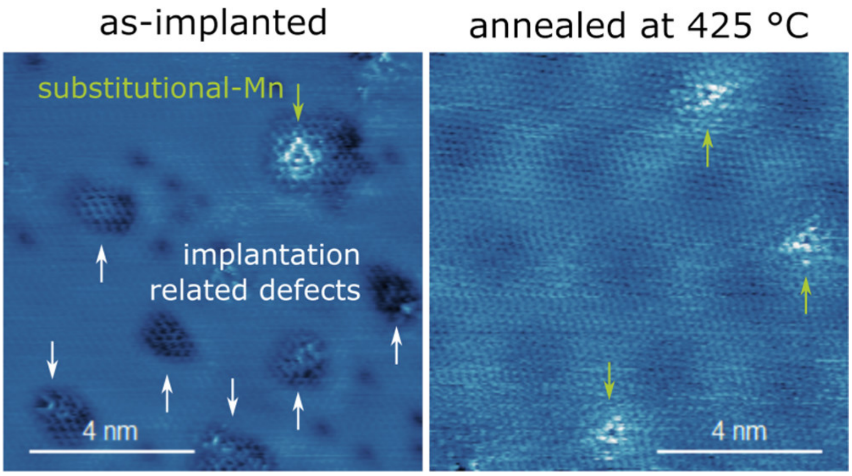

Figure 9.2: *STM images of graphene on Cu implanted with Mn as implanted and after annealing at 425° C. After the annealing a significant reduction of damage is visible together with the incorporation of Mn. Reprinted with permission from [20]. Copyright 2022 American Chemical Society.*

of the implanted graphene before and after annealing at 435° are shown. After annealing a significant reduction in damage is visible. The exact measurement results and their detailed interpretation can be found in [20].

9.3 Bond defects in graphene created by ultra-low energy noble gas ion implantation

The statements of this section are published in [21]. For this study, the required implantations in graphene were performed in Göttingen by Felix Junge and Manuel Auge. The evaluation and measurements were done in the group of Lino da Costa Pereira at KU Leuven. The manuscript was primarily written by Pin-Cheng Lin and Renan Villarreal.
In this study, the breaking of C-C bonds under ultra-low energy ion implantation was investigated. Noble gases were implanted in graphene on Cu and Pt and the density of the bond defect was investigated as a function of energy.

9.3.1 Experiment

CVD grown mono layer graphene layers on Cu and Pt were used as samples and implanted with He, Ne or Ar at low energies between 15 and 40 eV. Subsequently, the samples were examined by STM, Raman and XPS without prior annealing. Ion implantation took place at room temperature. A fluence of 1×10^{15} at/cm^2 was used in each case. The typical pressure during implantation was in the range of 5×10^{-8} mbar with a base pressure in the chamber of 5×10^{-9} mbar. Noble gas implantations were chosen because their inert nature means that they do not undergo chemical reactions with the carbon atoms, thus minimizing additional damage apart from the collision mask during implantation. However, for Pt substrates bubble formation may take place (see. 9.1). For better understanding of the experiments, additional MD simulations were performed with the PARCAS code. For more details see [21].

9.3.2 Results and discussion

The Raman data from the graphene on Pt show an appearance of a D-band together with a broadening of the G band, accompanied by a reduction of the 2D-band (for Raman modes of graphene see ch. 5.3.1). These observations suggest an increase in disorder even at energies down to 15 eV. Since the energy transfer would be to low to form a stable vancancy, another form of defect was created. The MD-simulations performed, showed that even at this low energies, the carbon gets removed from the graphene plane, by breaking one C-C bond and form a new bond with the substrate. Even if these atoms are no longer in the graphene, they are still bound to the C atoms and are therefore no vacancies but so-called bond defects. With higher implantation energy and higher ion mass, the number of bond defects increases. The Raman measurements of the graphene on Cu as well the STM measurements could confirm this behavior of the C atoms during the implantation. With the STM, no vacancies could be detected at the energies used. This may be related to the high mobility of vacancies, but it indicates that in this energy regime the generation of bond defects is clearly preferred over vacancies.

When dangling bonds are created, they are highly reactive and would react with other molecules and atoms, either with the substrate or the atmosphere. However, even if the XPS data show an increase of hydrocarbon contamination after the implantation, the amount of this is largely independent of the mass or species of implanted particle. Therefore, it can be concluded that the bonds are mostly passivated by the substrate. In Fig. 9.3 snapshots from the MD simulation showing the formation of C-Pt bonds and the breaking of C-C sp^2 are displayed. The exact measurement results, their quantitative analysis and their detailed interpretation can be found in [21].

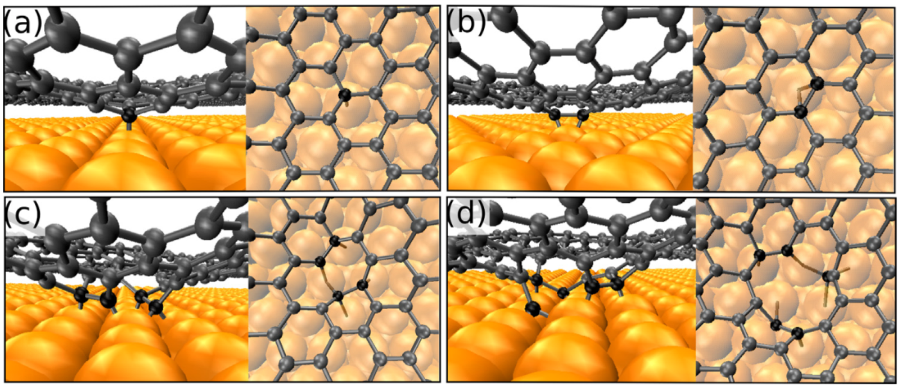

Figure 9.3: *Images extracted from MD simulations following ion impacts, illustrating the creation of bond defects. In these snapshots, one can observe the rupture of C-C sp^2 bonds (gray), leading to the displaced carbon atoms (black) establishing new connections with the Pt surface (orange). Provided are examples showcasing (a) a single bond defect from both side and top views, (b) two bond defects, (c) four bond defects, and (d) five bond defects resulting from a solitary impact. Reprinted with permission from [21]. 2022 Elsevier Ltd.*

9.4 Lateral controlled doping

The results and large parts of this section are also published in [29] and the text was only slightly adapted[1]. The manuscript was mainly written by the author of this thesis. To pave the way to a lateral p-n junction in graphene and to test the possibilities of the new deceleration unit (ch. 6.5), graphene was implanted using electrostatic masks. Subsequently, the transition area between the doped and un-doped areas was investigated.

9.4.1 Experiment

The new deceleration unit with electrostatic mask was used for the implantations. The shielding electrode was used in non conctact mode. In the experiment, the deflection electrode hovered approximately 1 mm above the sample and was charged to either +100 V or +300 V relative to the sample potential of -20 V relative to the accelerating voltage of 30 kV . This causes deflection of incoming ions, which possess an energy of a few tens of electron volts at this stage, redirecting them away from one side of the sample. The implantation energy was 20 eV. As samples monolayer graphene on Ni and SiO_2, obtained from Graphene Supermarket[2] were used. Boron was implanted at fluences of 5×10^{14} at/cm^2 and 1×10^{15} at/cm^2.

---

[1] The corresponding text passages in this paper were prepared by the author of this thesis

[2] (Graphene Laboratories Inc., Ronkonkoma, NY, USA, https://www.graphene-supermarket.com)

Subsequently, SKPM measurements were conducted on the samples to determine the surface potential across the sample and analyze the sharpness of the transition between the implanted and un-implanted regions. The SKPM measurements were performed by an Atomic Force Microscope available at the institute of materials physics in Göttingen, type MFP-3D Origin+ from Oxford Instruments Asylum Research (Oxford Instruments GmbH, Wiesbaden, Germany), in SKPM non-contact constant height mode. The surface potential was determined by averaging over measured areas of $5\,\mu\mathrm{m} \times 5\,\mu\mathrm{m}$.

9.4.2 Results and discussion

The results of the SKPM measurements are shown in Figure 9.4. There is a clear distinction between the doped and undoped areas. In addition, the change in the surface potential is correlated with the fluence used. It should also be noted here that the different substrates also have an effect on the level of the potential and therefore a direct correlation between the fluence and the surface potential achieved cannot be determined. What can be measured, however, is the width of the transition region in relation to the applied deflection voltage. Thus, at 100 V deflection voltage, a transition region with a width of about 1 mm (Fig. 9.4a) is achieved, while the transition region for the sample with 300 V deflection voltage only has a width of just under 0.5 mm (Fig. 9.4b). In addition, an increase in the surface potential, and thus higher doping, at the interface can be seen at higher deflection voltages. This is due to the fact that the ions, which are deflected, are pushed to the sides and generate a higher fluence there. This only occurs on the implanted side, since the other side is completely shielded by the hovering electrode. The ion trajectories simulated with SIMION are listed in [25]. There one can see that the trajectories hitting the probe directly at the interface have a higher density. Since different substrates were used, it can be concluded that the higher surface potential indicates doping or damage to the graphene and not from implantation into the substrate.

These experiments show that graphene can be doped with different energies in only one implantation step by using electrostatic masks. Furthermore, it can be doped with different fluences at different sample spots in only one implantation step. Additionally, by adjusting the deflection voltage, the transition region between the doped and the un-doped regions can be be adjusted.

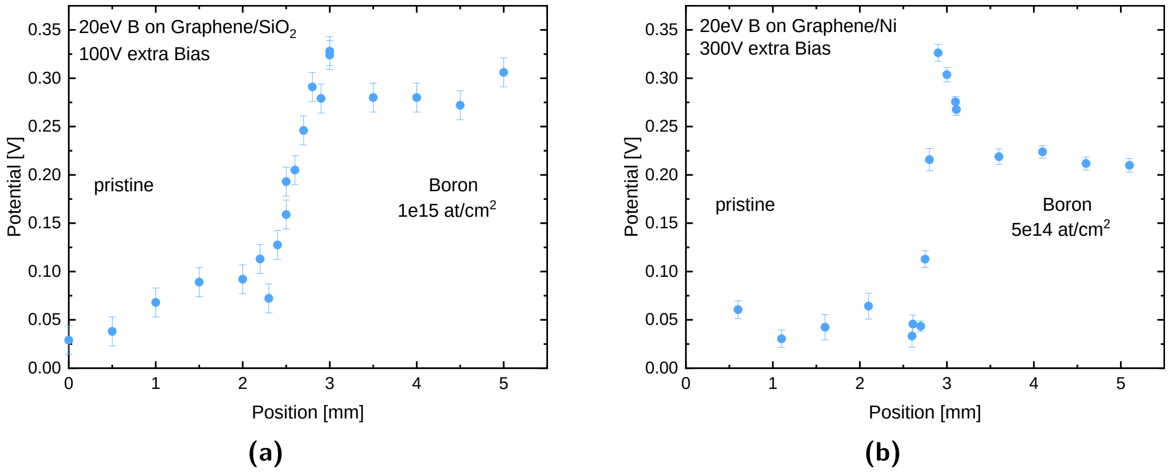

Figure 9.4: *(a) SKPM measurement of a graphene layer on SiO$_2$ previously implanted with 1×10^{15} at/cm^2 with B with an energy of 20 eV. In addition, only a part of the sample was implanted using an electrostatic mask. The voltage at the mask was set to +100 V corresponding to the sample bias. (b) SKPM measurement of a graphene layer on Ni previously implanted with 5×10^{14} at/cm^2 with B at an energy of 20 eV. The voltage for masking was set to +300 V in respect to the sample bias. The comparison shows a sharper transition region (≈1 mm to ≈0.5 mm) with increasing deflection voltage. The position indicates the relative position to the edge of the sample. (These figures are also published in [29] under the CC-BY 4.0 license).*

9.5 Damage study of Graphene using electrostatic masking

The results and large parts of this section are also published in [29] and the text was only slightly adapted[3]. The manuscript was mainly written by the author of this thesis. To investigate the implantation energy dependent damage of graphene, graphene on SiO$_2$ was bombarded with He ions.

9.5.1 Experiment

In this case also the new deceleration unit with electrostatic mask was used for the implantations in contact mode. To create an energy gradient across the sample, two 20 nm copper contacts were first sputtered onto both sides of the sample. Then, a constant voltage, of 100 V was applied between the two contacts. The ground contact on the graphene was set to 0 V in respect to the 30 kV of the anode of the source. Thus, He ions with energies of 0-100 eV could be implanted along the sample, since the current flow through the graphene layer results in a

---

[3] The corresponding text passages in this paper were prepared by the author of this thesis

linear potential gradient along the surface. In Fig. 9.5a the mounted and contacted sample is shown on the sample holder. It can be seen that the copper contacts have a relatively wide transition area due to the sputtering. In Fig. 9.5b the specimen is shown again schematically with the applied voltages. Batteries were used for contacting, since they provide a stable DC voltage. Tests with a normal power supply resulted in the small fluctuations in the voltages due to the rectifier of the power supply distorting the current measurement on the specimen. Because previous studies [28] have shown that lateral homogeneous He implantation is possible, He was again chosen. A total fluence of 1×10^{15} at/cm² was used for implantation.

In addition, IMINTDYN simulations of this experiment were performed to compare both and get a better understanding of the implantation process. For details about the simulations see ch. 7. The damage formation was determined using Raman spectrometry. Raman spectra were measured using a confocal Raman microscope equipped with a 532 nm Nd:YAG laser. The laser was directed onto the sample surface through an objective (OLYMPUS, X43 100x, N.A. 0.7), with the maximum laser power remaining below 1 mW in order to avoid laser-induced modification. All the measurements were obtained in ambient conditions, at room temperature. The Raman measurements were done by Zviadi Zarkua at the KU Leuven.

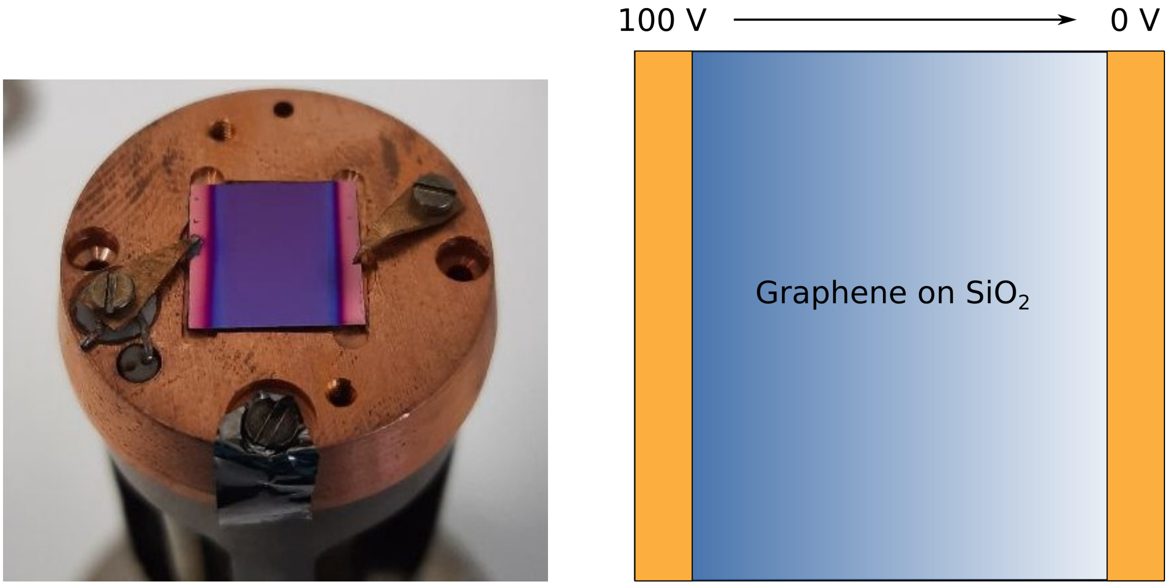

(a) (b)

Figure 9.5: *(a) Picture of the graphene specimen mounted on the specimen holder with copper contacts. The right contact was grounded to 100 V, while the left one was grounded to 30 kV. (b) Schematic representation of the voltage curve across the sample for implantation of 100 eV to 0 eV ions.*

9.5.2 Results and discussion

Experimental In Figure 9.6 different Raman spectra for different sample surface positions of the He implanted sample are shown. The positioning describes the distance in respect to the grounded electrode. Therefore, lower positions corresponds to lower implantation energy. The gradient can be approximately assumed to be linear, since the resistance across the graphene layer should not change. Along the sample surface, a clear shift of the D-peak as well as a broadening can be seen. Another indication for a large damage is provided by the 2D-peak, which gets smaller with higher He energy until it almost disappears. For $x > 3\,\mathrm{mm}$ the graphene becomes more and more amorphous, presumably due to the high fluence of 1×10^{15} at/cm^2. This is shown by the broadening of the G-peak and the merging with the D'-peak due to the broadening of the D-band, which indicates the loss of the crystal structure is thus also a sign of higher damage to the graphene [139, 140]. A typical Raman spectrum of graphene from graphene supermarket before and after an ion implantation can be found in [141]. Similar to our results, a decrease in the 2D-peak and an increase of the D-peak after the implantation was observed as damage increases. It should be noted that the first measuring point already shows a clear damage formation, since the 2D-peak is already smaller than the D-peak although at this position the implantation energy of around 1-5 eV is too small for vacancy formation. However, intercalation of He between the graphene and the substrate can still occur which leads to damage as well as the graphene was probably slightly damaged by the sputtering process when applying the copper contacts. Another reason could be the shipment to Belgium were the Raman measurements took place. These measurements only serve as a proof of concept, since due to the strong initial damage caused by the copper contacts and the high fluence of the implanted ions, it is not possible to make a quantitative statement about the damage compared to the implantation energy. This is partly because the exact field gradient over the sample was assumed to be linear, but can deviate from this due to various disturbances in the graphene. Nevertheless, these measurements show a clear trend towards more damage at higher ion energies, similar to results of laterally uniform implantations [21].

Simulations The He ion energies 20, 40, 60, 80 and 100 eV were simulated with fluences of both 5×10^{14} at/cm^2 and 1×10^{15} at/cm^2. Furthermore, the fixed density option was not used, but an error function, that leads to a diffusion of the He out of the sample, to take the noble gas character of He into account. The results in the composition of the first nanometer of the sample are shown exemplary in Figure 9.7. It is shown that the carbon content in the first layer decreases after implantation and is replaced by either vacancies, He or atoms from

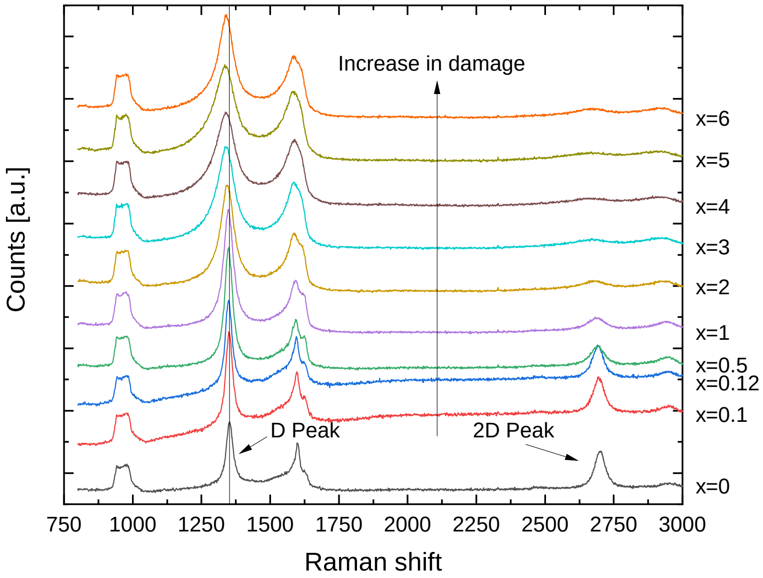

Figure 9.6: *Raman spectra of the He implanted sample. The spectrum was measured on different positions on the sample. Here, x is in mm, where* $x = 0$ *describes the position directly at the 0 V contact. With higher x also the He energy increases from* $E_{He} \approx 0$ *t* $x = 0$ *mm to* $E_{He} \approx 100$ *eV at x>6 mm. A clear shift of the D-peak and a broadening due to a higher implantation energy at larger x can be seen. (This figure is also published in [29] under the CC-BY 4.0 license).*

the substrate. In this extreme case, the carbon concentration drops by 10.9 % from 66.7 % to 59.4 %. In addition, it can be observed that some of the carbon atoms can be incorporated into the substrate by recoil formation and that the uppermost layers of the substrate are also damaged, seen in a increase in vacancies and loss of Si and O. This shows that already at these low energies a certain amount of recoils are generated which are incorporated into the underlying layers, and therefore the application of a capping layer to slow down the ions can lead to further damage of 2D materials and to incorporation of unwanted foreign atoms. The trend of the carbon decrease with higher energy is shown in Figure 9.8. It can be noticed that with higher He energy and higher fluence, more carbon is removed from the first layer. The missing carbon content in the first layer in relation to the undamaged graphene can be comprehended as a measure of damage. Here, the simulation confirms the higher defect density at higher implantation energies. In addition, it can be seen that in this energy regime, the fluence has a significantly greater influence on damage formation. Therefore, it is not surprising that the Raman spectrum shifts toward amorphous carbon for the fluence used in the experiment. The damage is caused on the one hand, by the creation of vacancies and on the other hand, by the incorporation of free atoms, either He or atoms of the substrate, which can be incorporated into the uppermost layers due to sputtering processes.

Figure 9.9 shows the fractions of introduced He, vacancies, Si, and O from the substrate into the top graphene layer after implantations in dependence of the implantation energy. For He (Fig. 9.9a) it can be seen that a maximum is reached at 20 eV. This is due to the fact that at higher energies the He is implanted deeper into the sample and thus penetrates the graphene layer more and more. For the vacancies (Fig. 9.9b) it can be seen that the vacancies first increase from the initial value of 33.3 %. Subsequently, the concentration falls again, with higher decrease at higher fluence, so that initially at the fluence of 1×10^{15} at/cm² and energies of up to just below 60 eV more vacancies are generated. At higher energies, more vacancies were generated in the top layer for the lower fluence of 5×10^{14} at/cm². For Si (Fig. 9.9c) and O (Fig. 9.9d) it can be seen that with increasing energy the fraction of these substrate atoms in the graphene layer also increases, this is further pronounced with higher fluence. The decrease in the vacancy concentration with a simultaneous decrease in carbon can be explained by the introduction of Si and O into the graphene layer, with O having a significantly greater effect. This effect is more pronounced at higher energies and can be explained by the scattering kinematics. When He hits Si or O, the resulting recoil can only go in the forward direction. In order to be incorporated into the graphene, a further scattering of the generated recoil with a substrate atom must subsequently take place. To have enough energy for the second scattering in the cascade, the first collision of He with Si or O must transfer sufficient high energy, thus this process becomes more likely with higher He energies. Another process is the backscattering of He in deeper substrate layers and the subsequent collision of He with Si or O on its way back. In this way, Si or O is also scattered towards the surface and can be incorporated there. The proportion to which these processes take place depends on the He energy. Thus, the process via the cascade has a fraction of 83 % (17 % via a direct collision with backscattered He) at 100 eV and of 53 % (47% via a direct collision with backscattered He) at 20 eV. The energy transfer to C, O and Si can be calculated by the kinematic factor and has its maximum at 180° backscattering angle (cf. section 5.2.2). Under these conditions, the maximum transferred energy is 75 % for C, 64 % for O and 43.75 % for Si. Due to the $1/E^2$ dependency of the backscattering cross section (eq. 5.8), where E is the projectile energy, the high backscattering yield is reasonable in the ultra-low energy regime. The fact that more O than Si is incorporated into the graphene is due to the double O concentration in the substrate (SiO_2) as well as to the lower mass of O, therefore the backscattering in the second collision of the cascade is more probable.

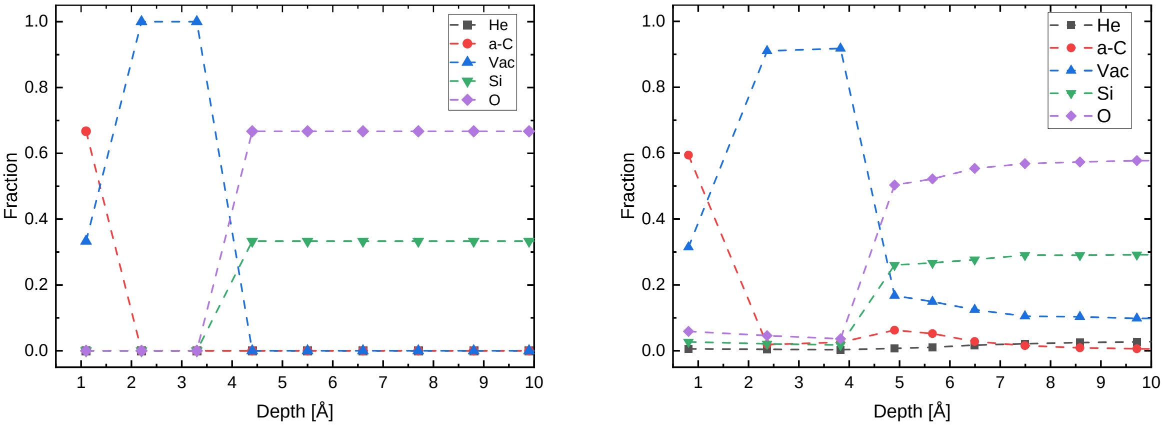

(a) *Unimplated layer structure as start condition for IMINTDYN.*

(b) *After implantation of 100 eV He with* 1×10^{15} *at/cm²*.

Figure 9.7: *Start condition of the IMINTDYN simulation of graphene on* SiO_2 *(a) and after He implantation at 100 eV with a fluence of* 1×10^{15} *at/cm². (b) After the implantation, damage to the graphene due to He, vacancies and substrate atoms is clearly visible in the top atomic layer. (This figures are also published in [29] under the CC-BY 4.0 license).*

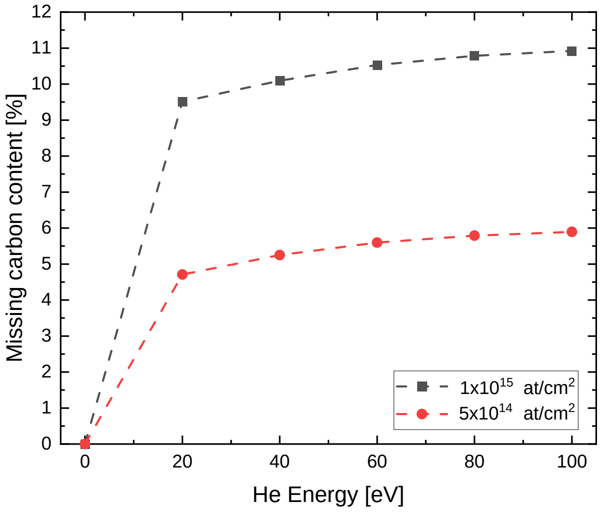

Figure 9.8: *Values of missing carbon content in the top layer versus He implantation energy from the IMINTDYN simulations. A clear trend towards higher damage to the graphene at higher He energy is becoming apparent. (This figure are also published in [29] under the CC-BY 4.0 license).*

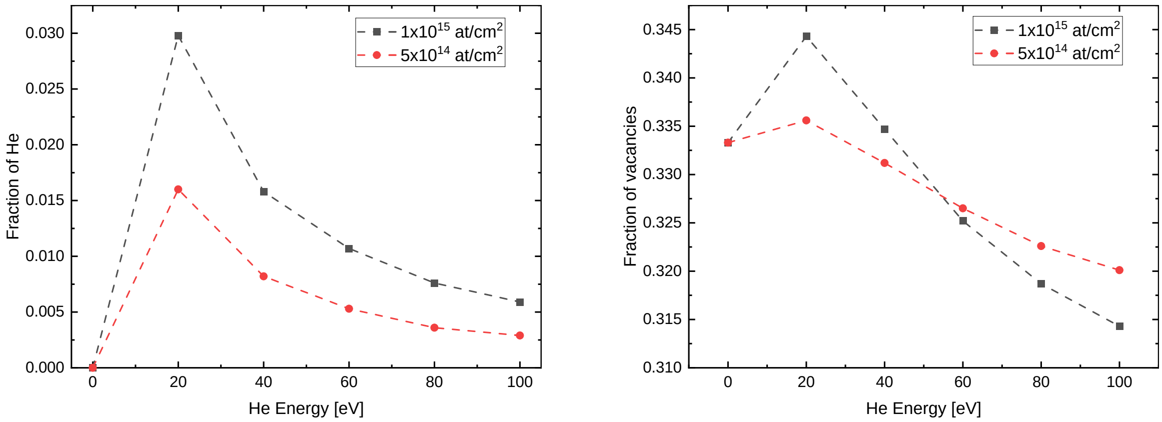

(a) *Helium concentration in the first layer.* **(b)** *Vacancy concentration in the first layer.*

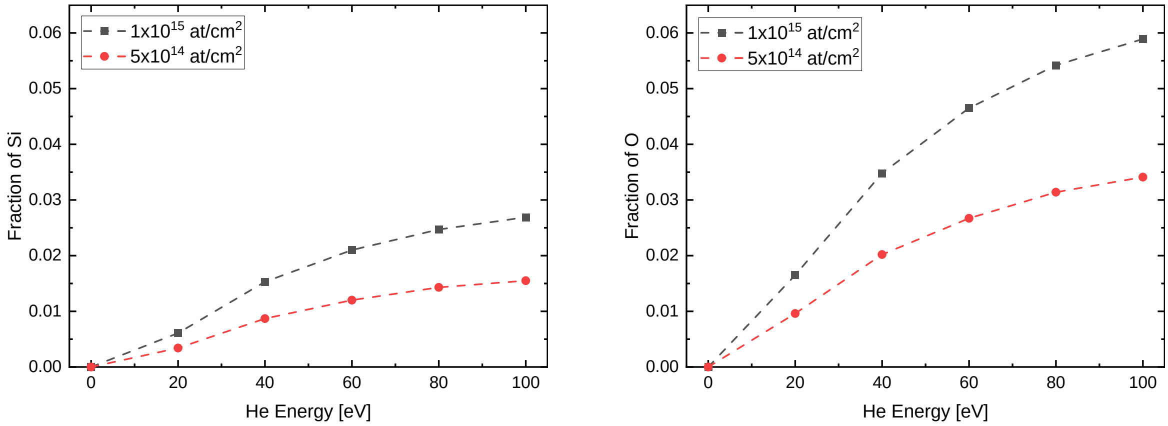

(c) *Silicon concentration in the first layer.* **(d)** *Oxygen concentration in the first layer.*

Figure 9.9: *Concentrations of impurity atoms (a) He, (b) vacancies, (c) Si, and (d) O in the top graphene layer after implantation of He with different energies and fluences of* $1 \times 10^{15}\,{}^{at}/_{cm^2}$ *and* $5 \times 10^{14}\,{}^{at}/_{cm^2}$*. (This figures are also published in [29] under the CC-BY 4.0 license).*

9.6 Test of implanting a lateral pn-junction in Graphene

Based on the results of lateral inhomogeneous implantation in graphene, it was tried to implant a lateral pn-junction in graphene. Since the creation of a lateral pn-junction is possible by doping with B and N [58], these elements were also chosen for the implantation for p and n doping, respectively.

9.6.1 Experiment

Again, graphene on SiO_2 samples was used. The SiO_2 serves as an insulator layer between the graphene and the Si substrate so that the current can only be measured via the graphene layer. First, gold contacts were deposited on the sample and then wire bonded to record current-voltage characteristics. For the implantation, the wires had to be removed, otherwise electrical contact between the sample on the sample holder and the electrostatic mask would have occurred, resulting in a short circuit. The implantation was performed in two steps. First, the entire specimen was implanted with N. Then, the electrostatic mask was used to shield a part of the sample and a second implantation with B took place. Here, the B fluence was chosen to be twice as high as the N fluence to compensate for the n-doping of the p-doped side. In each case, an energy of 20 eV was chosen as the implantation energy. Fluences of $1 \times 10^{14}\,\mathrm{at/cm^2}$ N and $2 \times 10^{14}\,\mathrm{at/cm^2}$ B in one experiment, and fluences of $2 \times 10^{13}\,\mathrm{at/cm^2}$ N and $4 \times 10^{13}\,\mathrm{at/cm^2}$ Bin another experiment were implanted. During the implantations, a pressure of about 10^{-8} mbar was present in the chamber. In Fig. 9.10 the mounted and bronze-tipped sample is shown. The bar across one side of the specimen serves as an electrostatic mask to which 400 V was applied as a deflection voltage. The bar hovers about 1 mm above the specimen surface, as in the previous experiments (see section 9.4). After implantation, the specimen was re-contacted by wire bonding and current voltage characteristics were again recorded. Since significant damage was expected from the implantation, the samples were then cured under vacuum ($<10^{-4}$ mbar) for 25 min at 525-530 °C and the measurements were repeated. The annealing temperature and time were chosen according to the results in [20]. Annealing could not be carried out in the UHV of Adonis, as temperatures of only slightly more than 200°C can be reached there.

9.6.2 Simulations

The implantation was also simulated with IMINTDYN. Again the Kr-C potential and stopping powers of SRIM were used. To simulate the implantation with B, the output of the first implantation simulation was used as input to draw an accurate picture of the double implantation. The $2 \times 10^{13}\,\mathrm{at/cm^2}$ N and $4 \times 10^{13}\,\mathrm{at/cm^2}$ B implantation was simulated.

Fig.9.11 shows the implantation profiles of the n-doped (Fig. 9.11a) and the p-doped (Fig. 9.11b). In this case, the vacancies were previously calculated out of the C layer, so that the listed atomic percentages correspond to the actual atomic percentages.

It can be seen that there is actually about twice as much B (0.61 at.%) as N (0.32 at.%) in the p-doped side of the graphene. Also, the fraction of N in the graphene is not affected by the subsequent B implantation. Whether this changes at higher fluences would have to be clarified by further simulations. As far as the damage to the graphene is concerned, it can be seen that after the second implantation the fraction of O and Si in the graphene layer increased

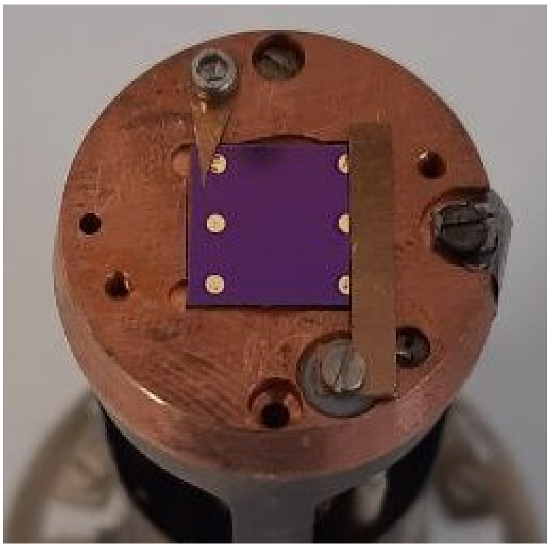

Figure 9.10: *Picture of the mounted graphene on SiO_2 on the sample holder. The 6 gold contacts were applied to the graphene layer and are used to attach the bond wires. The copper tip serves as an electrostatic mask to which a positive voltage is applied to shield the ions from this site of the sample and is not in contact with the sample ($h \approx 1$ mm). The bronze tip (top left) is used to contact the graphene layer.*

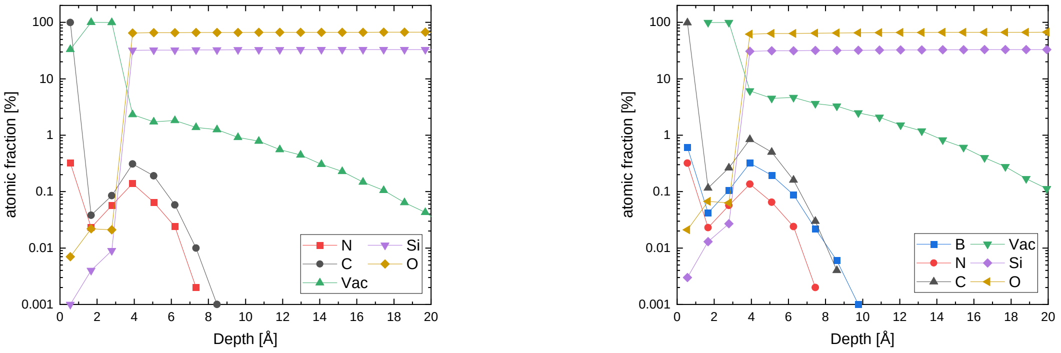

(a) **(b)**

Figure 9.11: *(a) Implantation profile after the N implantation for the p-n test. Corresponds to the p-doped site. (b) Implantation profile after the B and N implantation for the p-n test. Corresponds to the p-doped site.*

by a factor of 3 (from 0.007 at.% to 0.021 at.% for O and from 0.001 at.% to 0.003 at.% for Si). However, this is to be expected, since the total fluence with which the irradiation was performed was also increased by a factor of 3. Again, many implantation atoms end up in the substrate, due to the hollow structure of the graphene lattice with filler vacancies.

9.6.3 Results and discussion

The results of the current-voltage measurements are shown in Fig.9.12. It is clear that no pn-junction could be produced in either of the two samples. Even after subsequent annealing of the sample, this did not change. However, it can be seen that damage to the graphene has occurred as a result of the implantation. For example, the conductivity of the graphene layer in the first sample changed from 1.56×10^{-3} S to 8.56×10^{-5} S after the implantation of B and N. The annealing was able to repair part of the damage, so that the conductivity increased again to 1.67×10^{-4} S. In the second sample, which was irradiated with lower fluence, no pn-junction could be generated either. Once more, not all of the damage could be repaired by the annealing. Thus, the conductivity fell from 1.13×10^{-3} S to 9.52×10^{-4} S after implantation and subsequent annealing. Conductivity measurements along one side of the sample gave conductivities of 6.25×10^{-4} S on the only N doped side and 1.03×10^{-4} S on the B and N doped side, for the sample with the 1×10^{14} at/cm² N and 2×10^{14} at/cm² B fluence after annealing. The fit errors of the conductivity values are 4-5 orders of magnitude below the value and are therefore negligible not listed again. From this it can at least be concluded that some implantation has taken place and that the fluence has an influence on the damage and thus the conductivity. Unfortunately, it is not possible to calculate the theoretical conductivity along the sample from the values at the edges, since neither the exact position of the shielding area for the B implantation is known, nor can the values at the edges be transferred exactly to the entire layer, since they are distorted by the middle gold contacts.

To find out what happened during the implantation and no pn-junction was produced, additional SKPM measurements were performed on the sample implanted with 1×10^{14} at/cm² N and 2×10^{14} at/cm² B to measure a possible transition in the surface potential. The results are shown in Fig. 9.13. Here, a transition was made from the mean gold edge on the N implanted side to the middle gold contact on the N and B implanted side. The points directly at the contacts (distance <0.1 mm) are marked in orange. These measurements show no clear change in surface potential but fluctuates around -80 mV throughout the sample. The only change occurs directly near the first contact. However, it is not clear whether this is due to a change caused by the implantation or due to the influence of the gold contact. The two points, which are marked in the red area, are measurement errors, because during these measurements the AFM tip had lost the contact to the surface temporarily and therefore these values are falsified and were not used for the interpretation of the measurement.

From these data, several possible errors can be identified. On the one hand, implantation may have occurred, as evidenced by the change in conductivity, but no or insufficient impurities

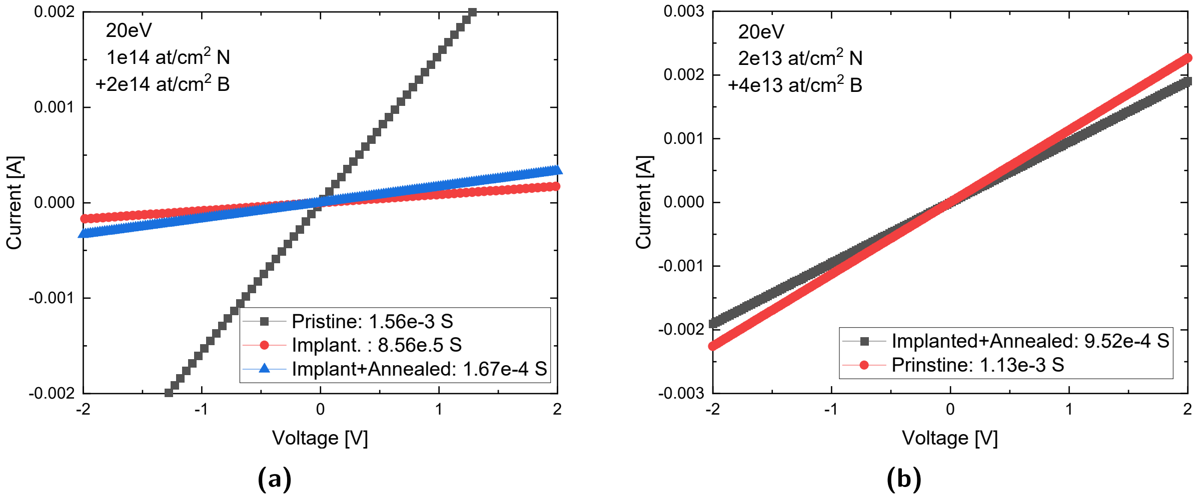

Figure 9.12: *(a) Current-voltage characteristics of graphene on SiO$_2$ before and after implantation with 20 eV 1×10^{13} at/cm^2 N and additional lateral selected 20 eV 2×10^{13} at/cm^2 B and subsequent annealing at 525° C. (b) Current-voltage characteristics of graphene on SiO$_2$ before and after implantation with 20 eV 2×10^{13} at/cm^2 N and additional lateral selected 20 eV 4×10^{13} at/cm^2 B and subsequent annealing at 525° C.*

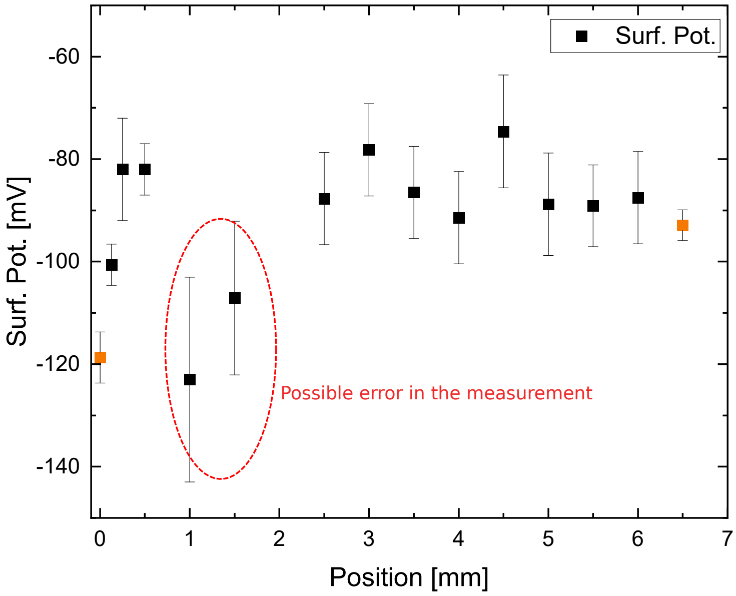

Figure 9.13: *SKPM measurement of graphene on SiO$_2$ after the implantation of 1×10^{14} at/cm^2 N and 2×10^{14} at/cm^2 B using the electrostatic masking and annealing at 525-530° C for 25 min. The orange contact are measurement points close to the gold contacts.*

may have been incorporated into the graphene lattice. Wang et al. [58] report about 1.3-5.2% impurity atoms for B and 1.8-5.6 % for N in the graphene lattice for their pn-junction. From previous studies it is known that only about 10 % of the implanted atoms are actually incorporated into the graphene at the energies and fluences used [17]. Thus, the implanted density of impurity atoms would still be too low by about a factor of 4, since 1×10^{14} at/cm^2 would only give us about 0.25% impurity atoms. However, since we already see large damages under these implantation conditions, which cannot be easily repaired by the subsequent annealing, either the annealing process should be adjusted afterwards or implantations should be performed at already elevated temperature, which show an increased retention rate at least for TMDs [22]. Higher fluences would damage the graphene even more, which makes the necessity of a successful annealing step even more important Another explanation, which also involves the SKPM measurements, is that the electrostatic mask failed. This would explain why the surface potential does not change across the sample. Even though the conductivity measurements on only one side of the sample showed that the doubly implanted area has more damage, it is still possible that the junction area is too close to the gold contacts and thus they show a significant influence on the current voltage behavior. Spatially resolved element measurements such as XPS, which measure the B or N content along the sample, could at least give an indication of whether the implantation worked as desired. A precise statement about the whereabouts of the ions would still be provided by STM measurements, in which the impurity atoms in the graphene lattice can be identified and counted.

Another source of error could be the sample itself. The graphene used was not grown directly on the SiO$_2$ but transferred. In this case, PMMA residuals may remain on the graphene, which impede the implantation. The shearing of the graphene after implantation can then be explained by recoils from the PMMA, which were implanted into the graphene instead of B and N. The PMMA residues are then transferred to the graphene. As already explained and simulated in chapter 8.1.4 on the water film on the sample, a layer of impurity atoms has a great potential to completely interfere with the implantation and to generate many recoils. Therefore, especially in this energy range, it is possible that both the B and N did not have sufficient energy to penetrate the PMMA and be implanted into the graphene. The samples used for the pure B implantation to investigate the lateral controlled doping were from the same company, but from different batches, so there may have been less contamination. A possible solution here would again be implantation at elevated temperatures to clean the sample before implantation at approximately 200°C. Even if higher temperatures would increase the cleaning and annealing of the graphene, ADONIS is incapable to further raise the samples temperatures.

Finally, it must be mentioned that the transition region between p and n is still too wide and thus prevents the formation of a pn-junction. Again a higher deflection voltage was used (400 V vs. 300 V) and a transition area of less than 0.5 mm can be expected according to the previous experiments (see ch. 9.4). However, this could still be significantly too large. This would also explain the behavior of the current voltage characteristics but not the lack of a transition region in the surface potential. In order to reduce the transition region significantly, higher deflection voltages should be used again and the shielding electrode should be reworked. This should be as close as possible to the sample and also as thin as possible, so that no stray fields occur at the edge.

10 Conclusion and Outlook

In this thesis, the possibilities of Ultra-Low Energy (ULE) ion implantation were expanded by developing both a new ion source for the accelerator and an advanced deceleration unit. This innovation increased the options for available elements and enabled lateral selective implantation. Moreover, ULE ion implantation was utilized to introduce foreign atoms into graphene, followed by investigating the resultant damage to the material after implantation.
The main findings can be summarized as follows:

Ion source A new sputter ion source, based on the Hot Filament Hollow Cathode Ion Source (SO-55 from High Voltage Engineering), extended the range of available ions. Elements such as Li, S, V, Fe, Co, Cu, Nb, Mo, Ag, Sn, Te, and Gd were added to the already possible ones. This source allowed the provision of elements with high melting points and low vapor pressures as an ion beam, as demonstrated by testing Mo (melting point: 2617°C). Through simulations of ion trajectories and comparison with experimental data, it was confirmed that the source indeed released portions of Mo through sputtering, which were subsequently ionized in the plasma. The provided ions were unequivocally confirmed through test implantations and PIXE, RBS, and Auger measurements. Since the source is based on a commercially available model, it can be incorporated into other setups beyond the accelerator in Göttingen.
In the future, additional elements will be tested on the source to further expand the range of available ions. Currently, Zn, Zr, Ta, Ce, and Nd are in the testing phase, with Nd being a particularly promising candidate due to its magnetic properties for influencing 2D materials' magnetic characteristics. Additional planned and partially conducted implantations include incorporating Gd into graphene and implanting V into MoS_2.

Deceleration unit The newly developed deceleration unit, with its enhanced contact for selective implantation, was successfully tested to generate both an energy and a fluence gradient. It allows for applying a voltage gradient across a graphene sample, facilitating implantation at different energies across various surface points. Moreover, by employing electrical masks, one area of the sample can be implanted while keeping another pristine.

Process control A new process control method enabled the use of an Arduino for implantation control, allowing for unattended operation. Additionally, layer growth with ADONIS is now possible without needing manual mass switches between layers. Although such functions were previously possible, the failure of the old control system necessitated the development of a new one. The new system relies on an Arduino, directly communicating with power supplies and the current integrator, eliminating the need for a complex switching box. This simplifies maintenance through the new system.

Simulations Ion implantation simulations have become more realistic with the new program IMINTDYN, as it can now simulate vacancies rather than merely incrementing a vacancy counter. This enhancement improves simulations of graphene and other 2D materials by allowing for the definition of a pseudo-crystalline structure. The ion simulations now provide more accurate insights into ion implantation, enabling more realistic predictions.

Implantations The conducted ion implantations provided insights into damage formation in graphene following ion implantation. For instance, during implantation with noble gases, bubbles can form beneath the graphene, storing gases under high pressure. The conditions for healing graphene after Mn implantation were investigated, as well as the breaking of C-C bonds during implantation. Additionally, an attempt was made to create a p-n junction through selective implantation, but it was not successful. Possible reasons are outlined in Chapter 9.6. Further experiments could involve elevated temperatures for cleaning graphene before implantation and initiating healing processes during implantation. Moreover, additional studies on the sharpness of the transition region between implanted and unimplanted areas should be conducted to optimize its sharpness. Experimenting with different fluences could also be explored to more strongly influence doping. Better measurement and control of electrostatic shadowing should be pursued to achieve the goal of implanting both the n and p regions only once, minimizing material damage from double implantation on one side.

In conclusion, ULE ion implantation holds significant potential for tailoring the properties of 2D materials according to desired specifications. As a result, it can emerge as a technique of great importance for research in this field.
The primary focus for advancing ULE ion implantation in the future should involve scaling up the process to enable the irradiation of entire wafers, making it a compelling option for industrial applications. This technology holds the potential for the integration of doped graphene into various technologies, including but not limited to solar cells, fuel cells, catalysts for water

electrolysis, electrode materials in batteries, environmental toxin sensors, and graphene-based transistors in microelectronics. What sets ULE ion implantation apart from other methods is its ability to directly implant graphene without requiring additional steps like transfers or interference with graphene growth, which could introduce contaminants. Additionally, ULE ion implantation offers precise control over the quantity of foreign atoms to be implanted, and it can accommodate a wide range of elements from the periodic table, provided the appropriate ion source is chosen.

Bibliography

[1] Q. Shangguan, Z. Chen, H. Yang, S. Cheng, W. Yang, Z. Yi, X. Wu, S. Wang, Y. Yi, and P. Wu, Sensors **22** (2022), 10.3390/s22176483.

[2] Q. Shangguan, Y. Zhao, Z. Song, J. Wang, H. Yang, J. Chen, C. Liu, S. Cheng, W. Yang, and Z. Yi, Diamond and Related Materials **128**, 109273 (2022).

[3] G. Dastgeer, Z. M. Shahzad, H. Chae, Y. H. Kim, B. M. Ko, and J. Eom, Advanced Functional Materials **32**, 2204781 (2022).

[4] Z. Zhang, R. Cai, F. Long, and J. Wang, Talanta **134**, 435 (2015).

[5] G. Dastgeer, A. M. Afzal, S. H. A. Jaffery, M. Imran, M. A. Assiri, and S. Nisar, Journal of Alloys and Compounds **919**, 165815 (2022).

[6] Z. Cheng, J. Liao, B. He, F. Zhang, F. Zhang, X. Huang, and L. Zhou, ACS Sustainable Chemistry & Engineering **3**, 1677 (2015).

[7] R. Kumar, S. Sahoo, E. Joanni, R. K. Singh, K. Maegawa, W. K. Tan, G. Kawamura, K. K. Kar, and A. Matsuda, Materials Today **39**, 47 (2020).

[8] R. Faccio, L. FernÃ¡ndez-Werner, H. Pardo, C. Goyenola, O. N. Ventura, and Ã. W. MombrÃº, The Journal of Physical Chemistry C **114**, 18961 (2010).

[9] B. Bhattacharya and U. Sarkar, The Journal of Physical Chemistry C **120**, 26793 (2016).

[10] U. Bangert, W. Pierce, D. M. Kepaptsoglou, Q. Ramasse, R. Zan, M. H. Gass, J. A. Van den Berg, C. B. Boothroyd, J. Amani, and H. Hofsäss, Nano Letters **13**, 4902 (2013).

[11] B. Guo, Q. Liu, E. Chen, H. Zhu, L. Fang, and J. R. Gong, Nano Letters **10**, 4975 (2010).

[12] T. O. Wehling, K. S. Novoselov, S. V. Morozov, E. E. Vdovin, M. I. Katsnelson, A. K. Geim, and A. I. Lichtenstein, Nano Letters **8**, 173 (2008).

[13] E. Åhlgren, J. Kotakoski, and A. Krasheninnikov, Physical Review B, Condensed Matter and Materials Physics **83**, 115424 (2011).

[14] S. Prucnal, A. Hashemi, M. Ghorbani-Asl, R. Hübner, J. Duan, Y. Wei, D. Sharma, D. R. T. Zahn, R. Ziegenrücker, U. Kentsch, A. V. Krasheninnikov, M. Helm, and S. Zhou, Nanoscale **13**, 5834 (2021).

[15] M. Petrović, I. ˇ Srut Rakić, and S. e. a. Runte, Nature Communications **4**, 2772 (2013).

[16] D. Kepaptsoglou, T. P. Hardcastle, C. R. Seabourne, U. Bangert, R. Zan, J. A. Amani, H. Hofsäss, R. J. Nicholls, R. M. D. Brydson, A. J. Scott, and Q. M. Ramasse, ACS Nano **9**, 11398 (2015).

[17] P. Willke, J. A. Amani, A. Sinterhauf, S. Thakur, T. Kotzott, T. Druga, S. Weikert, K. Maiti, H. Hofsäss, and M. Wenderoth, Nano Letters **15**, 5110 (2015).

[18] P.-C. Lin, R. Villarreal, S. Achilli, H. Bana, M. N. Nair, A. Tejeda, K. Verguts, S. De Gendt, M. Auge, H. Hofsäss, S. De Feyter, G. Di Santo, L. Petaccia, S. Brems, G. Fratesi, and L. M. C. Pereira, ACS Nano **15**, 5449 (2021).

[19] M. N. Bui, S. Rost, M. Auge, J.-S. Tu, L. Zhou, I. Aguilera, S. Blügel, M. Ghorbani-Asl, A. V. Krasheninnikov, A. Hashemi, H.-P. Komsa, L. Jin, L. Kibkalo, E. N. O'Connell, Q. M. Ramasse, U. Bangert, H. C. Hofsäss, D. Grützmacher, and B. E. Kardynal, npj 2D Materials and Applications **6** (2022), 10.1038/s41699-022-00318-4.

[20] P.-C. Lin, R. Villarreal, H. Bana, Z. Zarkua, V. Hendriks, H.-C. Tsai, M. Auge, F. Junge, H. Hofsäss, E. Tosi, P. Lacovig, S. Lizzit, W. Zhao, G. Di Santo, L. Petaccia, S. De Feyter, S. De Gendt, S. Brems, and L. M. C. Pereira, The Journal of Physical Chemistry C **126**, 10494 (2022).

[21] R. Villarreal, P.-C. Lin, Z. Zarkua, H. Bana, H.-C. Tsai, M. Auge, F. Junge, H. Hofsäss, E. Tosi, S. De Feyter, S. De Gendt, S. Brems, E. H. Åhlgren, and L. M. Pereira, Carbon **203**, 590 (2023).

[22] M. Auge, *Modification of monolayer-thick semiconductors by ultra-low energy ion implantation*, Phd thesis, Georg-August-Universität Göttingen (2022).

[23] P.-C. Lin, *Ultra-low energy ion implantation of graphene: substitutional and intercalated atoms*, Phd thesis, KU Leuven (2021).

[24] F. Junge, M. Auge, and H. Hofsäss, Nuclear Instruments and Methods in Physics Research Section B: Beam Interactions with Materials and Atoms **510**, 63 (2022).

[25] M. Auge, F. Junge, and H. Hofsäss, Nuclear Instruments and Methods in Physics Research Section B: Beam Interactions with Materials and Atoms **512**, 96 (2022).

[26] H. Hofsäss, F. Junge, P. Kirscht, and K. van Stiphout, Materials Research Express **10**, 075003 (2023).

[27] S. R. E. W. D. R. S. K. v. T. U. B. G. Mutzke, A., "Sdtrimsp version 6.00, ipp 2019-02," Tech. Rep. (MPI for Plasma Physics, 2019).

[28] R. Villarreal, P.-C. Lin, F. Faraji, N. Hassani, H. Bana, Z. Zarkua, M. N. Nair, H.-C. Tsai, M. Auge, F. Junge, H. C. Hofsaess, S. De Gendt, S. De Feyter, S. Brems, E. H. Åhlgren, E. C. Neyts, L. Covaci, F. M. Peeters, M. Neek-Amal, and L. M. C. Pereira, Nano Letters **21**, 8103 (2021).

[29] F. Junge, M. Auge, Z. Zarkua, and H. Hofsäss, Nanomaterials **13** (2023), 10.3390/nano13040658.

[30] P. R. Wallace, Phys. Rev. **71**, 622 (1947).

[31] K. S. Novoselov, A. K. Geim, S. V. Morozov, D. Jiang, Y. Zhang, S. V. Dubonos, I. V. Grigorieva, and A. A. Firsov, Science **306**, 666 (2004).

[32] M. Sharon, M. Sharon, H. Shinohara, and A. Tiwari, *Graphene: An Introduction to the Fundamentals and Industrial Applications*, Advanced Material Series (Wiley, 2015).

[33] A. H. Castro Neto, F. Guinea, N. M. R. Peres, K. S. Novoselov, and A. K. Geim, Rev. Mod. Phys. **81**, 109 (2009).

[34] G. Giovannetti, P. A. Khomyakov, G. Brocks, V. M. Karpan, J. van den Brink, and P. J. Kelly, Phys. Rev. Lett. **101**, 026803 (2008).

[35] G. W. Semenoff, Phys. Rev. Lett. **53**, 2449 (1984).

[36] N. M. R. Peres, F. Guinea, and A. H. Castro Neto, Phys. Rev. B **73**, 125411 (2006).

[37] A. Reina, X. Jia, J. Ho, D. Nezich, H. Son, V. Bulovic, M. S. Dresselhaus, and J. Kong, Nano Letters **9**, 30 (2009).

[38] X. Li, W. Cai, J. An, S. Kim, J. Nah, D. Yang, R. Piner, A. Velamakanni, I. Jung, E. Tutuc, S. K. Banerjee, L. Colombo, and R. S. Ruoff, Science **324**, 1312 (2009).

[39] B. Deng, Z. Liu, and H. Peng, Advanced Materials **31**, 1800996 (2019).

[40] C. Soldano, A. Mahmood, and E. Dujardin, Carbon **48**, 2127 (2010).

[41] S. Ullah, X. Yang, H. Q. Ta, M. Hasan, A. Bachmatiuk, K. Tokarska, B. Trzebicka, L. Fu, and M. H. Rummeli, Nano Research **14**, 3756 (2021).

[42] Y. Zhang, J. P. Small, W. V. Pontius, and P. Kim, Applied Physics Letters **86**, 073104 (2005).

[43] M. Ishigami, J. H. Chen, W. G. Cullen, M. S. Fuhrer, and E. D. Williams, Nano Letters **7**, 1643 (2007).

[44] J. Moser, A. Barreiro, and A. Bachtold, Applied Physics Letters **91**, 163513 (2007).

[45] P. R. Somani, S. P. Somani, and M. Umeno, Chemical Physics Letters **430**, 56 (2006).

[46] K. Verguts, Y. Defossez, A. Leonhardt, J. D. Messemaeker, K. Schouteden, C. V. Haesendonck, C. Huyghebaert, S. D. Gendt, and S. Brems, ECS Journal of Solid State Science and Technology **7**, M195 (2018).

[47] G. R. Yazdi, T. Iakimov, and R. Yakimova, Crystals **6** (2016), 10.3390/cryst6050053.

[48] T. Susi, T. P. Hardcastle, H. HofsÃ¤ss, A. Mittelberger, T. J. Pennycook, C. Mangler, R. Drummond-Brydson, A. J. Scott, J. C. Meyer, and J. Kotakoski, 2D Materials **4**, 021013 (2017).

[49] A. Pramanik, S. Thakur, B. Singh, P. Willke, M. Wenderoth, H. Hofsäss, G. Di Santo, L. Petaccia, and K. Maiti, Phys. Rev. Lett. **128**, 166401 (2022).

[50] L. Lin, L. Liao, J. Yin, H. Peng, and Z. Liu, Nano Today **10**, 701 (2015).

[51] M. Freitag, T. Low, and P. Avouris, Nano Letters **13**, 1644 (2013).

[52] R. A. Nistor, D. M. Newns, and G. J. Martyna, ACS Nano **5**, 3096 (2011).

[53] Y.-C. Lin, C.-Y. Lin, and P.-W. Chiu, Applied Physics Letters **96**, 133110 (2010).

[54] H. M. Jeong, J. W. Lee, W. H. Shin, Y. J. Choi, H. J. Shin, J. K. Kang, and J. W. Choi, Nano Letters **11**, 2472 (2011).

[55] C. Zhang, L. Fu, N. Liu, M. Liu, Y. Wang, and Z. Liu, Advanced Materials **23**, 1020 (2011).

[56] H. Wang, T. Maiyalagan, and X. Wang, ACS Catalysis **2**, 781 (2012).

[57] D. Wei, Y. Liu, Y. Wang, H. Zhang, L. Huang, and G. Yu, Nano Letters **9**, 1752 (2009).

[58] G. Wang, M. Zhang, D. Chen, Q. Guo, X. Feng, T. Niu, X. Liu, A. Li, J. Lai, D. Sun, Z. Liao, Y. Wang, P. K. Chu, G. Ding, X. Xie, Z. Di, and X. Wang, Nature Communications (2018).

[59] M. Nastasi, J. Mayer, and J. Hirvonen, *Ion-Solid Interactions: Fundamentals and Applications*, Cambridge Solid State Science Series (Cambridge University Press, 1996).

[60] W. Eckstein, *Computer Simulation of Ion-Solid Interactions*, Springer Series in Materials Science (Springer Berlin Heidelberg, 2013).

[61] P. van der Heide, *Secondary Ion Mass Spectrometry: An Introduction to Principles and Practices* (Wiley, 2014).

[62] R. Behrisch, *Sputtering by Particle Bombardment I: Physical Sputtering of Single-Element Solids*, Topics in Applied Physics (Springer Berlin Heidelberg, 2014).

[63] R. Behrisch, *Sputtering by Particle Bombardment II: Sputtering of Alloys and Compounds, Electron and Neutron Sputtering, Surface Topography*, Topics in Applied Physics (Springer Berlin Heidelberg, 2014).

[64] R. Behrisch, R. Behrisch, K. Wittmaack, W. Hauffe, W. Hofer, N. Laegreid, E. McClanahan, B. Sundqvist, K. Wittmaack, and M. Yu, *Sputtering by Particle Bombardment III: Characteristics of Sputtered Particles, Technical Applications*, Topics in Applied Physics (Springer Berlin Heidelberg, 2014).

[65] N. Soppera, E. Dupont, M. Bossant, and O. Cabellos, "Janis book of proton-induced cross-sections comparison of evaluated and experimental data from endf/b-vii.1, jendl/he-2007, padf-2007, tendl-2015 and exfor," (2017), oECD NEA Data Bank.

[66] IAEA, "Ion beam analysis nuclear data library (ibandl)," .

[67] A. C. e. W. K. Chu (auth.), J. P. Thomas, *Material Characterization Using Ion Beams*, 1st ed., NATO Advanced Study Institutes Series 28 (Springer US, 1978).

[68] S. A. Johansson, Endeavour **13**, 48 (1989).

[69] M. Toulemonde, E. Paumier, and C. Dufour, Radiation Effects and Defects in Solids **126**, 201 (1993).

[70] J. F. Ziegler, M. Ziegler, and J. Biersack, Nuclear Instruments and Methods in Physics Research Section B: Beam Interactions with Materials and Atoms **268**, 1818 (2010).

[71] R. Gross and A. Marx, *Festkörperphysik* (Oldenbourg Wissenschaftsverlag, 2012).

[72] H. R. Verma, *Atomic and Nuclear Analytical Methods: XRF, Mössbauer, XPS, NAA and Ion-Beam Spectroscopic Techniques*, 1st ed. (Springer, 2007).

[73] W. D. Wilson, L. G. Haggmark, and J. P. Biersack, Phys. Rev. B **15**, 2458 (1977).

[74] L. Landau and E. Lifshitz, *Mechanics: Volume 1*, Bd. 1 (Elsevier Science, 1982).

[75] G. Schatz, A. Weidinger, and M. Deicher, *Nukleare Festkörperphysik: Kernphysikalische Messmethoden und ihre Anwendungen*, Teubner Studienbücher Physik (Vieweg+Teubner Verlag, 2010).

[76] M. Nastasi, J. Mayer, and Y. Wang, *Ion Beam Analysis: Fundamentals and Applications* (CRC Press, 2019).

[77] A. V. Krasheninnikov, F. Banhart, J. X. Li, A. S. Foster, and R. M. Nieminen, Phys. Rev. B **72**, 125428 (2005).

[78] D. Oxtoby, H. Gillis, and L. Butler, *Principles of Modern Chemistry* (Cengage Learning, 2016).

[79] F. Neufingerl, *Chemie: Allgemeine und anorganische Chemie. 1*, Chemie (Jugend & Volk, 2006).

[80] J. Hopster, R. Kozubek, B. Ban-d'Etat, S. Guillous, H. Lebius, and M. Schleberger, 2D Materials **1**, 011011 (2014).

[81] A. Merrill, C. D. Cress, J. E. Rossi, N. D. Cox, and B. J. Landi, Phys. Rev. B **92**, 075404 (2015).

[82] F. Banhart, J. X. Li, and A. V. Krasheninnikov, Phys. Rev. B **71**, 241408 (2005).

[83] J. Kotakoski, C. H. Jin, O. Lehtinen, K. Suenaga, and A. V. Krasheninnikov, Phys. Rev. B **82**, 113404 (2010).

[84] J. Kotakoski, D. Santos-Cottin, and A. V. Krasheninnikov, ACS Nano **6**, 671 (2012).

[85] O. Lehtinen, J. Kotakoski, A. V. Krasheninnikov, A. Tolvanen, K. Nordlund, and J. Keinonen, Phys. Rev. B **81**, 153401 (2010).

[86] A. Zobelli, A. Gloter, C. P. Ewels, G. Seifert, and C. Colliex, Phys. Rev. B **75**, 245402 (2007).

[87] A. P. Thompson, H. M. Aktulga, R. Berger, D. S. Bolintineanu, W. M. Brown, P. S. Crozier, P. J. in 't Veld, A. Kohlmeyer, S. G. Moore, T. D. Nguyen, R. Shan, M. J. Stevens, J. Tranchida, C. Trott, and S. J. Plimpton, Comp. Phys. Comm. **271**, 108171 (2022).

[88] J. C. Meyer, F. Eder, S. Kurasch, V. Skakalova, J. Kotakoski, H. J. Park, S. Roth, A. Chuvilin, S. Eyhusen, G. Benner, A. V. Krasheninnikov, and U. Kaiser, Phys. Rev. Lett. **108**, 196102 (2012).

[89] R. Egerton, R. McLeod, F. Wang, and M. Malac, Ultramicroscopy **110**, 991 (2010).

[90] F. Banhart, Reports on Progress in Physics **62**, 1181 (1999).

[91] T. Susi, C. Hofer, G. Argentero, G. T. Leuthner, T. J. Pennycook, C. Mangler, J. C. Meyer, and J. Kotakoski, Nature Communications **7**, 13040 (2016).

[92] K. Nakai, C. Kinoshita, and A. Matsunaga, Ultramicroscopy **39**, 361 (1991).

[93] J. Roth, J. Bohdansky, and W. Ottenberger, Journal of Nuclear Materials **165**, 193 (1989).

[94] I. Fayazov, E. Mashkova, V. Molchanov, A. Sidorov, A. Tolmachev, and W. Eckstein, Nuclear Instruments and Methods in Physics Research Section B: Beam Interactions with Materials and Atoms **67**, 523 (1992).

[95] V. O. Özçelik, H. H. Gurel, and S. Ciraci, Phys. Rev. B **88**, 045440 (2013).

[96] W. Buaprasert, B. Kaewkham-ai, and K. Uthaichana, in *2020 17th International Conference on Electrical Engineering/Electronics, Computer, Telecommunications and Information Technology (ECTI-CON)* (2020) pp. 447–451.

[97] L. N. Large and R. W. Bicknell, Journal of Materials Science **2**, 589 (1967).

[98] M. I. Current, AIP Conference Proceedings **2160**, 020001 (2019).

[99] D. Chattopadhyay, *Electronics (fundamentals And Applications)* (New Age International (P) Limited, 2006).

[100] J. Gordon, D. Armour, S. Donnelly, J. van den Berg, D. Marton, and J. Rabalais, Nuclear Instruments and Methods in Physics Research Section B: Beam Interactions with Materials and Atoms **59-60**, 312 (1991).

[101] Colutron low energy ion beam system, https://beamimaging.com/product/model-450-decelerator/ last visited 06.09.2023.

[102] W. Demtröder, *Experimentalphysik 3 Atome, Moleküle und Festkörper*, 4th ed. (Springer Verlag, 2010).

[103] D. A.J.Garratt-Reed, *Energy-Dispersive X-Ray Analysis in the Electron Microscope* (Garland Science, New York, 2003).

[104] M. H. Kabir, *Particle Induced X-ray Emission (PIXE) Setup and Quantitative Elemental Analysis*, Dissertation, Kochi University of Technology (2007).

[105] F. Junge, P. Kirscht, and H. Hofsäss, Nuclear Instruments and Methods in Physics Research Section B: Beam Interactions with Materials and Atoms **517**, 16 (2022).

[106] M. Uhrmacher and H. Hofsäss, Nuclear Instruments and Methods in Physics Research Section B: Beam Interactions with Materials and Atoms **240**, 48 (2005), accelerators in Applied Research and Technology.

[107] C. Borschel, M. Schnell, C. Ronning, and H. Hofsäss, Nuclear Instruments and Methods in Physics Research Section B: Beam Interactions with Materials and Atoms **267**, 1737 (2009), proceedings of the 16th International Conference on Ion Beam Modification of Materials.

[108] N. de la Rosa, P. Kristiansson, E. Nilsson, L. Ros, J. Pallon, and H. Skogby, Journal of Radioanalytical Chemistry **317**, 253 (2018).

[109] S. Hofmann, *Auger- and X-Ray Photoelectron Spectroscopy in Materials Science: A User-Oriented Guide*, Springer Series in Surface Sciences (Springer Berlin Heidelberg, 2012).

[110] Https://rbdinstruments.com/phi/system-upgrades.html accessed on 14.08.2023.

[111] K. Childs and C. Hedberg, *Handbook of Auger Electron Spectroscopy: A Book of Reference Data for Identification and Interpretation in Auger Electron Spectroscopy* (Physical Electronics, 1995).

[112] I. Lewis and H. Edwards, *Handbook of Raman Spectroscopy: From the Research Laboratory to the Process Line*, Practical Spectroscopy (CRC Press, 2001).

[113] A. C. Ferrari and J. Robertson, Phys. Rev. B **61**, 14095 (2000).

[114] J.-B. Wu, M.-L. Lin, X. Cong, H.-N. Liu, and P.-H. Tan, Chem. Soc. Rev. **47**, 1822 (2018).

[115] C. Cress, S. Schmucker, A. Friedman, P. Dev, J. Culbertson, J. Lyding, and J. Robinson, ACS Nano **10**, 3714 (2016).

[116] A. C. Ferrari, Solid State Communications **143**, 47 (2007).

[117] M. Lucchese, F. Stavale, E. M. Ferreira, C. Vilani, M. Moutinho, R. B. Capaz, C. Achete, and A. Jorio, Carbon **48**, 1592 (2010).

[118] L. G. Cançado, A. Jorio, E. H. M. Ferreira, F. Stavale, C. A. Achete, R. B. Capaz, M. V. O. Moutinho, A. Lombardo, T. S. Kulmala, and A. C. Ferrari, Nano Letters **11**, 3190 (2011).

[119] J. B. Pendry, "Low-energy electron diffraction," in *Interaction of Atoms and Molecules with Solid Surfaces*, edited by V. Bortolani, N. H. March, and M. P. Tosi (Springer US, Boston, MA, 1990) pp. 201–211.

[120] W. Zhang, *Photoemission Spectroscopy on High Temperature Superconductor: A Study of Bi2Sr2CaCu2O8 by Laser-Based Angle-Resolved Photoemission*, Springer Theses (Springer Berlin Heidelberg, 2012).

[121] K. Wandelt, *Encyclopedia of Interfacial Chemistry: Surface Science and Electrochemistry* (Elsevier Science, 2018).

[122] S. Sadewasser and T. Glatzel, *Kelvin Probe Force Microscopy: Measuring and Compensating Electrostatic Forces*, Springer Series in Surface Sciences (Springer Berlin Heidelberg, 2011).

[123] H. Hofsäss and A. Stegmaier, Nuclear Instruments and Methods in Physics Research Section B: Beam Interactions with Materials and Atoms **517**, 49 (2022).

[124] P. Sigmund, Phys. Rev. **187**, 768 (1969).

[125] M. Mayer, SIMNRA User's Guide , Report IPP 9/113, Max-Planck-Institut für Plasmaphysik, Garching, Germany, 1997.

[126] A. Gurbich, Nuclear Instruments and Methods in Physics Research Section B: Beam Interactions with Materials and Atoms **371**, 27 (2016).

[127] J. L. Campbell, "Gupix," (2009), http://pixe.physics.uoguelph.ca/gupix/about/.

[128] D. Manura and D. Dahl, *Simion 8.1 users manual (adaptas solutions, llc, palmer, ma 01069)* (2008).

[129] G. Sidenius, Nuclear Instruments and Methods **151**, 349 (1978).

[130] H. Hofsäss, H. Binder, T. Klumpp, and E. Recknagel, Diamond and Related Materials **3**, 137 (1994).

[131] C. F. Barnett, P. M. Stier, and G. E. Evans, Review of Scientific Instruments **24**, 394 (1953).

[132] A. Rohatgi, "Webplotdigitizer: Version 4.6," (2022).

[133] D. Lide, *CRC Handbook of Chemistry and Physics, 84th Edition* (Taylor & Francis, 2003).

[134] Https://www.arduino.cc/reference/en/language/functions/communication/wire/ accessed on 15.08.2023.

[135] Https://www.arduino.cc/reference/en/libraries/liquidcrystal-i2c/ accessed on 15.08.2023.

[136] Moeller W. and Posselt M., 2001, ,TRIDYN-FZR User Manual, Forschungszentrum Rossendorf (FZR) 317 1-20.

[137] T. Yoon, W. C. Shin, T. Y. Kim, J. H. Mun, T.-S. Kim, and B. J. Cho, Nano Letters **12**, 1448 (2012).

[138] J. Torres, Y. Zhu, P. Liu, S. C. Lim, and M. Yun, physica status solidi (a) **215**, 1700512 (2018).

[139] M. Shahzadi, S. Nisar, D.-K. Kim, N. Sarwar, A. Rasheed, W. Ahmad, A. M. Afzal, M. Imran, M. A. Assiri, Z. M. Shahzad, and G. Dastgeer, Chemosensors **11** (2023), 10.3390/chemosensors11020083.

[140] S. Hang, Z. Moktadir, and H. Mizuta, Carbon **72**, 233 (2014).

[141] Y. Xu, K. Zhang, C. Brüsewitz, X. Wu, and H. C. Hofsäss, AIP Advances **3**, 072120 (2013).

Appendix

Arduino Code

```
""///// Author: Felix Junge //////

#include <Wire.h>
#include <LiquidCrystal_I2C.h>
#include <Keypad.h>



////////////////////////////////////////////Keypad/////////////////////////////////
int i=0;

const byte Rows= 4;
const byte Cols= 4;

char keymap[Rows][Cols]= {
{'1', '2', '3', 'A'},
{'4', '5', '6', 'B'},
{'7', '8', '9', 'C'},
{'*', '0', '#', 'D'}
};

byte rowPins[Rows] = {46,47,48,49}; //Rows 0 to 3    Keypad 8 -> pin 46, 7 -> 47 etc ..... 1-> 53
byte colPins[Cols]= {50,51,52,53}; //Columns 0 to 3

Keypad keypad= Keypad(makeKeymap(keymap), rowPins, colPins, Rows, Cols);

///////////////////////////////LCD Display/////////////////////////////////////

LiquidCrystal_I2C lcd(0x27, 16, 2); // LCD connected to SDA, SDL, 5V and Ground


/////////////////////////////////// Def. Variables //////////////////////////////////////////

int CurrentIntPulse = 3;  // Pin 3 to Current integrator Pulse
int BeamDefl = 25; // Pin 25 to  Beam Deflector
int Pin_regime = 27;  // Pin for current regime at current integrator
int Element1 = 29; // Pin for Magnet element 1
```

```
int Element2 = 31; // Pin for Magnet element 2



///Times for binär signal to current int.//////
int long_high = 300;
int short_high = 150;
int short_down = 350;
int long_down = 500;


long count;
double count2;
long fluence;
long fluence1;
long fluence2;
long timer_start;
long timer_stop;
float timer;
float charge;
double finish_count; // Where to stop the implantation
float current_regime;
int regime;


String InputRegime; // String for Current Regime
String InputCode; // String for Keypad password
String InputFluence; // String for Keypad input number for Fluence
String InputFluence2; // String for Keypad input number for Fluence
int u, j, k, code, p, o, t, g, oldstate, d; // Variable for while loop for keypad read
//boolean Pulse // for counter
//////////////////////////////////////Setup/////////////////////////////////////////////

void setup() {
// put your setup code here, to run once:

Serial.begin(9600); // USB output
pinMode(CurrentIntPulse, INPUT);
attachInterrupt(digitalPinToInterrupt(CurrentIntPulse), count_pulse, RISING); // Current
    integrator Pulse Rising counts signal from low to high
pinMode(BeamDefl, OUTPUT);// Beam Defelector output mode
pinMode(Element1, OUTPUT);
pinMode(Element2, OUTPUT);
pinMode(Pin_regime,OUTPUT);
//  pinMode(counter1, INPUT);


InputFluence.reserve(6); // Maximum number of Fluence digits is 6
InputCode.reserve(4); // Maximum number of Code digits is 4
InputRegime.reserve(6); // Maximum number of Code digits is 6

lcd.init(); // LCD start
lcd.noBacklight();
```

```
digitalWrite(BeamDefl, HIGH); // Turn on Beam Defl.

}



/////////////////////////////////////////Main////////////////////////////////////////////////////////////////////

void loop() {
// put your main code here, to run repeatedly:
//////////////////////////////////////// Program start////////////////////////////////
keypad.waitForKey(); // Wait for Numpad key to start program
lcd.backlight();
digitalWrite(BeamDefl, HIGH); // Turn on Beam Defl.
lcd.clear();
lcd.setCursor(0,0); // Text at top left corner
lcd.print("Start");
keypad.waitForKey();


////////////////////////////////Program reset////////////////////////////////////////////////

digitalWrite(BeamDefl, HIGH); // Turn on Beam defelctor

regime=0;
current_regime=0;
finish_count=0; // Reset all values
charge=0; // Reset all values
fluence=0; // Reset all values
fluence2=0; //Reset all values
count=0;
count2=0;// Reset all values
u=0; // Reset all values
j=0; // Reset all values
p=0;
o=0;
g=0;
t=0;
d=1;
oldstate=0;
//  Pulse=LOW;





////////////////////////////////Select Programm////////////////////////////////////////////////


char select_program = 0;
```

```
lcd.clear();
lcd.setCursor(0,0);
lcd.print("Implantation: 1");
lcd.setCursor(0,1);
lcd.print("Switch Beam: 2");

select_program = keypad.waitForKey();  //Select Programtype
if(select_program == ’1’) {
lcd.setCursor(0,0);
StandartImp();
}
if(select_program == ’2’) {
lcd.setCursor(0,0);
SwitchBeam();
}


////////////////////End Implantation set to stand by///////////////////////

keypad.waitForKey();
// digitalWrite(BeamDefl, LOW);
// digitalWrite(35,LOW);
lcd.clear();
lcd.noBacklight();

}

/////////////////////////Funktion for counting/////////////////

void count_pulse(){
count++;
count2++;
}

////////////////////////////// Standart Implantation //////////////
void StandartImp(){
lcd.clear();
lcd.setCursor(0,0); // Text at top left corner
lcd.print("Fluence [1e12]:");

while (u!=1){

char key_fluence = keypad.waitForKey();

if (key_fluence) {  //Test Keypad input
Serial.println(key_fluence);
lcd.setCursor(0,0); // Text at top left corner
lcd.print("Fluence [1e12]");
lcd.setCursor(j,1); // second row
lcd.print(key_fluence);
j++;    // Set Cursor one step further
}

```

```
if (key_fluence >= '0' && key_fluence <= '9'){
InputFluence += key_fluence;
}
else if (key_fluence == '#'){ // Press # for converting to number
if (InputFluence.length() > 0) {
fluence= InputFluence.toInt(); // Conevrting String to Int to set Fluence
InputFluence = ""; // Clear Input string
u = 1; // Condition to leave the loop
}
}
else if (key_fluence == '*') {
InputFluence = ""; // Clear Input by pressing *
lcd.clear();
lcd.setCursor(0,0);
lcd.print("Fluence [1e12]:");
j=0;
}
}

/////////////////////////////Set LCDDisplay/////////////////////////////////
lcd.clear();
lcd.setCursor(0,0);
lcd.print("Fluence:");
lcd.setCursor(8,0);
lcd.print(fluence);
lcd.setCursor(13,0);
lcd.print("e12");
lcd.setCursor(0,1);
lcd.print("Press any button");
keypad.waitForKey(); //Waiting for key
//  Serial.println(fluence); // Test Serial output

select_regime();  //select current regime
///////////////////////////////////////////////////////Start Implantation /////////////////////////////
charge = fluence*0.4; // Calculate charge

//  Serial.print(charge);

finish_count = 10*charge/(current_regime); // Calculating the needed counts (*10 sind 10 ct are one current regime)

char key_start=keypad.waitForKey(); // Waiting for key to start

timer_start=millis(); // Start of Clock

currentint_regime();

if ((charge > 0) && (key_start)){ // Condition to start Implantation
count=0; // Set count 0 to be sure to start with zero (maybe signals vom CI have arrived during starting by sparks etc.)
digitalWrite(BeamDefl, LOW); // Turn off Beam defl.
lcd.clear();
```

```
lcd.setCursor(0,0);
lcd.print("Counts");
lcd.setCursor(9,1);
lcd.print(finish_count, 0);
lcd.setCursor(8,1);
lcd.print("/");
}

while (count<=finish_count){ // Counting the Fluence loop
//      count();  //counter without interupt
currentint_regime();
lcd.setCursor(0,1);
lcd.print(count);
Serial.println(count);
}

digitalWrite(BeamDefl, HIGH); // Turn on Beam Defl. after Implantation
// digitalWrite(35,HIGH);


timer_stop=millis(); // End Clock
timer=(timer_stop-timer_start)/(60000.0); // Calculate Implantation Time in min

//////////////////////// Print Implantation Time////////////////////////////
lcd.clear();
lcd.setCursor(0,0);
lcd.print("Job done in");
lcd.setCursor(0,1);
lcd.print(timer);
lcd.setCursor(13,1);
lcd.print("min");
}
////////////////////////////////////////////////////////////////////////
//////////////////////////// Switch BEAM ///////////////////////////

void SwitchBeam(){
lcd.clear();
lcd.setCursor(0,0); // Text at top left corner
lcd.print("Fluence 1 [1e15]:");

while (u!=1){

char key_fluence = keypad.waitForKey();

if (key_fluence) {  //Test Keypad input
lcd.setCursor(0,0); // Text at top left corner
lcd.print("Fluence 1 [1e15]");
lcd.setCursor(j,1); // second row
lcd.print(key_fluence);
j++;    // Set Cursor one step further
}

if (key_fluence >= '0' && key_fluence <= '9'){
```

```
InputFluence += key_fluence;
}
else if (key_fluence == '#'){ // Press # for converting to number
if (InputFluence.length() > 0) {
fluence1= InputFluence.toInt(); // Conevrting String to Int to set Fluence
InputFluence = ""; // Clear Input string
u = 1; // Condition to leave the loop
}
}
else if (key_fluence == '*') {
InputFluence = ""; // Clear Input by pressing *
lcd.clear();
lcd.setCursor(0,0);
lcd.print("Fluence [1e15]:");
j=0;
}
}

InputFluence = "";//Reset of String for second Fluence
j=0; //Reset Cursor
lcd.clear();
lcd.setCursor(0,0); // Text at top left corner
lcd.print("Fluence 2 [1e15]:");

while (g!=1){

char key_fluence = keypad.waitForKey();

if (key_fluence) {  //Test Keypad input
//       Serial.println(key_fluence);
lcd.setCursor(0,0); // Text at top left corner
lcd.print("Fluence 2 [1e15]");
lcd.setCursor(j,1); // second row
lcd.print(key_fluence);
j++;    // Set Cursor one step further
}

if (key_fluence >= '0' && key_fluence <= '9'){
InputFluence += key_fluence;
}
else if (key_fluence == '#'){ // Press # for converting to number
if (InputFluence.length() > 0) {
fluence2= InputFluence.toInt(); // Conevrting String to Int to set Fluence
InputFluence = ""; // Clear Input string
g = 1; // Condition to leave the loop
}
}
else if (key_fluence == '*') {
InputFluence = ""; // Clear Input by pressing *
lcd.clear();
lcd.setCursor(0,0);
lcd.print("Fluence [1e15]:");
j=0;
```

```
}
}
////////////////////////////Set LCDDisplay////////////////////////////////
lcd.clear();
lcd.setCursor(0,0);
lcd.print("Fluence1:");
lcd.setCursor(9,0);
lcd.print(fluence1);;
lcd.setCursor(13,0);
lcd.print("e15");
lcd.setCursor(0,1);
lcd.print("Fluence2:");
lcd.setCursor(9,1);
lcd.print(fluence2);
lcd.setCursor(13,1);
lcd.print("e15");
//  lcd.setCursor(0,1);
//  lcd.print("Press#");

//  Serial.println(fluence); // Test Serial output

//////////////////////////////// Bestrahlung ///////////////////////////
select_regime();


float charge1 = fluence1*400.0;
float charge2 = fluence2*400.0;
float charge_tot = charge1+charge2;

long finish_count1 = 10*charge1/(current_regime);
long finish_count2 = 10*charge2/(current_regime);
double finish_count_tot = 10*charge_tot/(current_regime);

float fluence1_1 = fluence1;
float fluence2_2 = fluence2;
float tot_flu = fluence1_1 + fluence2_2;
float ratio12 = fluence1/(tot_flu);
float ratio21 = fluence2/(tot_flu);

double c; //variable for 1e15 or 2e15


if (ratio12 == ratio21){
c = 4000/(current_regime); // 1e15 fluence definition
}
else {
c = 2*4000/(current_regime);  //2e15 fluence definition
}

double Element1_count=c*ratio12;
double Element2_count=c*ratio21;

char key_start=keypad.waitForKey(); // Waiting for key to start
```

```

timer_start=millis(); // Start of Clock

currentint_regime();

if ((charge_tot > 0) && (key_start)){ // Condition to start Implantation
count=0; // Set count 0 to be sure to start with zero (maybe signals vom CI have arrived during starting by sparks etc.)
digitalWrite(BeamDefl, LOW); // Turn off Beam defl.
lcd.clear();
lcd.setCursor(0,0);
lcd.print("Counts");
lcd.setCursor(9,1);
lcd.print(finish_count_tot, 0);
lcd.setCursor(8,1);
lcd.print("/");
}

count2=0;
count=0;
d=1;
while (count<=finish_count_tot){ // Counting the Fluence loop

if (d==1){
digitalWrite(Element1, HIGH);
digitalWrite(Element2, LOW);
while (count2<=Element1_count){
currentint_regime();
lcd.setCursor(0,1);

lcd.print(count);
if(count>=finish_count_tot){
break;
}
}
if (count2>=Element1_count){
d=2;
}
}

count2=0;

if (d==2){
digitalWrite(Element1, LOW);
digitalWrite(Element2, HIGH);
while (count2<=Element2_count){
currentint_regime();
lcd.setCursor(0,1);
lcd.print(count);

if(count>=finish_count_tot){
break;
}
```

```
}
if (count2>=Element2_count){
d=1;
}
}
//d=1;
count2=0;


}

digitalWrite(BeamDefl, HIGH); // Turn on Beam Defl. after Implantation
// digitalWrite(35,HIGH);


timer_stop=millis(); // End Clock
timer=(timer_stop-timer_start)/(60000.0); // Calculate Implantation Time in min

//////////////////////// Print Implantation Time////////////////////////////
lcd.clear();
lcd.setCursor(0,0);
lcd.print("Job done in");
lcd.setCursor(0,1);
lcd.print(timer);
lcd.setCursor(13,1);
lcd.print("min");



}
////////////////////////////////////////////////////////// Send current regime ///////////////////

void currentint_regime(){

digitalWrite(Pin_regime, HIGH);

if (current_regime == 0.001){
delay(6);
digitalWrite(Pin_regime, LOW);
delayMicroseconds(short_down);
digitalWrite(Pin_regime, HIGH);
delayMicroseconds(long_high);
digitalWrite(Pin_regime, LOW);
delayMicroseconds(short_down);
digitalWrite(Pin_regime, HIGH);
delayMicroseconds(short_high);
digitalWrite(Pin_regime, LOW);
delayMicroseconds(long_down);
digitalWrite(Pin_regime, HIGH);
delayMicroseconds(short_high);
digitalWrite(Pin_regime, LOW);
delayMicroseconds(long_down);
```

```
digitalWrite(Pin_regime, HIGH);
delayMicroseconds(short_high);
digitalWrite(Pin_regime, LOW);
delayMicroseconds(long_down);
digitalWrite(Pin_regime, HIGH);
delayMicroseconds(short_high);
digitalWrite(Pin_regime, LOW);
delayMicroseconds(long_down);
digitalWrite(Pin_regime, HIGH);
delayMicroseconds(short_high);
digitalWrite(Pin_regime, LOW);
delayMicroseconds(long_down);
digitalWrite(Pin_regime, HIGH);
delayMicroseconds(short_high);
digitalWrite(Pin_regime, LOW);
delayMicroseconds(long_down);
digitalWrite(Pin_regime, HIGH);
delayMicroseconds(short_high);
digitalWrite(Pin_regime, LOW);
delayMicroseconds(long_down);
digitalWrite(Pin_regime, HIGH);
delay(6);
}


else if (current_regime == 0.003){
delay(6);
digitalWrite(Pin_regime, LOW);
delayMicroseconds(short_down);
digitalWrite(Pin_regime, HIGH);
delayMicroseconds(short_high);
digitalWrite(Pin_regime, LOW);
delayMicroseconds(long_down);
digitalWrite(Pin_regime, HIGH);
delayMicroseconds(long_high);
digitalWrite(Pin_regime, LOW);
delayMicroseconds(short_down);
digitalWrite(Pin_regime, HIGH);
delayMicroseconds(short_high);
digitalWrite(Pin_regime, LOW);
delayMicroseconds(long_down);
digitalWrite(Pin_regime, HIGH);
delayMicroseconds(short_high);
digitalWrite(Pin_regime, LOW);
delayMicroseconds(long_down);
digitalWrite(Pin_regime, HIGH);
delayMicroseconds(short_high);
digitalWrite(Pin_regime, LOW);
delayMicroseconds(long_down);
digitalWrite(Pin_regime, HIGH);
delayMicroseconds(short_high);
digitalWrite(Pin_regime, LOW);
delayMicroseconds(long_down);
```

```
digitalWrite(Pin_regime, HIGH);
delayMicroseconds(short_high);
digitalWrite(Pin_regime, LOW);
delayMicroseconds(long_down);
digitalWrite(Pin_regime, HIGH);
delayMicroseconds(short_high);
digitalWrite(Pin_regime, LOW);
delayMicroseconds(long_down);
digitalWrite(Pin_regime, HIGH);
delay(6);
}
else if (current_regime == 0.01){
delay(6);
digitalWrite(Pin_regime, LOW);
delayMicroseconds(short_down);
digitalWrite(Pin_regime, HIGH);
delayMicroseconds(long_high);
digitalWrite(Pin_regime, LOW);
delayMicroseconds(short_down);
digitalWrite(Pin_regime, HIGH);
delayMicroseconds(long_high);
digitalWrite(Pin_regime, LOW);
delayMicroseconds(short_down);
digitalWrite(Pin_regime, HIGH);
delayMicroseconds(short_high);
digitalWrite(Pin_regime, LOW);
delayMicroseconds(long_down);
digitalWrite(Pin_regime, HIGH);
delayMicroseconds(short_high);
digitalWrite(Pin_regime, LOW);
delayMicroseconds(long_down);
digitalWrite(Pin_regime, HIGH);
delayMicroseconds(short_high);
digitalWrite(Pin_regime, LOW);
delayMicroseconds(long_down);
digitalWrite(Pin_regime, HIGH);
delayMicroseconds(short_high);
digitalWrite(Pin_regime, LOW);
delayMicroseconds(long_down);
digitalWrite(Pin_regime, HIGH);
delayMicroseconds(short_high);
digitalWrite(Pin_regime, LOW);
delayMicroseconds(long_down);
digitalWrite(Pin_regime, HIGH);
delayMicroseconds(short_high);
digitalWrite(Pin_regime, LOW);
delayMicroseconds(long_down);
digitalWrite(Pin_regime, HIGH);
delay(6);
}
else if (current_regime == 0.03){
delay(6);
digitalWrite(Pin_regime, LOW);
```

```
delayMicroseconds(short_down);
digitalWrite(Pin_regime, HIGH);
delayMicroseconds(short_high);
digitalWrite(Pin_regime, LOW);
delayMicroseconds(long_down);
digitalWrite(Pin_regime, HIGH);
delayMicroseconds(short_high);
digitalWrite(Pin_regime, LOW);
delayMicroseconds(long_down);
digitalWrite(Pin_regime, HIGH);
delayMicroseconds(long_high);
digitalWrite(Pin_regime, LOW);
delayMicroseconds(short_down);
digitalWrite(Pin_regime, HIGH);
delayMicroseconds(short_high);
digitalWrite(Pin_regime, LOW);
delayMicroseconds(long_down);
digitalWrite(Pin_regime, HIGH);
delayMicroseconds(short_high);
digitalWrite(Pin_regime, LOW);
delayMicroseconds(long_down);
digitalWrite(Pin_regime, HIGH);
delayMicroseconds(short_high);
digitalWrite(Pin_regime, LOW);
delayMicroseconds(long_down);
digitalWrite(Pin_regime, HIGH);
delayMicroseconds(short_high);
digitalWrite(Pin_regime, LOW);
delayMicroseconds(long_down);
digitalWrite(Pin_regime, HIGH);
delayMicroseconds(short_high);
digitalWrite(Pin_regime, LOW);
delayMicroseconds(long_down);
digitalWrite(Pin_regime, HIGH);
delay(6);
}
else if (current_regime == 0.1){
delay(6);
digitalWrite(Pin_regime, LOW);
delayMicroseconds(short_down);
digitalWrite(Pin_regime, HIGH);
delayMicroseconds(long_high);
digitalWrite(Pin_regime, LOW);
delayMicroseconds(short_down);
digitalWrite(Pin_regime, HIGH);
delayMicroseconds(short_high);
digitalWrite(Pin_regime, LOW);
delayMicroseconds(long_down);
digitalWrite(Pin_regime, HIGH);
delayMicroseconds(long_high);
digitalWrite(Pin_regime, LOW);
delayMicroseconds(short_down);
digitalWrite(Pin_regime, HIGH);
```

```
delayMicroseconds(short_high);
digitalWrite(Pin_regime, LOW);
delayMicroseconds(long_down);
digitalWrite(Pin_regime, HIGH);
delayMicroseconds(short_high);
digitalWrite(Pin_regime, LOW);
delayMicroseconds(long_down);
digitalWrite(Pin_regime, HIGH);
delayMicroseconds(short_high);
digitalWrite(Pin_regime, LOW);
delayMicroseconds(long_down);
digitalWrite(Pin_regime, HIGH);
delayMicroseconds(short_high);
digitalWrite(Pin_regime, LOW);
delayMicroseconds(long_down);
digitalWrite(Pin_regime, HIGH);
delayMicroseconds(short_high);
digitalWrite(Pin_regime, LOW);
delayMicroseconds(long_down);
digitalWrite(Pin_regime, HIGH);
delay(6);
}
else if (current_regime == 0.3){
delay(6);
digitalWrite(Pin_regime, LOW);
delayMicroseconds(short_down);
digitalWrite(Pin_regime, HIGH);
delayMicroseconds(short_high);
digitalWrite(Pin_regime, LOW);
delayMicroseconds(long_down);
digitalWrite(Pin_regime, HIGH);
delayMicroseconds(long_high);
digitalWrite(Pin_regime, LOW);
delayMicroseconds(short_down);
digitalWrite(Pin_regime, HIGH);
delayMicroseconds(long_high);
digitalWrite(Pin_regime, LOW);
delayMicroseconds(short_down);
digitalWrite(Pin_regime, HIGH);
delayMicroseconds(short_high);
digitalWrite(Pin_regime, LOW);
delayMicroseconds(long_down);
digitalWrite(Pin_regime, HIGH);
delayMicroseconds(short_high);
digitalWrite(Pin_regime, LOW);
delayMicroseconds(long_down);
digitalWrite(Pin_regime, HIGH);
delayMicroseconds(short_high);
digitalWrite(Pin_regime, LOW);
delayMicroseconds(long_down);
digitalWrite(Pin_regime, HIGH);
delayMicroseconds(short_high);
digitalWrite(Pin_regime, LOW);
```

```
delayMicroseconds(long_down);
digitalWrite(Pin_regime, HIGH);
delayMicroseconds(short_high);
digitalWrite(Pin_regime, LOW);
delayMicroseconds(long_down);
digitalWrite(Pin_regime, HIGH);
delay(6);
}
else if (current_regime == 1){
delay(6);
digitalWrite(Pin_regime, LOW);
delayMicroseconds(short_down);
digitalWrite(Pin_regime, HIGH);
delayMicroseconds(long_high);
digitalWrite(Pin_regime, LOW);
delayMicroseconds(short_down);
digitalWrite(Pin_regime, HIGH);
delayMicroseconds(long_high);
digitalWrite(Pin_regime, LOW);
delayMicroseconds(short_down);
digitalWrite(Pin_regime, HIGH);
delayMicroseconds(long_high);
digitalWrite(Pin_regime, LOW);
delayMicroseconds(short_down);
digitalWrite(Pin_regime, HIGH);
delayMicroseconds(short_high);
digitalWrite(Pin_regime, LOW);
delayMicroseconds(long_down);
digitalWrite(Pin_regime, HIGH);
delayMicroseconds(short_high);
digitalWrite(Pin_regime, LOW);
delayMicroseconds(long_down);
digitalWrite(Pin_regime, HIGH);
delayMicroseconds(short_high);
digitalWrite(Pin_regime, LOW);
delayMicroseconds(long_down);
digitalWrite(Pin_regime, HIGH);
delayMicroseconds(short_high);
digitalWrite(Pin_regime, LOW);
delayMicroseconds(long_down);
digitalWrite(Pin_regime, HIGH);
delayMicroseconds(short_high);
digitalWrite(Pin_regime, LOW);
delayMicroseconds(long_down);
digitalWrite(Pin_regime, HIGH);
delay(6);
}
else if (current_regime == 3){
delay(6);
digitalWrite(Pin_regime, LOW);
delayMicroseconds(short_down);
digitalWrite(Pin_regime, HIGH);
delayMicroseconds(short_high);
```

```
digitalWrite(Pin_regime, LOW);
delayMicroseconds(long_down);
digitalWrite(Pin_regime, HIGH);
delayMicroseconds(short_high);
digitalWrite(Pin_regime, LOW);
delayMicroseconds(long_down);
digitalWrite(Pin_regime, HIGH);
delayMicroseconds(short_high);
digitalWrite(Pin_regime, LOW);
delayMicroseconds(long_down);
digitalWrite(Pin_regime, HIGH);
delayMicroseconds(long_high);
digitalWrite(Pin_regime, LOW);
delayMicroseconds(short_down);
digitalWrite(Pin_regime, HIGH);
delayMicroseconds(short_high);
digitalWrite(Pin_regime, LOW);
delayMicroseconds(long_down);
digitalWrite(Pin_regime, HIGH);
delayMicroseconds(short_high);
digitalWrite(Pin_regime, LOW);
delayMicroseconds(long_down);
digitalWrite(Pin_regime, HIGH);
delayMicroseconds(short_high);
digitalWrite(Pin_regime, LOW);
delayMicroseconds(long_down);
digitalWrite(Pin_regime, HIGH);
delayMicroseconds(short_high);
digitalWrite(Pin_regime, LOW);
delayMicroseconds(long_down);
digitalWrite(Pin_regime, HIGH);
delay(6);
}
else if (current_regime == 10){


delay(6);
digitalWrite(Pin_regime, LOW);
delayMicroseconds(short_down);
digitalWrite(Pin_regime, HIGH);
delayMicroseconds(long_high);
digitalWrite(Pin_regime, LOW);
delayMicroseconds(short_down);
digitalWrite(Pin_regime, HIGH);
delayMicroseconds(short_high);
digitalWrite(Pin_regime, LOW);
delayMicroseconds(long_down);
digitalWrite(Pin_regime, HIGH);
delayMicroseconds(short_high);
digitalWrite(Pin_regime, LOW);
delayMicroseconds(long_down);
digitalWrite(Pin_regime, HIGH);
delayMicroseconds(long_high);
```

```
digitalWrite(Pin_regime, LOW);
delayMicroseconds(short_down);
digitalWrite(Pin_regime, HIGH);
delayMicroseconds(short_high);
digitalWrite(Pin_regime, LOW);
delayMicroseconds(long_down);
digitalWrite(Pin_regime, HIGH);
delayMicroseconds(short_high);
digitalWrite(Pin_regime, LOW);
delayMicroseconds(long_down);
digitalWrite(Pin_regime, HIGH);
delayMicroseconds(short_high);
digitalWrite(Pin_regime, LOW);
delayMicroseconds(long_down);
digitalWrite(Pin_regime, HIGH);
delayMicroseconds(short_high);
digitalWrite(Pin_regime, LOW);
delayMicroseconds(long_down);
digitalWrite(Pin_regime, HIGH);
delay(6);
}
else if (current_regime == 30){
delay(6);
digitalWrite(Pin_regime, LOW);
delayMicroseconds(short_down);
digitalWrite(Pin_regime, HIGH);
delayMicroseconds(short_high);
digitalWrite(Pin_regime, LOW);
delayMicroseconds(long_down);
digitalWrite(Pin_regime, HIGH);
delayMicroseconds(long_high);
digitalWrite(Pin_regime, LOW);
delayMicroseconds(short_down);
digitalWrite(Pin_regime, HIGH);
delayMicroseconds(short_high);
digitalWrite(Pin_regime, LOW);
delayMicroseconds(long_down);
digitalWrite(Pin_regime, HIGH);
delayMicroseconds(long_high);
digitalWrite(Pin_regime, LOW);
delayMicroseconds(short_down);
digitalWrite(Pin_regime, HIGH);
delayMicroseconds(short_high);
digitalWrite(Pin_regime, LOW);
delayMicroseconds(long_down);
digitalWrite(Pin_regime, HIGH);
delayMicroseconds(short_high);
digitalWrite(Pin_regime, LOW);
delayMicroseconds(long_down);
digitalWrite(Pin_regime, HIGH);
delayMicroseconds(short_high);
digitalWrite(Pin_regime, LOW);
delayMicroseconds(long_down);
```

```
digitalWrite(Pin_regime, HIGH);
delayMicroseconds(short_high);
digitalWrite(Pin_regime, LOW);
delayMicroseconds(long_down);
digitalWrite(Pin_regime, HIGH);
delay(6);
}
else if (current_regime == 100){
delay(6);
digitalWrite(Pin_regime, LOW);
delayMicroseconds(short_down);
digitalWrite(Pin_regime, HIGH);
delayMicroseconds(long_high);
digitalWrite(Pin_regime, LOW);
delayMicroseconds(short_down);
digitalWrite(Pin_regime, HIGH);
delayMicroseconds(long_high);
digitalWrite(Pin_regime, LOW);
delayMicroseconds(short_down);
digitalWrite(Pin_regime, HIGH);
delayMicroseconds(short_high);
digitalWrite(Pin_regime, LOW);
delayMicroseconds(long_down);
digitalWrite(Pin_regime, HIGH);
delayMicroseconds(long_high);
digitalWrite(Pin_regime, LOW);
delayMicroseconds(short_down);
digitalWrite(Pin_regime, HIGH);
delayMicroseconds(short_high);
digitalWrite(Pin_regime, LOW);
delayMicroseconds(long_down);
digitalWrite(Pin_regime, HIGH);
delayMicroseconds(short_high);
digitalWrite(Pin_regime, LOW);
delayMicroseconds(long_down);
digitalWrite(Pin_regime, HIGH);
delayMicroseconds(short_high);
digitalWrite(Pin_regime, LOW);
delayMicroseconds(long_down);
digitalWrite(Pin_regime, HIGH);
delayMicroseconds(short_high);
digitalWrite(Pin_regime, LOW);
delayMicroseconds(long_down);
digitalWrite(Pin_regime, HIGH);
delay(6);
}
else if (current_regime == 300){
delay(6);
digitalWrite(Pin_regime, LOW);
delayMicroseconds(short_down);
digitalWrite(Pin_regime, HIGH);
delayMicroseconds(short_high);
digitalWrite(Pin_regime, LOW);
```

```
delayMicroseconds(long_down);
digitalWrite(Pin_regime, HIGH);
delayMicroseconds(short_high);
digitalWrite(Pin_regime, LOW);
delayMicroseconds(long_down);
digitalWrite(Pin_regime, HIGH);
delayMicroseconds(long_high);
digitalWrite(Pin_regime, LOW);
delayMicroseconds(short_down);
digitalWrite(Pin_regime, HIGH);
delayMicroseconds(long_high);
digitalWrite(Pin_regime, LOW);
delayMicroseconds(short_down);
digitalWrite(Pin_regime, HIGH);
delayMicroseconds(short_high);
digitalWrite(Pin_regime, LOW);
delayMicroseconds(long_down);
digitalWrite(Pin_regime, HIGH);
delayMicroseconds(short_high);
digitalWrite(Pin_regime, LOW);
delayMicroseconds(long_down);
digitalWrite(Pin_regime, HIGH);
delayMicroseconds(short_high);
digitalWrite(Pin_regime, LOW);
delayMicroseconds(long_down);
digitalWrite(Pin_regime, HIGH);
delayMicroseconds(short_high);
digitalWrite(Pin_regime, LOW);
delayMicroseconds(long_down);
digitalWrite(Pin_regime, HIGH);
delay(6);
}
else if (current_regime == 1000){
delay(6);
digitalWrite(Pin_regime, LOW);
delayMicroseconds(short_down);
digitalWrite(Pin_regime, HIGH);
delayMicroseconds(long_high);
digitalWrite(Pin_regime, LOW);
delayMicroseconds(short_down);
digitalWrite(Pin_regime, HIGH);
delayMicroseconds(short_high);
digitalWrite(Pin_regime, LOW);
delayMicroseconds(long_down);
digitalWrite(Pin_regime, HIGH);
delayMicroseconds(long_high);
digitalWrite(Pin_regime, LOW);
delayMicroseconds(short_down);
digitalWrite(Pin_regime, HIGH);
delayMicroseconds(long_high);
digitalWrite(Pin_regime, LOW);
delayMicroseconds(short_down);
digitalWrite(Pin_regime, HIGH);
```

```
delayMicroseconds(short_high);
digitalWrite(Pin_regime, LOW);
delayMicroseconds(long_down);
digitalWrite(Pin_regime, HIGH);
delayMicroseconds(short_high);
digitalWrite(Pin_regime, LOW);
delayMicroseconds(long_down);
digitalWrite(Pin_regime, HIGH);
delayMicroseconds(short_high);
digitalWrite(Pin_regime, LOW);
delayMicroseconds(long_down);
digitalWrite(Pin_regime, HIGH);
delayMicroseconds(short_high);
digitalWrite(Pin_regime, LOW);
delayMicroseconds(long_down);
digitalWrite(Pin_regime, HIGH);
delay(6);
}

//   else if (current_regime == 20){
//   digitalWrite(Pin_regime, HIGH);
// Serial.println("test");
//   delay(100);
//   digitalWrite(Pin_regime, LOW);
//   delay(100);
//   }
}


/////////////////////////////////////Select current regime ////////////////////////////////////
void select_regime(){
lcd.clear();
lcd.setCursor(0,0); // Text at top left corner
lcd.print("Regime[nA]:");

while (p!=1){

char key_regime = keypad.waitForKey();

if (key_regime) {  //Test Keypad input
//      Serial.println(key_regime);
lcd.setCursor(0,0); // Text at top left corner
lcd.print("Regime[nA]:");
lcd.setCursor(o,1); // second row
lcd.print(key_regime);
o++;    // Set Cursor one step further
}

if (key_regime >= ’0’ && key_regime <= ’9’){
InputRegime += key_regime;
}
else if (key_regime == ’#’){ // Press # for converting to number
```

```
if (InputRegime.length() > 0) {
regime = InputRegime.toInt(); // Conevrting String to Int to set Fluence
current_regime = regime/1000.0; // Converting nA in uC
InputRegime = ""; // Clear Input string
p = 1; // Condition to leave the loop
lcd.clear();
}
}
else if (key_regime == '*') {
InputRegime = ""; // Clear Input by pressing *
lcd.clear();
lcd.setCursor(0,0);
lcd.print("Regime [nA]:");
o=0;
}
}

currentint_regime(); // Send bitcode to currentintegrator to set regime
currentint_regime(); // Twice to be sure

lcd.clear();
lcd.setCursor(0,0);
lcd.print("Regime[uC]:");
lcd.setCursor(11,0);
if (current_regime < 0.01){
lcd.print(current_regime, 3);
}
else if (current_regime >= 0.01 && current_regime < 0.1){
lcd.print(current_regime, 2);
}
else if (current_regime >= 0.1 && current_regime < 1){
lcd.print(current_regime, 1);
}
else if (current_regime >= 1){
lcd.print(current_regime, 0);
}
lcd.setCursor(0,1);
lcd.print("Press any button");

}
```

Abbreviations

Abbreviation	Definition
2D	two dimensional
ADONIS	Anlage zur DepOsition Niederenergetischer Ionen auf Substrate
AES	Auger electron spectroscopy
AFM	atomic force microscopy
Al	aluminium
Ar	argon
ARPES	angle-resolved photoemission spectroscopy
B	boron
BCA	binary collision approximation
BN	boron nitride
BO	boron oxide
C	carbon
Ce	cerium
CH_4	methane
Cl	chlorine
CO	carbon monoxide
Cr	chromium
Cu	copper
CVD	chemical vapor deposition
DFT	density function theory
Fe	iron
Gd	gadolinium
H	hydrogen
He	helium
HOPG	highly oriented pyrolytic graphite
K	potassium

Abbreviation	Definition
Kr	krypton
LEED	low energy electron diffraction
Li	lithium
MD	molecular dynamic
Mo	molybdenum
MoS_2	molybdenum disulfide
$MoSe_2$	molybdenum diselenide
N	nitrogen
Nd	neodymium
Ne	neon
NRA	nuclear reaction analysis
O	oxygen
PIXE	particle induced X-ray emission
Pt	platinum
RBS	Rutherford backscattering spectroscopy
Si	silicon
Si_3N_4	silicon nitride
SiC	silicon carbide
SiO_2	silicon oxide
SKPM	Scanning kelvin probe microscopy
Sn	tin
STM	scanning tunneling microscopy
Ta	tantalum
TEM	transmission electron microscopy
TiN	titanium nitride
UHV	ultra high vacuum
ULE	Ultra-low Energy
V	vanadium
W	tungsten
XPS	X-ray photoelectron spectroscopy
ZBL	Ziegler-Biersack-Littmark
Zr	zirconium

Acknowledgements

At the end of this work, I would like to thank all the individuals who have supported me during my studies and my doctoral research.

First and foremost, I would like to express my gratitude to Prof. Dr. Hans Hofsäss, who made this work in his research group possible for me. I am immensely thankful for his trust in my independent work and the numerous assistance he provided, both in technical and theoretical matters.

I would like to express my gratitude to Prof. Dr. Martin Wenderoth and Prof. Dr. Michael Seibt for their participation in my advisory committee and for their helpful comments and suggestions during our joint meetings. I would also like to extend my thanks to Prof. Dr. Martin Wenderoth for providing the second evaluation. Additionally, I thank Prof. Cynthia A. Volkert, Prof. Dr. Thomas Weitz, and Prof. Dr. Lino da Costa Pereira for their participation in my examination committee.

I would like to express my gratitude to my partners from KU Leuven, Lino da Costa Pereira, Pin, and Zviadi, for our close collaboration. Due to the numerous visits by Pin and Zviadi to Göttingen and the countless hours we spent together in the laboratory during the implantations, I would consider both of you as honorary members of our research group.

While we're on the topic of members of the research group, I want to extend my gratitude to all current and former colleagues who made my time during my doctoral studies more enjoyable. In particular, I'd like to mention Manuel, Patrick, Koen, Leonard, Dimitar, Helene, Stefan and Nikolai. Whether it was the over 200 chess games with Patrick, the countless hours in the lab with Manuel, or the regular cake sessions in the Caphy, your presence made a significant difference. I'm also thankful for your support at physics-related questions or during our joint accelerator repairs. Furthermore, I'd like to thank Patrick, Manuel, and Koen for proofreading this work and providing me with valuable suggestions.

I also thank the other doctoral students at the institute, including Marike Schwickardi, Julian Uthes, André Wilhahn, and Yannik Buch, for a pleasant shared time.
I thank Marius Herold for the training on the AFM and the support during the measurements

Unserem Team von technischen Mitarbeitern des Instituts und der Feinmechanik, bestehend aus Rüdiger Widera, Peter Arnsberger, Tim Kannengießer, Sascha Böhlken und Uwe Ronsöhr, sowie der Zentralwerkstatt unter der Leitung von Christof Schmidt und den Mitarbeitern der E-Werkstatt Marco Peltzer, Andrey Eger, Michael Hillmann und Reinhard Mielke, möchte ich meinen herzlichen Dank für eure fachkundigen Beratungen und technische Unterstützung aussprechen. Besonders hervorzuheben ist hierbei Peter, der oft als Retter in der Not fungierte und Teile in kürzester Zeit reparierte oder neu baute.

Ebenso danke ich dem Sekretariat mit Bernadette, Janika und Vicky für die Unterstützung und die Korrektur von fehlerhaften Anträgen.

Abschließend möchte ich meinen Freunden und meiner Familie danken, die mich während meines gesamten Studiums unterstützt haben. Besonders meine Mutter, Susanne Lange-Junge, hat mich in jedem Motivationstief aufgemuntert und mich stets unterstützt.

The funding of this work in the project "Perspektiven der Dotierung von Graphen mittels Ionenstrahlimplantation mit Ionen niedriger Energie" (project number 421708041) by the DFG is highly acknowledged.

Thank you all!